



HAL
open science

Hydrate crystallization from cyclopentane loaded on porous activated carbon particles for produced waters desalination

Rafik Mallek

► **To cite this version:**

Rafik Mallek. Hydrate crystallization from cyclopentane loaded on porous activated carbon particles for produced waters desalination. Physics [physics]. Université de Pau et des Pays de l'Adour, 2021. English. NNT : 2021PAUU3047 . tel-03793816

HAL Id: tel-03793816

<https://theses.hal.science/tel-03793816v1>

Submitted on 2 Oct 2022

HAL is a multi-disciplinary open access archive for the deposit and dissemination of scientific research documents, whether they are published or not. The documents may come from teaching and research institutions in France or abroad, or from public or private research centers.

L'archive ouverte pluridisciplinaire **HAL**, est destinée au dépôt et à la diffusion de documents scientifiques de niveau recherche, publiés ou non, émanant des établissements d'enseignement et de recherche français ou étrangers, des laboratoires publics ou privés.

THESE

UNIVERSITE DE PAU ET DES PAYS DE L'ADOUR

Ecole Doctorale des Sciences et leurs Applications

Par

Rafik MALLEK

Pour l'obtention du grade de

DOCTEUR

Spécialité : Physique

**Cristallisation de l'hydrate de cyclopentane à partir
de particules poreuses de charbon actif chargées en
cyclopentane pour le dessalement des eaux de
production**

16 Décembre 2021

Jury

Mme V. FIERRO	DR CNRS	Université de Lorraine	Rapporteur
M. B. BOUILLOT	MC-HDR	Ecole des mines Saint-Etienne	Rapporteur
M. J.P. CROUE	Professeur	Université de Poitiers	Examineur
M. P. BALDONI-ANDREY	Ingénieur, Dr.	TotalEnergies	Examineur
M. C. DICHARRY	Professeur	Université de Pau	Directeur
Mme. C. MIQUEU	MC-HDR	Université de Pau	Co-directeur

THESIS

UNIVERSITY OF PAU ET PAYS DE L'ADOUR

Doctoral School of Exact Science and their Applications

Presented by

Rafik MALLEK

For obtaining the grade of

DOCTOR OF PHYLOSOPHY

Speciality: Physics

**Hydrate crystallization from cyclopentane loaded on
porous activated carbon particles for produced
waters desalination**

December 16th, 2021

Jury

Ms. V. FIERRO	DR CNRS	University of Lorraine	Reviewer
Mr. B. BOUILLOT	MC-HDR	Mines Saint-Etienne	Reviewer
Mr. J.P. CROUE	Professor	University of Poitiers	Examiner
Mr. P. BALDONI-ANDREY	Engineer, PhD	TotalEnergies	Examiner
Mr. C. DICHARRY	Professor	University of Pau	Supervisor
Ms. C. MIQUEU	MC HDR	University of Pau	Co-supervisor

My PhD work is dedicated to the memory of my grand-father

Dr. Elhadj Mohammed MALLEK

1934-2017

“Rabbi-Yarhmou”

Acknowledgments

The work presented in this thesis was carried out at the Complex Fluids and Reservoirs Laboratory (LFCR – Pau and Anglet campus) and the Thermal, Energetic and Process Laboratory (LaTEP at Pau). It was achieved via the collaboration of the industrial partners TotalEnergies company and BGH start-up. Firstly, I would like to thank these institutions for having me as a member of their team. In particular, I extend my acknowledgment to TotalEnergies company for funding my PhD project.

I would like to express very special thanks to my supervisors Mr. Christophe Dicharry and Ms. Christelle Miqueu for their help, availability and kindness. I learned a lot from you!

I show a substantial gratitude to Mr. Frederic Plantier and Mr. Manuel Ildefonso for their help and discussions.

I gratefully acknowledge TotalEnergies and BGH members, Mr. Patrick Baldoni-Andrey, Mr. Matthieu Jacob, Mr. Pascal Le Mélinaire, Mr. Stephane Nowe and Mr. Hervé Nabet for their remarks and discussions.

I would like to thank Ms. Vanessa Fierro and Mr. Baptiste Bouillot for accepting to read and evaluate my thesis, and also Mr. Jean-Philippe Croué and Mr. Patrick Baldoni-Andrey for agreeing to participate as guest members of the jury.

I wish to address a big fat acknowledgment to Joseph Diaz for his help and the amazing football discussions.

I am really grateful to Mr. Jean-Pierre Bedecarats for having warmly received me in the LaTEP laboratory. I am also grateful to Mr. Philippe Thomas for providing me with some of the activated carbon samples used in my thesis.

I would like to thank my colleagues Hafid, Dyhia, Ababakari, Soufiane, Saphir, Mohammed, Kedi, Bich, Daoud, Shweta, Khaled, Youcef and Lionel. Thank you for the great time we spent together.

My thanks to my friends Takwa, Akli, Nabil, Hamza, Walid, Ilyes, Nouredine, Sifou and Youcef.

As it is said, the best for the last, I would like to thank my parents (Chikh and Oumi), my brother Amir and my sisters Meriem and Nova. Literally, thank you for everything!

List of publications and communications

Rafik Mallek, Christelle Miqueu, Matthieu Jacob, Pascal Le Mélinaire, Christophe Dicharry, Effect of porous activated carbon particles soaked in cyclopentane on CP-hydrate formation in synthetic produced water, Journal of Water Process Engineering, Volume 38, 2020, 101660, ISSN 2214-7144, <https://doi.org/10.1016/j.jwpe.2020.101660>.

Rafik Mallek, Frédéric Plantier, Christophe Dicharry, Matthieu Jacob, Christelle Miqueu, Experimental characterization of cyclopentane adsorption/desorption in microporous activated carbons, Carbon Trends, Volume 2, 2021, 100021, ISSN 2667-0569, <https://doi.org/10.1016/j.cartre.2020.100021>.

Rafik Mallek, Christelle Miqueu, Matthieu Jacob, Christophe Dicharry, Investigation on hydrate formation from cyclopentane-loaded porous activated carbon particles, submitted to Chemical Engineering Sciences in October 2021.

Rafik Mallek, Christelle Miqueu, Matthieu Jacob, Christophe Dicharry, Experimental evaluation of the partial thermal energy compensation of hydrate crystallization from cyclopentane-loaded porous activated carbon particles immersed in brine, Desalination, Volume 530, 2022, 115662, <https://doi.org/10.1016/j.desal.2022.115662>.

Rafik Mallek, Frédéric Plantier, Manuel Ildefonso, Pascal Le Mélinaire, Matthieu Jacob, Christelle Miqueu, Christophe Dicharry, Desalination of produced water: evaluation of a new process based on hydrate formation with cyclopentane confined in porous activated carbon particles, the 10th International Conference on Gas Hydrates (ICGH10), accepted for oral presentation.

Table of contents

List of Figures	viii
List of Tables	xi
Abstract	xii
Résumé	xiii
Main notation	xiv
General introduction	1
References	5
Chapter 1. Generalities and state-of-the-art	6
1.1. Introduction	6
1.2. Clathrate hydrates	6
1.2.1. Definition	6
1.2.2. Main structures	7
1.2.3. Hydration number	8
1.2.4. Phase diagram	9
1.2.5. Hydrate formation	10
1.2.5.1. Driving force	10
1.2.5.2. Nucleation	11
1.2.5.2.1. Primary nucleation	12
1.2.5.2.2. Secondary nucleation	13
1.2.5.3. Growth	14
1.2.5.4. Metastability and memory effect	14
1.2.6. Enthalpy of dissociation	15
1.2.7. Effect of inorganic salts	15
1.2.8. Morphology	16
1.2.9. Main areas of study	16
1.2.9.1. Enhancement of hydrate formation kinetics	17
1.2.9.2. Hydrate-based applications	17
1.2.10. Cyclopentane hydrates	18
1.3. Produced water	19
1.3.1. Definition	19
1.3.2. Composition	20
1.3.3. Management	20
1.4. Water desalination processes	21

1.4.1. Major desalination processes -----	22
1.4.1.1. Thermal technologies -----	22
1.4.1.1.1. Multi-Stage Flash (MSF)-----	23
1.4.1.1.2. Multi-Effect Distillation (MED)-----	23
1.4.1.2. Membrane technologies -----	24
1.4.2. Hydrate-Based technologies -----	25
1.4.2.1. Description-----	25
1.4.2.2. Comparison of HBD with the major desalination processes-----	26
1.4.2.3. Development and challenges of HBD technology -----	27
1.4.2.4. BGH process -----	29
1.5. Porous media -----	30
1.5.1. Definition-----	30
1.5.2. Main Characteristics-----	30
1.5.2.1. Porosity-----	30
1.5.2.2. Pore size distribution-----	31
1.5.2.3. Specific surface -----	31
1.5.3. Example of porous media -----	32
1.5.4. Adsorption phenomena -----	32
1.5.4.1. Definitions -----	32
1.5.4.2. Adsorption/Desorption mechanisms-----	33
1.5.4.2.1. Adsorption mechanisms -----	33
1.5.4.2.2. Desorption mechanisms -----	35
1.5.4.3. Surface-excess adsorbed amount -----	36
1.5.4.4. Adsorption isotherms -----	37
1.5.4.5. Adsorption enthalpy-----	38
1.5.4.5.1. Differential enthalpy of adsorption-----	38
1.5.4.5.2. Isosteric enthalpy of adsorption-----	39
1.6. Hydrate formation in presence of solid materials/porous media -----	39
1.6.1. Open-solid surfaces-----	40
1.6.2. Confining solids -----	40
1.6.3. Packed-beds -----	41
1.7. Conclusion -----	42
1.8. References -----	43
Chapter 2. Experimental techniques and setups -----	50
2.1. Introduction-----	50
2.2. Materials-----	50

2.3. Description of experimental techniques and setups-----	51
2.3.1. Characterization of virgin PACP-----	51
2.3.1.1. Laser diffraction -----	52
2.3.1.2. Gas porosimetry -----	52
2.3.1.3. Mercury intrusion porosimetry -----	55
2.3.2. Analysis of CP adsorption-desorption on/from the PACP-----	57
2.3.2.1. Gravimetric technique -----	57
2.3.2.2. Calorimetric-manometric technique -----	61
2.3.2.3. Gas Porosimetry -----	64
2.3.2.4. Themogravimetric analysis -----	64
2.3.3. Analysis of hydrate formation from CP-loaded PACP -----	64
2.3.3.1. Batch-chemical reactors-----	65
2.3.3.2. Calorimetric measurements-----	66
2.3.3.2.1. Differential scanning calorimeter micro-DSC7 evo-----	66
2.3.3.2.2. Tian-Calvet BT2.15 calorimeter -----	67
2.3.3.3. Optical microscopy-----	68
2.4. Conclusion -----	69
2.5. References -----	70

Chapter 3. Effect of porous activated carbon particles soaked in cyclopentane on CP-hydrate formation in synthetic produced water ----- 72

3.1. Introduction-----	72
3.2. Experimental methods -----	73
3.2.1. Preliminary investigation -----	73
3.2.1.1. Effect of NaCl concentration on CP-hydrate equilibrium temperature -----	73
3.2.1.2. Effect of NaCl concentration on CP-hydrate growth rate -----	74
3.2.2. Hydrate formation experiments in BGH process -----	75
3.2.2.1. Effect of PACP and stirring rate on CP-hydrate formation -----	77
3.2.2.2. Effect of the CP-loading rate of PACP on CP-hydrate formation -----	78
3.2.2.3. Effect of the size of PACP on CP-hydrate formation -----	78
3.2.2.4. Effect of water salinity on CP-hydrate formation -----	78
3.3. Results and discussion-----	79
3.3.1. Effect of NaCl on CP-hydrate formation -----	79
3.3.1.1. Effect of NaCl concentration on CP-hydrate equilibrium temperature -----	79
3.3.1.2. Effect of NaCl concentration on CP-hydrate growth rate -----	80
3.3.2. Hydrate formation experiments in BGH process -----	82
3.3.2.1. Effect of PACP and stirring rate on CP-hydrate formation -----	82

3.3.2.2. Effect of CP-loading rate of PACP on CP-hydrate formation -----	84
3.3.2.3. Effect of the size of PACP on CP-hydrate formation -----	86
3.3.2.4. Effect of water salinity on CP-hydrate formation -----	87
3.4. Conclusion -----	89
3.5. References -----	90

Chapter 4. Experimental characterization of cyclopentane adsorption/desorption in porous activated carbon particles ----- 92

4.1. Introduction-----	92
4.2. Experimental Methods-----	93
4.2.1. PACP characterization -----	93
4.2.2. Adsorption/desorption of CP -----	94
4.3. Results and discussion-----	95
4.3.1. Characterization of the virgin PACP -----	95
4.3.2. Adsorption/desorption of CP in the PACP -----	97
4.3.2.1. Adsorption capacity and enthalpy -----	97
4.3.2.2. Trapping capacity-----	99
4.3.3. Characterization of the PACP after CP adsorption/desorption-----	100
4.3.3.1. Identification of the pore sizes responsible of CP trapping -----	100
4.3.3.2. Influence of the CP loading process on CP trapping -----	101
4.3.3.3. Influence of purification temperature on CP trapping-----	103
4.4. Conclusion -----	104
4.5. References -----	105

Chapter 5. Investigation on hydrate formation from cyclopentane-loaded porous activated carbon particles ----- 107

5.1. Introduction-----	107
5.2. Experimental methods -----	108
5.2.1. Characterization of PACP and determination of adsorption capacities -----	108
5.2.2. CP-Hydrate formation from CP-saturated PACP -----	109
5.2.3. CP-Hydrate formation from CP-oversaturated PACP -----	110
5.2.4. Visualization of CP-hydrate crystallization from CP-loaded PACP -----	112
5.3. Results and Discussion -----	112
5.3.1. Characterization of PACP and determination of adsorption capacities -----	112
5.3.2. CP-Hydrate formation from of CP-saturated PACP -----	115
5.3.3. CP-Hydrate formation from CP-oversaturated PACP -----	119
5.3.4. Visualizing of CP-hydrate crystallization from CP-loaded PACP -----	120

5.4. Conclusion -----	122
5.5. References -----	123
Chapter 6. Experimental evaluation of the partial thermal energy compensation of hydrate crystallization from cyclopentane-loaded porous activated carbon particles immersed in brine -----	124
6.1. Introduction -----	124
6.2. Experimental methods -----	125
6.2.1. Preparation of the CP-saturated PACP -----	125
6.2.2. Investigation into the CP desorption-CP hydrate crystallization thermal energy compensation -----	126
6.3. Results and discussion -----	128
6.4. Conclusion -----	132
6.5. References -----	133
General conclusion -----	134
Perspectives -----	137
General overview of the thesis (In French) -----	138
Introduction générale -----	138
Principaux résultats et conclusions -----	141
Perspectives -----	144
References -----	145
Appendix -----	146
Appendix A -----	146
Appendix B -----	147
Appendix C -----	152
Appendix D -----	155
Graphical abstract -----	157

List of Figures

Figure 1. 1. General schematic representation of a clathrate hydrate. Taken from [5].	7
Figure 1. 2. Clathrate hydrate common structures. Taken from [1].	8
Figure 1. 3. Pressure – temperature phase diagram of pure water-light alkane system. Adapted from [2].	10
Figure 1. 4. Types of hydrate nucleation.	12
Figure 1. 5. Gibbs free energy evolution for primary nucleation process as dictated by the classical nucleation theory. Taken from [13].	13
Figure 1. 6. CP-hydrate structure. Taken from [45].	18
Figure 1. 7. Equilibrium temperatures of CP-hydrates vs. salt concentration. Taken from [8].	19
Figure 1. 8. History and forecast annual growth of desalination market. Taken from [55].	22
Figure 1. 9. Global contracted capacity by technology in 2013.	22
Figure 1. 10. Multi-stage flash principle. Adapted from [54].	23
Figure 1. 11. Multi-effect-distillation principle. Adapted from [54].	24
Figure 1. 12. RO principle. Taken from [57].	25
Figure 1. 13. HBD concept. Adapted from [3].	26
Figure 1. 14. HBD research progress over time. Taken from [3].	28
Figure 1. 15. BGH process concept. Taken from BGH startup.	29
Figure 1. 16. Pore features in coal. Taken from [65].	30
Figure 1. 17. Schematic representation of a solid surface. Taken from [64].	31
Figure 1. 18. Mechanisms of adsorption. Taken from [66].	34
Figure 1. 19. Schematic representation of as cavitation and pore blocking mechanisms. Adapted from [69].	35
Figure 1. 20. Schematic description of surface-excess adsorbed amount. Adapted from [66].	36
Figure 2. 1. Mastersizer 2000 apparatus. (1) Hydro 2000; (2) Optical bench	52
Figure 2. 2. Principle of laser diffraction technique. Taken from [4].	52
Figure 2. 3. Autosorb Quantachrome IQ instrument.	54
Figure 2. 4. Basic schematic of manometric technique. Adapted from [9].	54
Figure 2. 5. Schematic representation of the procedure used in calculating a DFT pore-size distribution from experimental adsorption/desorption isotherms. Taken from [7].	55
Figure 2. 6. Autopore IV 9500 instrument. a) low pressure port; b) high pressure port.	56
Figure 2. 7. Magnetic suspension balance (MSB). Adapted from [9].	60
Figure 2. 8. Measurement positions of the MSB. Taken from [9].	60
Figure 2. 9. Experimental setup used for determination of adsorption/desorption isotherms.	60
Figure 2. 10. Calometric-manometric apparatus developed by Mouahid et al. (2010) [9].	63
Figure 2. 11. Experimental setup for CP-hydrate formation: a) 1-L reactor, b) mechanical stirrer, c) stirring shaft, d) temperature sensor (PT100), e) funnel, f) syringe, g) syringe filter (0.8 μm), h) refractometer, i) cryostat, j) refrigerant fluid.	65
Figure 2. 12. Principle of DSC measurements. Taken from [18].	67
Figure 2. 13. 3D-Calvet sensor. Taken from [19].	68
Figure 2. 14. Experimental setup used in observing hydrate formation. Adapted from [20]	68

Figure 3. 1. Experimental procedure to determine the relative water-to-hydrate conversion rate (<i>RWHC</i>) and the final relative water-to-hydrate conversion rate (<i>RWHC_f</i>). a) Measured refractive index of the synthetic PW and deduced NaCl concentration vs. time (insert), b) calculated water-to-hydrate conversion (<i>WHC</i>) vs. time, c) determination of <i>RWHC</i> and <i>RWHC_f</i>	77
Figure 3. 2. CP-hydrate and ice equilibrium temperatures as a function of NaCl concentration. This graph also shows the three initial experimental conditions (starting points 1, 2 and 3) used for the CP-hydrate formation experiments.	79
Figure 3. 3. Measured lateral growth rate of CP-hydrates formed at the water/CP interface, at different NaCl concentrations and subcoolings of 2 and 6°C.	81
Figure 3. 4. Effect of PACP (Gbac loaded with 0.8 g of CP per gram of PACP) and stirring rate on the relative water-to-hydrate conversion. The NaCl concentration is 3.5 wt%.	82
Figure 3. 5. Effect of the CP-loading rate of PACP (Gbac) on the relative water-to-hydrate conversion rate with 3.5 wt% NaCl. The stirring rate is 180 rpm.	85
Figure 3. 6. Effect of PACP size (400 and 700 μm) on the relative water-to-hydrate conversion with 3.5 wt% NaCl. The PACP are loaded with 0.8 g of CP per gram of PACP. The stirring rate is 180 rpm.	87
Figure 3. 7. Effect of water salinity on the relative water-to-hydrate conversion. The PACP (Gbac) are loaded with 0.8 g of CP per gram of PACP. The stirring rate is 180 rpm.	88
Figure 4. 1. Particle size distribution of Gbac and Abac.	95
Figure 4. 2. (Top) pore volumes of the PACP measured by Ar adsorption at 87 K and obtained with a QSDFT model. (bottom) corresponding PSD.	96
Figure 4. 3. Adsorption/desorption isotherms of CP at 30°C on the different AC measured by gravimetry. Filled marks: adsorption; empty marks: desorption. Squares: Gbac, circles: Abac, diamonds: ChemA, stars: Cycarb. Black triangles: Adsorption of CP on Gbac measured with manometric/calorimetric device. The inset is a zoom of the low-pressure measurements. Dotted lines are guide-for-the-eyes.	97
Figure 4. 4. Differential heat of adsorption of CP at 30°C on Gbac and ChemA measured with a manometric-calorimetric device.	99
Figure 4. 5. Weight of the sample as a function of time during desorption measured with the MSB. (left): typical of $P > 1$ kPa. (right): typical of $P < 1$ kPa with prolonged evacuation.	100
Figure 4. 6. (top) pore volumes of the PACP measured by Ar adsorption at 87 K and obtained with a QSDFT model. (bottom) corresponding pore size distributions. (left): Gbac and Abac. (right): ChemA and Cycarb. Solid lines: virgin PACP. Dashed lines: same PACP samples after CP adsorption/desorption. All the results are given per gram of PACP.	101
Figure 4. 7. Comparison of CP-loading method (vapor-CP adsorption vs. liquid-CP imbibition) in Gbac and ChemA. (top) Pore volumes of the PACP measured by Ar adsorption at 87 K and obtained with a QSDFT model. (bottom) corresponding pore size distributions. (left): Gbac. (right): ChemA. Solid lines: virgin PACP. Dashed lines: same samples after CP loading/evacuation.	102
Figure 4. 8. Effect of purification temperature upon release of CP from microporosity of Gbac. (top) Pore volumes of the PACP measured by Ar adsorption at 87 K and obtained with a QSDFT model. (bottom) corresponding pore size distributions. Solid lines: virgin PACP. Dashed lines: same sample after CP adsorption/desorption with different purification temperatures.	103
Figure 4. 9. Mass loss (measured by TGA) and proportion of pore volume recovered by secondary vacuum (measured by Ar porosimetry at 87 K) as a function of purification temperature.	104

Figure 5. 1. CP-saturated PACP immersed in water.	110
Figure 5. 2. Temperature profile imposed for hydrate formation and dissociation from CP-saturated PACP.	110
Figure 5. 3. CP-oversaturated PACP immersed in water.	111
Figure 5. 4. PSD and cumulative pore volumes of PACP obtained with QSDFT Ar at 87 K.	113
Figure 5. 5. Mercury intrusion curve (cumulative intrusion volume as a function of intrusion pressure) for Gbac.	113
Figure 5. 6. Mercury intruded volume as a function of pore size for the three PACP.	114
Figure 5. 7. Hydrate dissociation peaks of CP hydrates formed from CP-saturated PACP.	116
Figure 5. 8. CP-to-hydrate masses throughout the cycles.	116
Figure 5. 9. Determination of the threshold pore size of pores releasing CP.	118
Figure 5. 10. Proposed mechanism governing hydrate formation from CP-saturated PACP.	118
Figure 5. 11. Hydrate dissociation peaks of CP hydrates formed from CP-oversaturated PACP.	120
Figure 5. 12. Microscopic observation of hydrate formation from CP-saturated or oversaturated Gbac.	121
Figure 5. 13. A proposal of the mechanism governing the conversion of surface CP into hydrate. ..	122
Figure 6. 1. Preparation of CP-saturated PACP.	125
Figure 6. 2. Preparing the system for the hydrate formation experiment in the calorimetric cell of the BT2.15 apparatus. 1) measurement cell, 2) hydrate seed, 3) CP-saturated PACP, and 4) brine.	128
Figure 6. 3. Experimental procedure to determine thermal energy compensation.	128
Figure 6. 4. Thermal energy peak (green curve) generated by subtracting the “blank” thermogram (brown curve) from the “experiment” thermogram (blue curve) for the 3.5 wt% NaCl solution (left) and 8 wt% NaCl solution (right).	129
Figure 6. 5. Comparison of the thermal energy peak obtained in two repeated experiments with the 3.5 wt% NaCl solution (left) and the 8 wt% NaCl solution (right).	129
Figure 6. 6. Comparison of the balanced energy obtained in the case of hydrate formation from CP-saturated PACP (green area), and differential enthalpy of CP adsorption from PACP (blue and black dots).	131

List of Tables

Table 1. 1. Some methods/techniques used in the determination of gas hydrate equilibrium conditions.	9
Table 1. 2. Dissociation enthalpies of some gas hydrates.	15
Table 1. 3. Hydrate crystal morphology as a function of subcooling.	16
Table 1. 4. Morphology of CP-hydrate crystals as function of subcooling.	18
Table 1. 5. Main components of PW. Adapted from [49].	20
Table 1. 6. Standards for PW reuse in gas industry. Adapted from [49].	21
Table 1. 7. Comparison of HBD, MSF and RO processes.	27
Table 1. 8. Adsorption isotherms and their corresponding adsorbent.	38
Table 2. 1. The different PACP used in this work.	50
Table 3. 1. CP-hydrate equilibrium temperatures (T_{eq}) measured at different NaCl concentrations ([NaCl]).	80
Table 3. 2. Values of the induction time, the relative water-to-hydrate conversion rate and the final relative water-to-hydrate conversion (at $t = 78$ hrs) for the systems with and without PACP (Gbac loaded with 0.8 g of CP per gram of PACP) and different stirring rates. The initial conditions for these experiments correspond to starting point 1 (Figure 3.2).	82
Table 3. 3. Values of the relative water-to-hydrate conversion rate and the final relative water-to-hydrate conversion (at $t = 24$ hrs) for the systems with PACP (Gbac) at different CP-loading rates. The initial conditions for these experiments correspond to starting point 1 (Figure 3.2). The stirring rate is 180 rpm.	85
Table 3. 4. Values of the relative water-to-hydrate conversion rate and the final relative water-to-hydrate conversion (at $t = 24$ hrs) for the different sizes of PACP (Gbac (700 μm) and Abac (400 μm)) loaded with 0.8 g of CP per gram of PACP. The initial conditions for these experiments correspond to starting point 1 (Figure 3.2). The stirring rate is 180 rpm.	87
Table 3. 5. Values of the relative water-to-hydrate conversion rate and the final relative water-to-hydrate conversion (at $t = 24$ hrs) for the system with PACP (Gbac loaded with 0.8 g of CP per gram of PACP). The initial conditions for these experiments correspond to starting points 1, 2 and 3 (Figure 3.2). The stirring rate is 180 rpm.	88
Table 4. 1. Main characteristics of the four PACP used in this work.	96
Table 5. 1. Characteristics of the PACP used.	115
Table 5. 2. Maximum CP-conversion rates.	118
Table 5. 3. CP-conversion rates in the presence of PACP (Gbac or BGX).	120
Table 6. 1. Indirect measurement of hydrate formation energy.	130
Table 6. 2. Determination of the balanced energy per mole of CP.	130

Abstract

This thesis falls within the context of water desalination in oil and gas industry. Indeed, oil production is accompanied with large amounts (3 barrels of water for 1 barrel of oil) of high salinity water (around 8 wt% TDS), known as produced water. This latter should be desalinated so that to be discharged or reused. Recently, a French start-up, called BGH, patented a hydrate-based desalination (HBD) process but with the innovation of using porous activated carbon particles (PACP) loaded with cyclopentane (CP). The aim of this thesis is to gain deeper insight into the mechanisms governing the hydrate formation stage of this process. For that purpose, fine characterizations of the PACP and their CP-adsorption capacities (determined using gas and mercury intrusion porosimetry and gravimetric technique, respectively), hydrate formation experiments at different scales (from microliters (in a micro-DSC) to liters (in a stirred batch reactor)) and microscopic observations are performed.

The obtained results show that CP-loaded PACP enhance the hydrate formation kinetics and feed hydrate crystallization with CP, thus acting as both kinetic promoter and CP-source. It is found that the CP available for hydrate formation is predominantly contained in large pores and on the external surface of the PACP. Indeed, CP contained in the pores larger than a threshold pore size can desorb to form hydrate inside and/or outside the pores, while the CP held by the external surface of the PACP is released as droplets before being converted to hydrate. Accordingly, it is shown that the use of CP-oversaturated PACP with a pore size distribution developed towards meso- and macroporous regions, in combination with a high meso- to macropore volume, significantly increase hydrate conversion rate (from 1% to 45%). Finally, it is shown that CP-desorption from the PACP (endothermic reaction) compensates up to 40% of the hydrate crystallization (exothermic) energy.

Keywords: *Cyclopentane hydrates, Hydrate crystallization, Adsorption, Activated carbons, Brine desalination, Hydrate-based desalination, Energy compensation.*

Résumé

Cette thèse s'inscrit dans le contexte du dessalement des eaux de production de l'industrie pétro-gazière. En effet, la production d'hydrocarbures s'accompagne de grandes quantités d'eau (3 barils d'eau pour 1 baril de pétrole) de salinité élevée (environ 8% en masse de TDS). Ces eaux de production doivent être dessalées avant d'être rejetées ou réutilisées. Récemment, une start-up française, appelée BGH, a breveté un procédé de dessalement à base d'hydrates mais avec l'innovation d'utiliser des particules poreuses de charbon actif (PPCA) chargées en cyclopentane (CP). L'objectif de cette thèse est de mieux comprendre les mécanismes qui régissent l'étape de formation des hydrates dans ce procédé. Dans ce but, des caractérisations fines des PPCA et de leurs capacités d'adsorption du CP (déterminées respectivement par des mesures de porosimétrie gaz et d'intrusion mercure, et par gravimétrie d'adsorption), des expériences de formation d'hydrates à différentes échelles (du microlitre (dans la cellule d'un microcalorimètre DSC) au litre (dans un réacteur batch agité)) et des observations microscopiques ont été réalisées.

Les résultats obtenus montrent que les PPCA chargées en CP améliorent la cinétique de formation et la croissance des hydrates, agissant ainsi à la fois de promoteur cinétique et de source de CP. Le CP disponible pour la formation d'hydrates est principalement contenu par les pores supérieurs à une taille seuil et sur la surface externe des PPCA. Le CP qui se désorbe des grands pores forme des hydrates à l'intérieur et/ou à l'extérieur des pores, tandis que le CP de la surface externe est libéré sous forme de gouttelettes avant d'être converti en hydrates. L'utilisation de PPCA sursaturées en CP avec une distribution de taille de pores développée vers des régions méso et macroporeuses, en combinaison avec un volume élevé de méso-macropores, améliore significativement le taux de conversion du CP en hydrates (de 1% à 45%). Enfin, il est démontré que la désorption du CP des PPCA (réaction endothermique) compense jusqu'à 40% de l'énergie de cristallisation des hydrates (réaction exothermique).

Mots clés : *Hydrates de cyclopentane, Cristallisation d'hydrates, Adsorption, Charbons actifs, Dessalement de saumures, Dessalement à base d'hydrates, Compensation d'énergie.*

Main notation

Notation Category	Designation
<i>Subscript</i>	
i	initial
f	final
eq	equilibrium
hr	hour
hrs	hours
des	desorption
crys	crystallization
<i>Chemical formula</i>	
C ₅ H ₁₀	Cyclopentane
NaCl	Sodium chloride
Ar	Argon
He	Helium
N ₂	Nitrogen
Water desalination	
PW	Produced water
TDS	Total dissolved solids
[NaCl]	Sodium chloride concentration
MSF	Multi-stage flash
MED	Multi-effect distillation
RO	Reverse osmosis
HBD	Hydrate-based desalination
<i>Techniques/setup</i>	
DSC	Differential scanning calorimetry
MIP	Mercury intrusion porosimetry
MSB	Magnetic suspension balance
TGA	Thermogravimetric analysis
<i>Characteristics of Porous media</i>	
PSD	Pore size distribution
PV	Pore volume
SSA	Specific surface area
SD	Particle size distribution
<i>Adsorption/desorption experiments</i>	
n_{ads}^{excess}	Surface-excess adsorbed amount
P/P ₀	Equilibrium pressure/Saturation pressure
ΔH_{diff}	Differential enthalpy of adsorption

Hydrate formation experiments

CP	Cyclopentane
PACP	Porous activated carbon particles
ΔT	Subcooling
nD	Refractive index measured at a wavelength of 589.3 nm
T _{ind}	Induction time
WHC	Water-to-hydrate conversion
WHC _{th,max}	Maximal theoretical water-to-hydrate conversion
RWHC	Relative water-to-hydrate conversion
$R\dot{W}HC$	Relative water-to-hydrate conversion rate
E	Energy

General introduction

In the last decades, the world has witnessed a noticeable population growth (1-2% [1]) and fast technology development which has induced both a growth in energy consumption and environmental degradation. Therefore, energy supply and environment protection have become a world priority. This is reflected by both the growth in energy demand (+27% expected from 2017 to 2040 [2]) and the various environmental conventions and regulations (Kyoto protocol, COPs, etc.).

One of the major energy supplier is oil and gas industry, presenting 54.4% of the world energy supply [3]. During hydrocarbon production, large amounts (about 75% of the effluents [4]) of high salinity water (around 8 wt% TDS¹ [5]), called produced water, is coproduced. A good management of this by-product is one of the challenging activities of oil and gas industry. Produced water could be either stored, discharged or reused. Storing is not an option due to the huge amounts of produced water, whereas discharge (very often in seawater) and/or reuse (mainly reinjection into the producing reservoir to sustain reservoir pressure) are the commonly used options. Due to the high salinity of produced water, environmental restrictions (laws and regulations) and technical limitations (possible compatibility issues with formation water, tubing corrosion, etc.) make water desalination a recommended process before any discharge or reinjection operation.

Nowadays, several water desalination processes are used including distillation-based processes (multi-stage flash (MSF), multi effect distillation (MED)), reverse osmosis (RO), nanofiltration (NF), electro dialysis (ED), etc. RO and water distillation are the most commonly used processes (65 and 30%, respectively) of the world's global desalination capacity [6]. However, these conventional processes present either technical limitations (low feed-water salinity is required in case of RO (< 4.3 wt% TDS [7])) or high economic impact (high-energy consumption for distillation inducing high costs (1.1-1.5 USD/m³ [8])). With the aim to efficiently desalinate water, that is with a low economic impact and less

¹ Total dissolved Solids: the total concentration of dissolved organic and inorganic matter in water.

technical limitations, an unconventional desalination process called hydrate-based desalination (HBD) process has been proposed as a potential alternative [9]. This latter exploits clathrate hydrate (ice-like solids) formation and dissociation to produce a less salty water. Indeed, water molecules form cages around guest compounds (added to water), thereby separating themselves from salt molecules which do not participate to the hydrate structure. The choice of the guest can allow to proceed even at temperatures higher than the normal freezing temperature of water [8]. Once the hydrates have formed, the hydrate crystals are separated from the remaining brine, in which salts are concentrated. The separated crystals are then dissociated and desalinated water (in theory, pure water) is obtained. Even though HBD process seems promising for desalinating produced water, it is still not technically feasible and economically viable mainly due to the low hydrate formation kinetics and the relatively high supplied energy. Accordingly, several researches have been carried out in order to get rid of these restraining aspects [8].

In an attempt to overcome these limitations, a French start-up called BGH recently patented a new HBD desalination process, denoted here as BGH process [10] in which porous activated carbon particles (PACP) are loaded with cyclopentane (CP) and immersed into the water to be desalinated at a suitable temperature. CP has the advantage of forming hydrates at atmospheric pressure and temperatures lower than about 7°C. Four main stages in BGH process can be distinguished: i) PACP loading with CP, ii) CP-hydrate formation, iii) separation of the CP-hydrate crystals from the remaining brine, and iv) dissociation of the separated CP-hydrate crystals. Although the preliminary results obtained by the start-up for produced waters are promising, a detailed understanding of the role of PACP and the mechanisms involved in hydrate formation is still required in particular to improve/optimize this process.

The purpose of the present work is to study the first two stages of BGH process while using model produced waters (NaCl brines at different concentrations). From there, the mechanisms governing the hydrate formation from CP-loaded PACP are investigated, and the main addressed issues are the hydrate formation and energetic aspects resulting from the use of the CP-loaded PACP. In summary, the objective of this thesis is to answer the following question: what is the role of the CP-loaded PACP in

hydrate formation (BGH process) compared to a conventional bulk CP-hydrate formation (classic HBD process)?

In order to reply to this question, the work plan of the thesis is to:

- make a literature survey to relate the state-of-the art on the investigations already conducted on HBD process, clathrate hydrates, adsorption/desorption phenomena and hydrate formation in presence of porous media.
- determine the CP-hydrate stability region and hydrate growth rate without PACP as a function of NaCl concentration.
- evaluate the effect of the main parameters (PACP size, pore size distribution, stirring rate, CP-loading rate and feed water salinity) of BGH process on hydrate formation.
- understand the prevailing mechanisms of hydrate formation from CP-loaded PACP (mainly the hydrate formation and energetic aspects).

This manuscript is organized in six chapters as follows:

Chapter 1 presents an overview of the conventional water desalination processes and research works already performed on hydrate-based desalination. It relates the state-of-art on clathrate hydrates, adsorption/desorption phenomena and hydrate formation in presence of porous media.

Chapter 2 is devoted to the description of the experimental techniques used in the present work. The techniques are categorized into three classes depending on the investigated system: i) virgin PACP, ii) CP-loaded PACP, and iii) CP-loaded PACP immersed in water at suitable conditions for hydrate formation.

Chapter 3 is dedicated to preliminary BGH-process investigation, starting from the effect of NaCl on CP-hydrate equilibrium temperatures and hydrate growth rate, to the evaluation of the BGH main parameters on hydrate formation kinetics and hydrate formed amount.

Chapter 4 investigates the relatively low hydrate amount formed (demonstrated in Chapter 3) through the study of CP-loading and unloading from the PACP under primary vacuum. This study is conducted

mainly through PACP characterization, generation of CP adsorption/desorption isotherms and determination of enthalpy of adsorption.

In Chapter 5, the insights obtained in Chapter 4 are employed so as to understand the mechanism(s) governing hydrate formation from the CP-loaded PACP and enhance hydrate formation (particularly the hydrate formed amount).

Chapter 6 tackles the energetic phenomena at stake resulting from CP-desorption and hydrate crystallization. From there, a thermal energy balance is investigated and quantified.

References

- [1] World Population Clock: 7.9 Billion People **2021** - Worldometer n.d. <https://www.worldometers.info/world-population/>
- [2] Babu P, Nambiar A, Chong ZR, Daraboina N, Albeirutty M, Bamaga OA, Hydrate-based desalination (HyDesal) process employing a novel prototype design, *Chem. Eng. Sci.* **2020**; 218:115563. <https://doi.org/10.1016/j.ces.2020.115563>.
- [3] Key World Energy Statistics 2020 – Analysis. IEA n.d. <https://www.iea.org/reports/key-world-energy-statistics-2020>
- [4] Abousnina R, An overview on oil contaminated sand and its engineering applications. *Int. J. geomate* **2015**; 10:1615–22. <https://doi.org/10.21660/2016.19.150602>.
- [5] Cha JH, Seol Y. increasing gas hydrate formation temperature for desalination of high salinity produced water with secondary guests. *ACS Sustain. Chem. Eng.* **2013**; 1:1218–24. <https://doi.org/10.1021/sc400160u>.
- [6] Islam MS, Sultana A, Saadat AHM, Islam MS, Shammi M, Uddin MK. desalination technologies for developing countries: a review, *J. Sci. Res.* **2018**; 10:77–97. <https://doi.org/10.3329/jsr.v10i1.33179>.
- [7] Younos T, Tulou KE, overview of desalination techniques: overview of techniques, *J. Contemp Water Res. Educ.* **2009**; 132:3–10. <https://doi.org/10.1111/j.1936-704X.2005.mp132001002.x>.
- [8] Babu P, Nambiar A, He T, Karimi IA, Lee JD, Englezos P, a review of clathrate hydrate based desalination to strengthen energy–water nexus. *ACS Sustain. Chem. Eng.* **2018**; 6:8093–107. <https://doi.org/10.1021/acssuschemeng.8b01616>.
- [9] Zheng J, Cheng F, Li Y, Lü X, Yang M. Progress and trends in hydrate based desalination (HBD) technology: A review. *Chin J Chem Eng* **2019**; 27:2037–43. <https://doi.org/10.1016/j.cjche.2019.02.017>.
- [10] Mottet B, Method for crystallising clathrate hydrates, and method for purifying an aqueous liquid using the clathrate hydrates thus crystallised, Applicant: BGH[FR]. EP3153606, <https://worldwide.espacenet.com/patent/search/family/054476876/publication/WO2017060456A1?q=PCT%2FEP2016%2F074044>.

Chapter 1. Generalities and state-of-the-art

1.1. Introduction

This thesis deals with hydrate formation from cyclopentane-loaded porous activated carbon particles. It falls in the context of produced waters desalination. In this chapter, produced waters are defined, their composition reported and the major conventional desalination processes described. As a potential desalination process, hydrate-based desalination is explained and compared with more conventional ones. A specific hydrate based-process, namely BGH which is the subject of investigation in this thesis, is described. Hydrate formation, as the main issue of the present work, is reviewed mainly in terms of nucleation and hydrate growth. Clathrate hydrates are defined and their main properties listed. In addition, due to the fact that cyclopentane is loaded in porous activated carbon particles, generalities on both porous media and adsorption phenomena are reported. Finally, a general view of hydrate formation in presence of solid materials namely porous media is given.

1.2. Clathrate hydrates

1.2.1. Definition

Clathrate hydrates (from “Klathron”: closure and “Hudor”: water), simply called gas hydrates, are crystalline compounds that visually resemble ice. They are formed under suitable temperature and pressure by inclusion of guest molecules (hydrate former), of suitable size (at most 9 Å), into a tridimensional framework (cavities or cages) made up of hydrogen-bonded water molecules (host) (Figure 1.1). The van der Waals interactions between the encapsulated guest molecules and the water

molecules stabilize the hydrate structure [1,2]. Common hydrate formers include light hydrocarbons, fluorinated compounds, noble gases, carbon dioxide, small ether molecules, and hydrogen [3]. Gas hydrates are generally non-stoichiometric compounds, *i.e.* they can be stable even if some cavities remain empty. Their occupancy, that is the ratio of the filled cavities on the total number of the cavities present in the structure, is reported around 0.7 (70%) [4].

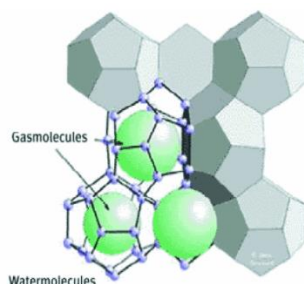


Figure 1. 1. General schematic representation of a clathrate hydrate. Taken from [5].

1.2.2. Main structures

Clathrate hydrates exist in three common distinct structures (Figure 1.2): cubic structure I (sI), cubic structure II (sII) and hexagonal structure H (sH), made of five different polyhedral cavities [1,2]. These latter are expressed as A^n , where A is the number of sides per face and n the number of faces.

Structure I:

A unit cell of sI hydrate consists of two 5^{12} and six $5^{12}6^2$ cavities, formed by 46 water molecules (see unit cell formula and Figure 1.2). Guest molecules are smaller than 6 Å such as methane, ethane, carbon dioxide and hydrogen sulfide.

Unit cell formula: $6X.2Y.46H_2O$, where X and Y corresponds to $5^{12}6^2$ and 5^{12} cavities, respectively.

Structure II:

A unit cell of sII hydrate consists of sixteen 5^{12} and eight $5^{12}6^4$ cavities made up of 136 water molecules. Large molecules (6 -7 Å) such as propane, iso-butane will form a structure II hydrate. Nitrogen and small molecules ($d < 4.2$ Å) are exception that form sII as single guests.

Unit cell formula: $8X.16Y.136H_2O$, where X and Y corresponds to $5^{12}6^4$ and 5^{12} , respectively.

Structure H:

A unit cell of sH consists of three 5^{12} , two $4^3 5^6 6^3$ and one $5^{12} 6^8$ cavities made up of 34 water molecules.

This structure is rare and is formed by a mixture of small molecules (4 - 5.5 Å) such as hydrogen sulfide, methane or nitrogen and large ones (8 - 9 Å) such as iso-pentane and neohexane.

Unit cell formula: $1X.3Y.2Z.34H_2O$, where X, Y, Z corresponds to $5^{12} 6^8$, 5^{12} , $4^3 5^6 6^3$, respectively.

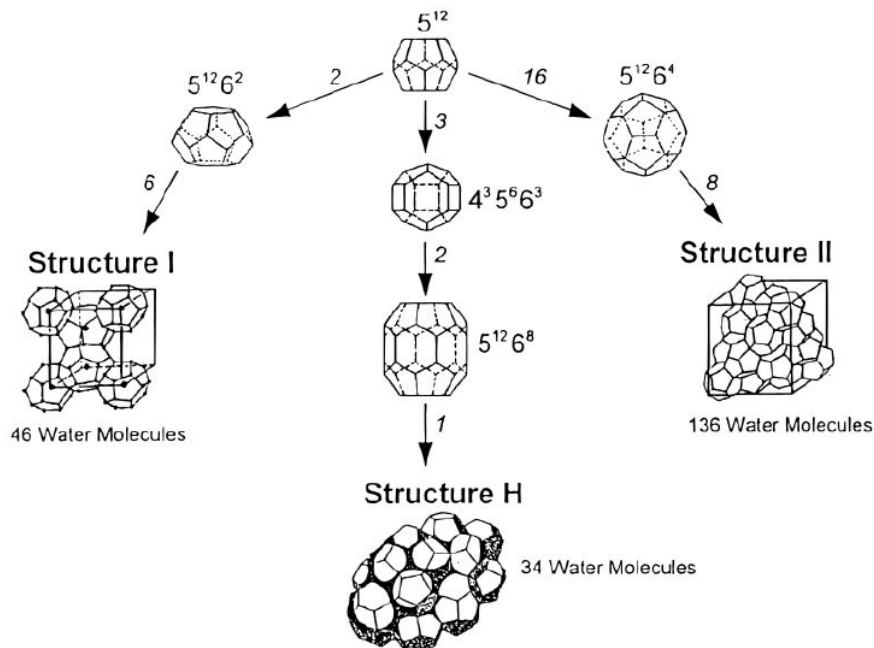


Figure 1. 2. Clathrate hydrate common structures. Taken from [1].

1.2.3. Hydration number

Hydration number n_H is defined as the ratio of the number of water molecules forming a gas hydrate unit cell and the number of enclathrated guest molecules in the cell [2]. It is expressed as follows:

$$n_H = \frac{\text{number of water molecules}}{\text{number of guest molecules}} \quad (\text{Eq. 1.1})$$

Hydration number depends on temperature, pressure, size and shape of the guest molecule [6]. The theoretical hydration number corresponds to a hydrate with all the cavities filled with the guest molecules. Accordingly, theoretical hydration number is calculated from unit cell formula (see section 1.2.2). It gives 5.75 for sI hydrates and 5.67 for both sII and sH hydrates.

1.2.4. Phase diagram

Phase diagram is a graphical plot that provides the thermodynamic conditions where the different phases of a given system are stable or coexist at equilibrium. Figure 1.3 shows the phase diagram of the system water – light alkane [2]. For example, the red curve presents the three-phase (hydrate (H), water (W), gas (V)) equilibrium curve of the system water-methane, whereas the left region depicts the hydrate stability zone.

In order to determine a gas hydrate phase diagram, equilibrium points can be experimentally determined. For that purpose, one must provide a proof of the hydrate phase absence or existence. Several methods and techniques can be used (Table 1.1) [6].

Table 1. 1. *Some methods/techniques used in the determination of gas hydrate equilibrium conditions.*

Method/technique	Brief description of some experimental protocols
Step-heating [7]	Gradual increase of temperature plateau (constant temperature during a given duration of time) until the observed hydrates disappear which corresponds to the equilibrium dissociation point
Abrupt slope change	Measurement of one parameter (temperature or pressure) within a reactor while varying the other one. The sudden change in temperature or pressure upon heating or depression indicates the dissociation of hydrate and thus the equilibrium point.
Differential scanning calorimetry	Increase of temperature until dissociating the hydrate phase. The corresponding thermal peak is interpreted to obtain the equilibrium point.

Equilibrium curves can also be calculated after modeling the phase equilibria of the given gas hydrate using thermodynamic approaches such as “Hildbrand and Scott” or “van der Waals and Platteeuw” theory [8].

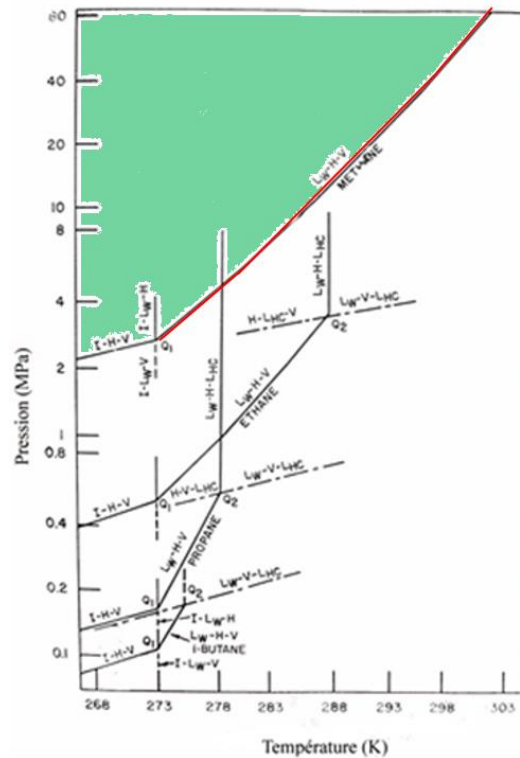


Figure 1. 3. Pressure – temperature phase diagram of pure water-light alkane system. Adapted from [2].

1.2.5. Hydrate formation

As mentioned above, gas hydrate crystallization (formation) requires primarily presence of water (host molecules), guest molecules (CO_2 , CP, CH_4 , etc.) and suitable thermodynamic conditions (T typically $< 20^\circ\text{C}$), and high pressure (P typically > 30 bar) [5]. Nonetheless, fulfilling the previous conditions does not ensure hydrate formation. Indeed, favorable kinetic conditions are required, mainly hydrate nucleation for hydrate formation initiation and sufficient mass and heat transfer for hydrate growth.

1.2.5.1. Driving force

Considering a closed system (solvent + solute i) where the solute is transforming from a solubilized state (L) to a solid state (S) at constant temperature and pressure, the equilibrium state can be expressed by the equality of the chemical potential of the solute in both states (Equation 1.2).

$$\mu_{i,eq}^L = \mu_{i,eq}^S \quad (\text{Eq. 1.2})$$

where $\mu_{i,eq}^L$ and $\mu_{i,eq}^S$ are the chemical potential of the solute at equilibrium within the liquid and solid phases, respectively.

Providing that for a system out of equilibrium, the solute migrates towards the phase where its chemical potential is the lowest, the driving force of crystallization can be defined as the difference of chemical potentials as follows:

$$\Delta\mu_i = \mu_i^L - \mu_i^S \quad (\text{Eq. 1.3})$$

The driving force is governed by the solute supersaturation since at this state, the system tends to achieve equilibrium by crystallizing the solute. It can be expressed as follows:

$$\Delta\mu_i = k_b T \ln \frac{c}{c_{sat}} = k_b T \ln(A) \quad (\text{Eq. 1.4})$$

where k_b , T , c , c_{sat} and A are the Boltzmann constant, the temperature, the solute concentration, the solute concentration at saturation and the supersaturation ratio, respectively.

In order to form hydrate, the supersaturation is obtained through an isobaric cooling or isothermal compression of the system “water + hydrate former” under the equilibrium temperature or above the equilibrium pressure dictated by the phase diagram (see section 1.2.4).

One of the common expressions of the driving force was given by Vysniauskas and Bishnoi and Arjmandi *et al.* (2004) [9,10]. They expressed it as the difference between the equilibrium temperature and the experimental one (Equation 1.5). This quantity is named supercooling but commonly known as “the subcooling”.

$$\Delta T = T_{eq} - T_{exp} \quad (\text{Eq. 1.5})$$

The concept of supersaturation is important to understand hydrate nucleation and growth. It governs these processes and defines the crystals purity, morphology and size [6] and thus, one can understand that hydrate formation depends significantly on the imposed subcooling.

1.2.5.2. Nucleation

Hydrate nucleation is the first step of hydrate formation. It can be defined as the process where nuclei (microscopic clusters, germs or embryos) grow and disperse so as to achieve a critical size (commonly

denoted as super nuclei or critical nuclei) allowing the development of hydrate crystals. The time taken for critical-nuclei formation is known as induction time. Depending on the prevailing mechanism, nucleation is classified into 2 types : primary and secondary nucleation [6,11–13] (Figure 1.4).

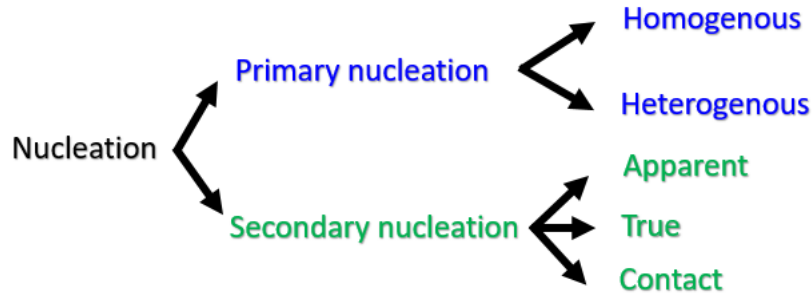


Figure 1. 4. Types of hydrate nucleation.

1.2.5.2.1. Primary nucleation

Primary nucleation takes place in absence of solute-particle interfaces (*i.e.* particle with chemical and physical nature similar to that of hydrate, namely fragment of hydrate crystals). Solute (gas) molecules within solute-supersaturated aqueous solutions combine to produce nuclei due to the higher chemical potential of dissolved molecules compared to the enclathrated ones. After series of formation-dissolution while adding more molecules, the nuclei reach a critical size r_c allowing a spontaneous growth as dictated by the classical nucleation theory. Indeed, the birth of the nuclei results in the creation of two antagonist energies: surface and volume Gibbs free energies (see equation 1.6, which is established assuming spherical nuclei of radius r).

$$\Delta G = \Delta G_{surface} + \Delta G_{volume} = 4\pi r^2 \gamma - \frac{3}{4} \pi \frac{r^3}{V_m} k_B T \ln A \quad (\text{Eq. 1.6})$$

where V_m and γ are the molecular volume and the surface tension between hydrate crystal and water respectively.

As the nuclei grow, due to the supersaturation (driving force), they reach the critical size corresponding to the critical Gibbs free energy ΔG_{crit} (Figure 1.5). This latter presents an energy barrier and requires an energy amount, known as activation energy, to be overcome. The germs larger than the critical size, will further grow to form macroscopic hydrate crystals.

Two categories of primary nucleation can be distinguished: homogenous nucleation and heterogeneous nucleation. The former takes place in the water bulk phase whereas the latter occurs on a foreign surface *i.e.* with chemical and/or physical nature different from that of hydrate crystals, such as a reactor wall, a stirrer or the water/gas interface. The fact that heterogeneous nucleation is induced by a foreign surface, which has a lower surface energy than three-dimensional bulk water, decreases the critical Gibbs free energy. Therefore, the required driving force is reduced. Accordingly, heterogeneous nucleation is more frequent than the homogeneous one.

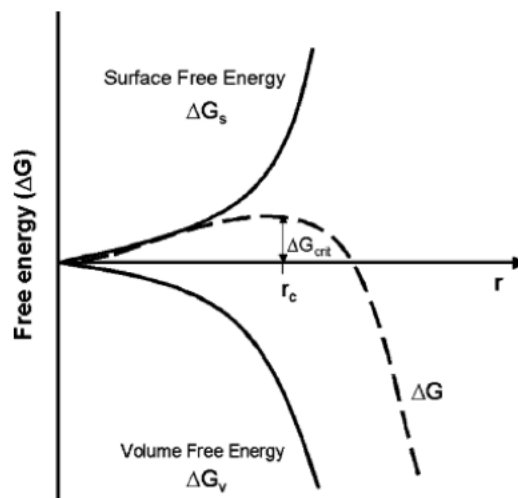


Figure 1. 5. Gibbs free energy evolution for primary nucleation process as dictated by the classical nucleation theory. Taken from [13].

1.2.5.2.2. Secondary nucleation

This type of nucleation relies on the active participation of solute-particle interface, that is the presence of hydrate crystals in water. Even though the exact mechanism is no well-defined, various scenarios of secondary nucleation, known as “apparent”, “true” and “contact” are distinguished [6,12]:

- apparent secondary nucleation: it occurs when crystalline fragments larger than the critical size are added to the system. This operation is commonly known as “seeding”.
- true secondary nucleation: the mechanism relies on the solute-particle ripening. The nuclei are created by the interaction between water and a hydrate crystal. Indeed, this latter disrupts the equilibrium of the nuclei and allows aggregates smaller than a critical size to evolve towards stable nuclei (*i.e.* super nuclei).

- contact secondary nucleation: is a consequence of the residual fragments resulting when a growing hydrate crystal collides with another surface such as the container wall, the stirrer or another hydrate crystal.

1.2.5.3. Growth

Once nucleation is produced, the critical nuclei grow spontaneously by incorporating water and hydrate former. The system evolves towards a thermodynamically stable state as long as a driving force is applied. Hydrate growth can be described at different size levels: molecular, microscopic and macroscopic scales. At a molecular level, the crystals surface hosts the atoms involved in hydrate formation, so called “growth units”. These latter either diffuse across the surface and eventually incorporate the crystals or return to the solution depending on the nature of crystal-solution interface. On a microscopic level, hundreds of molecular layers grouped together trap water inside the crystals structure. At the macroscopic level, heat transfer and mass transport are the governing phenomena. Mass transport is considered as a limiting factor since it is relatively slow compared to heat transfer. According to Elwell and Sheel (1975), mass transport limitations most often control hydrate growth [12,14]. Hence, hydrate formation takes place at a low kinetics (growth rate). Gas hydrates may grow under several configurations namely, single crystal growth and film/shell at the water-guest interface [11]. They are assumed to grow in the aqueous phase. Their crystallization is an exothermic phenomenon. As heat transfer is relatively fast, the released heat is generally evacuated rapidly from the hydrate surface so that to enable its growth [6].

1.2.5.4. Metastability and memory effect

As mentioned in section 1.2.5.2.1, the nuclei critical size corresponds to a critical Gibbs free energy. At this stage, the nuclei are at an unstable equilibrium and thus they grow or dissolve depending on whether an entity is added ($r > r_c$) or removed ($r < r_c$) as both cases correspond to a decrease of the free Gibbs free energy of the system (see Figure 1.5). Accordingly, it exists a metastable region where nucleation is not spontaneous [6]. As a consequence, the induction time in this region is stochastic and can be very

long. This zone is less pronounced in the case of a solution that has already seen hydrate formation where the melting temperature and/or time were moderate and/or short, respectively. This phenomenon is known as “memory effect”. It may be explained through two reported hypotheses: i) residual hydrate structures (partial hydrate cages or polyhedral clusters) remain in the solution after hydrate dissociation, therefore, hydrate nucleation is produced more easily, and ii) the solution is supersaturated as a consequence of the dissolved guest molecules from the dissociated hydrate. The use of memory effect is convenient to reduce the induction time [11].

1.2.6. Enthalpy of dissociation

The enthalpy of formation/dissociation of clathrate hydrates is defined as the amount of heat released/absorbed during their formation/dissociation. Calorimetry is considered as the most reliable method for determining gas hydrate dissociation enthalpy. Nonetheless, this latter can be obtained otherwise through the use of equations and correlations such as Clausius-Clapeyron equation [6]:

$$\frac{d \ln(p)}{1/T} = - \frac{\Delta H}{zR} \quad (\text{Eq. 1.7})$$

where p is the equilibrium pressure, T the equilibrium temperature, ΔH the dissociation enthalpy, z the compressibility factor and $R = 8.31 \text{ J/K/mol}$ the universal gas constant.

Table 1.2 reports the range of dissociation enthalpies of some gas hydrates determined by differential scanning calorimetry or calculated with Clausius-Clapeyron equation [6].

Table 1.2. *Dissociation enthalpies of some gas hydrates.*

	Dissociation enthalpy (kJ/mol of hydrate former)
CH ₄ hydrates	52 - 58
CO ₂ hydrates	57 - 73
N ₂ hydrates	46 - 66

1.2.7. Effect of inorganic salts

Inorganic salts such as NaCl were reported to act as both thermodynamic and kinetic inhibitors of hydrate formation [15]. Indeed, it was found that the presence of salt lowers the equilibrium temperatures and slows down both nucleation and growth rate of clathrate hydrates such as cyclopentane

and mixed cyclopentane-methane hydrates [8,16–18]. On the one hand, the thermodynamic effect of salt can be explained by the severe interactions between salt and water molecules (ion-dipole interactions) compared to the interactions between water molecules (van der Waals forces and hydrogen bonds). The hydration of salt ions through the so called “ion clustering” reduces the solubility of the guest molecules in water, a phenomenon known as “salting-out”. On the other hand, the kinetic effect of salt can be explained by the so called “concentration-polarization effect”. Indeed, salt ions are excluded during hydrate formation in brine since they do not participate to the hydrate structure. The excluded ions accumulate in the vicinity of the formed hydrate crystals. Therefore, the driving force (subcooling) locally decreases which slows down the hydrate formation kinetics [15,19].

1.2.8. Morphology

The morphology of gas hydrate crystals is defined by their shape and size. It depends mainly on the applied subcooling [20] and the presence of additives such as surfactants [21]. Kishimoto *et al.* (2012) found that hydrate crystals morphology is not significantly affected by the presence of salt. Furthermore, their results showed that the size of hydrate crystals decreases with increasing imposed subcooling [17]. Han *et al.* (2017) reported the general trend of hydrate crystal morphology as a function of subcooling (Table 1.3) [20].

Table 1.3. Hydrate crystal morphology as a function of subcooling.

Subcooling (°C)	Morphology
≤ 2	Polygons
2 - 3	Polygon-skeletal
≥ 3	Sword-like or triangular dendrites

1.2.9. Main areas of study

Hydrate crystallization has been widely studied in the literature in different contexts such as hydrate formation within natural sediments [7,22,23], flow assurance [24–26] and potential industrial applications (hydrate-based processes) [3,4,15,19,27–29]. A significant number of water-guest systems

and setup designs have been studied mainly to describe hydrate formation mechanisms [30,31] or hydrate crystals morphology [21,32,33], to promote [34,35] or inhibit [24,36] hydrate formation, and to reduce the energy supplied for hydrate crystallization [37–41]. Hereafter, we focus on the enhancement of hydrate formation kinetics and the hydrate based-applications.

1.2.9.1. Enhancement of hydrate formation kinetics

Several studies have been conducted to enhance hydrate formation kinetics mainly in the context of attempting successful hydrate-based processes at industrial scale. The investigated methods are based on: i) co-guests such as cyclopentane [15], cyclohexane [27], tetrahydrofuran [42], and carbon dioxide [43]; ii) enhanced formation conditions (mainly by increasing the subcooling) [36]; iii) memory effect [44]; iv) new methods/protocols such as LNG cold energy utilization [37,38], innovative reactor designs (stirred vessel, bubble column, spray column [3,4]); v) chemical compounds (surfactants: SDS, SDBS, APG [4], polymers [15]); vi) solid materials (silica sand, silica gel, activated carbons, nanoparticles, dry water, dry gel [31], graphite [34]).

1.2.9.2. Hydrate-based applications

Besides hydrate-based desalination technology presented below in section 1.4.2.1, gas hydrates present various potential applications [6] as a consequence of their ability to trap gases. Indeed, the high trapped amount of methane (about 170 times the volume of methane at standard conditions), made them a potential tool for natural gas storage. The formed methane hydrates can be transported at higher temperature compared to that required for liquefying natural gas. Formation of CO₂ hydrates in deep underground reservoirs or deep oceans, where suitable conditions prevail, could be exploited in carbon dioxide sequestration after being captured from the atmosphere. The so-called secondary refrigeration, where cold is produced with gas hydrates (*e.g.* TBAB and CO₂ hydrates) in a centralized and confined unit, could be employed in order to limit the use of conventional harmful refrigerants (*e.g.* chlorofluorocarbons). Finally, the selective property of gas hydrates, that is trapping some gases in

detriment of others, could give rise to gas-separation applications where less energy is supplied compared to conventional adsorption-based processes. It should be noted that the list of the covered applications is not exhaustive.

1.2.10. Cyclopentane hydrates

Cyclopentane hydrates are clathrate hydrates where guest molecules are cyclopentane (CP) and host molecules are water (Figure 1.6). CP, whose chemical formula is C_5H_{10} , is a cyclic alkane of low solubility in water (86 mg/L at $10^\circ C$ [27]). They form at atmospheric pressure and a temperature lower than $7.1^\circ C$ in pure water [8]. These accessible thermodynamic conditions made CP hydrates interesting model hydrates for laboratory investigations [45].

CP is known to form sII hydrates, where CP occupies only the 8 large cavities ($5^{12}6^4$) of the unit structure. Accordingly, it presents a hydration number of 17 ($=136:8$), in other words, a stoichiometric CP/water molar ratio of 17:1. Kishimoto *et al.* (2012) obtained several CP-hydrate morphologies as a function of the imposed subcooling (Table 1.4) [17].

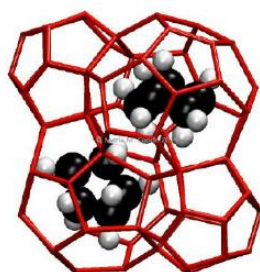


Figure 1. 6. CP-hydrate structure. Taken from [45].

Table 1. 4. Morphology of CP-hydrate crystals as function of subcooling.

Subcooling ($^\circ C$)	Morphology
1.4 – 2.4	Polygonal
2.4 – 3.5	Triangular
>3.5	Sword-like

Ho-Van *et al.* (2018) plotted equilibrium points of CP-hydrates in presence of several salts (NaCl, KCl, NaCl-KCl and $CaCl_2$) using what they called a “slow procedure” (Figure 1.7) [8]. The dissociation

enthalpy of CP-hydrates was determined by Zhang *et al.* (2004) and Nakajima *et al.* (2008) who obtained 82.3 ± 4 kJ/mol of CP and 106.9 kJ/mol of CP, respectively [46,47]. Recently, Delroisse *et al.* (2018) obtained an enthalpy dissociation of 115.4 ± 7.6 kJ/mole of CP by using a stirred calorimetric cell [45]. Ho-van *et al.* (2019) devoted a review paper to the use of CP as a hydrate former for hydrate-based desalination. They concluded that, even though challenges need to be overcome, CP-hydrate-based desalination process could be a promising alternative to the traditional desalination processes due to the fact that it operates under atmospheric pressure and requires lower energy supply [15].

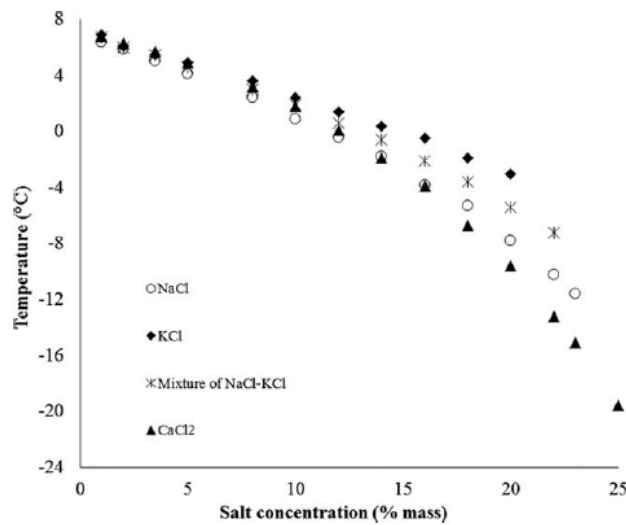


Figure 1. 7. Equilibrium temperatures of CP-hydrates vs. salt concentration. Taken from [8].

1.3. Produced water

1.3.1. Definition

Produced water (PW) is defined as the water co-produced with oil and gas during extraction process [48,49]. As it is in contact with hydrocarbon and geologic formations in underground basins, it usually contains high concentrations of both inorganic and organic compounds [50]. Indeed, the total dissolved solids (TDS) of PW, which is a measure of the total concentration of dissolved organic and inorganic matter in water (ASTM D5907-13), varies between 1,000 and 400,000 mg/L (0.1 and 28.5 wt% TDS) depending on the nature of the reservoir and the resource produced. Cha and Seol (2013) reported an

average TDS of 89,000 mg/L (8.2 wt% TDS) for PW, calculated from 58,707 entries of a database of oil and gas fields provided by the United States Geological Survey (USGS) [27]. PW is produced in very large amounts. Actually, it is considered as one of the largest streams of wastewater produced in oil and gas industry, globally estimated to be around 210 million barrels per day and greater than 70 billion barrels per year in the world [49,51]. It represents around 75% of the total effluents (three barrels of water for one barrel of oil [52]) and around 70% of the total wastewater produced during oil production [48]. Volume of produced water could reach 98% in nearly depleted fields with only 2% of fossil fuel production. Hence, it is expected that the PW to produced-oil ratio would be 12 (v/v) by 2025.

1.3.2. Composition

PW contains a mixture of dissolved and particulate organic and inorganic compounds. Its composition depends on several factors: geologic location of the field, age and depth of the basin, geochemistry of the formation, extraction process and both type and composition of the produced hydrocarbons. The major components of PW are salts, measured as salinity, mainly sodium cations (81% of the total cations) and chloride anions (97% of the total anions) in conventional wells, polyaromatic hydrocarbons, benzene, toluene, ethylbenzene, xylene, oil and grease, organic acids, phenols and compounds causing scaling such as calcium [49]. Table 1.5 presents the main constituents of a PW.

Table 1.5. Main components of PW. Adapted from [49].

Parameter	Concentration (mg/L)	Parameter	Concentration (mg/L)	Parameter	Concentration (mg/L)
COD	1,220-2,600	BTEX	0.73-24.1	Cl ⁻	0-270,000
TSS	1.2-1,000	Phenol	0.001-10,000	Ca ²⁺	0-74,000
TOC	0-1,500	Oil and grease	2-560	SO ₄ ²⁻	0-15,000
TDS	1,000-400,000	Na	0-150,000	Mg ²⁺	0.9-6,000
Glycol	7.7-2,000	Ba	0-850	HCO ₃ ⁻	0-15,000

1.3.3. Management

Nowadays, the huge amounts of PW make its management a necessity [49]. Indeed, PW can be either reinjected into the producing reservoir (to sustain reservoir pressure or for hydraulic fracturing operations), injected into disposal wells (proper aquifer) and/or discharged into surface water bodies

(very often into seawater). Reinjection of PW is the preferred management option since it allows both enhanced oil production and lesser environmental impact. Rejected and discharged PW can be desalinated to avoid possible compatibility issues with formation water [48], to enhance oil production [53] or to meet local regulations (*e.g.* COPs). Around two thirds of PW were reported to be reinjected in wells and one third discharged in aquifers and surface water [48]. According to Abousnina *et al.* (2015), more than 44 million barrels/day are discharged into the sea [52]. Table 1.6 depicts the standards for reusing PW in gas industry [49]. Accordingly, the content of PW, provided in Table 1.5, should be reduced through desalination processes to meet the recommended values (Table 1.6).

Table 1. 6. Standards for PW reuse in gas industry. Adapted from [49].

Parameter	Recommended maximum values (mg/L)	Parameter	Recommended maximum values (mg/L)
TSS	50	Chloride	45,000
TOC	25	Calcium	8,000
TDS	50,000-65,000	Sulfates	50
Sodium	36,000	Iron and barium	10

1.4. Water desalination processes

The use of desalination as water treatment method has been increased over the past 50 years. The first researches in this domain were conducted during the World War II, but desalination technologies appeared in 1960. They were based on thermal processes. In the later 1960s, membrane processes emerged in the desalination market. These processes have been developed since the 1980s. Recently, shortage in freshwater and environmental concerns have led to an increase in the world desalination demand, which has resulted in a growth of the world desalination capacity. In this decade, global desalination capacity is expected to reach 100 million m³ per day [54]. Thus, desalination market has rapidly grown over the past decade and is expected to continue growing in the coming decades (Figure 1.8).

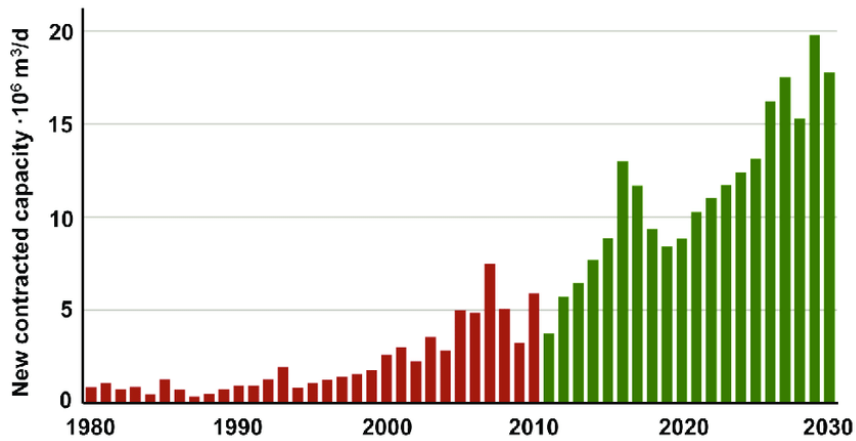


Figure 1. 8. History and forecast annual growth of desalination market. Taken from [55].

1.4.1. Major desalination processes

In this part, we describe the most commercially-used desalination processes [54] (Figure 1.9) and hydrate based-desalination process as the context of this thesis.

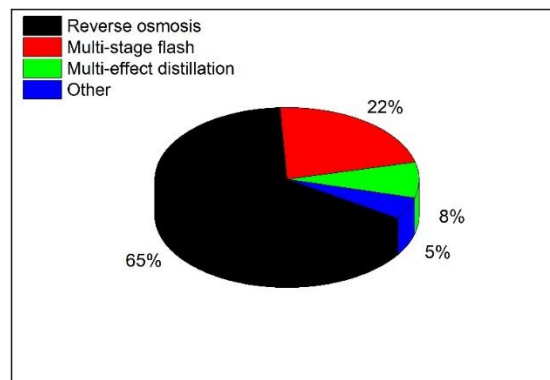


Figure 1. 9. Global contracted capacity by technology in 2013.

1.4.1.1. Thermal technologies

This technology is based on water distillation. We distinguish two main processes: Multi-stage flash and Multi-effect distillation.

1.4.1.1.1. Multi-Stage Flash (MSF)

In this process, feed water is heated and circulated through chambers with successively decreased pressure (Figure 1.10). Therefore, the boiling temperature is decreased and a fraction of water evaporated (flash evaporation). The resulted steam is collected and condensed into a very low salinity distillate (< 50 mg/L TDS). While the feed water salinity does not impact significantly the incurred costs of MSF, the installation and operating costs are noticeable [54,56].

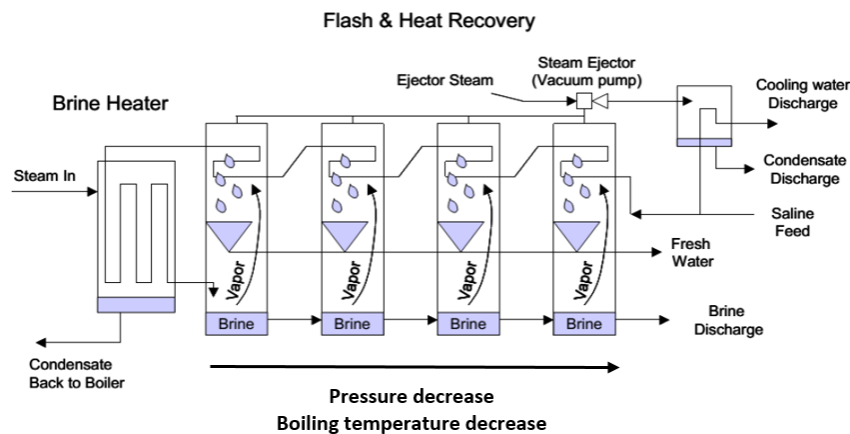


Figure 1. 10. Multi-stage flash principle. Adapted from [54].

1.4.1.1.2. Multi-Effect Distillation (MED)

In this process, feed water is sprayed over heat exchange tubes which provokes steam generation (Figure 1.11). This latter flows through the tubes and finishes by condensing to pure water. The heat energy released from steam condensation causes a fraction a feed water to evaporate outside of the tubes. The resulted steam is introduced in the tube of the next chamber, called an “effect”, operating at a slightly lower pressure. The quality of the produced water is similar to that produced by MSF. Even though MED is technically improved than MSF (lower thermal and electric energy), it lost favor due to the problems of scaling on the heat transfer tubes [54,56].

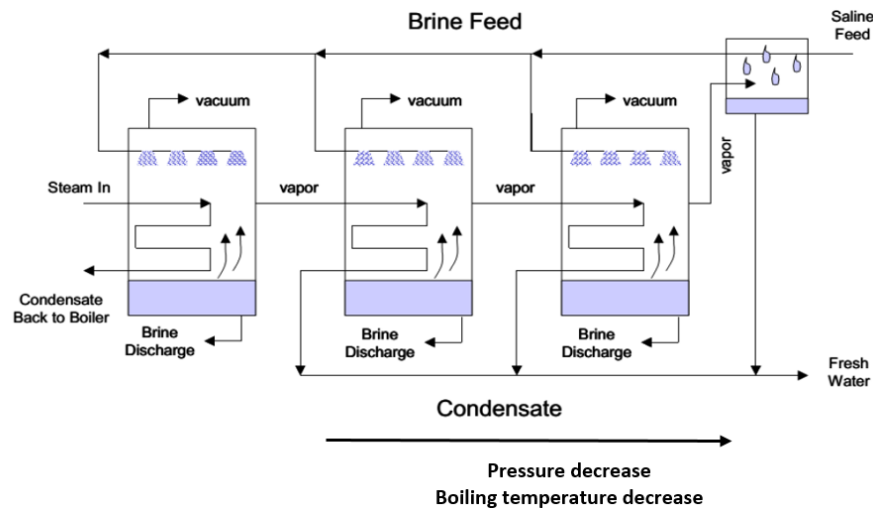


Figure 1. 11. Multi-effect-distillation principle. Adapted from [54].

1.4.1.2. Membrane technologies

They owe their name to the use of membranes for water desalination. Several membrane processes are distinguished namely nanofiltration, electrodialysis and reverse osmosis. As depicted in Figure 1.9, this latter is the most deployed process with 65% of the global contracted capacity. Reverse osmosis (RO) uses the osmosis phenomenon to remove salt from water. Osmosis occurs when two solutions of different solute concentrations (here salty and pure water) are separated with a semi-permeable membrane (Figure 1.12a). This process relies on applying, on the salty water, a pressure greater than the osmotic pressure ($\Delta\pi$) in order to reverse the flow. This allows pure water to flow through the membrane and separates from salts (see Figure 1.12b) [57] resulting into two streams: a high quality and a salt concentrated “reject” streams. The amount of applied pressure is correlated with the feed water TDS [57]. Indeed, for brackish water (1,000-10,000 mg/L) and seawater (35,000 mg/L), a pressure range of 15 to 20 bar and 54 to 80 bar is required, respectively [54]. RO must be preceded by filtration to remove large particles and suspended solids that would otherwise foul and damage the polymeric membranes. It also often requires the use of chemical additives to prevent or alleviate scaling and biological fouling. According to Younos and Tulou (2009), RO is effective when feed water TDS is lower than 45,000 mg/L (typically brackish and seawater) [57]. For higher TDS (as typically in the case of PW), Cakmakce

et al. (2008) reported a cost between 5.19 and 5.98 \$/m³ water, roughly ten times higher than the treatment cost of seawater (see Table 1.7 below) [48,58].

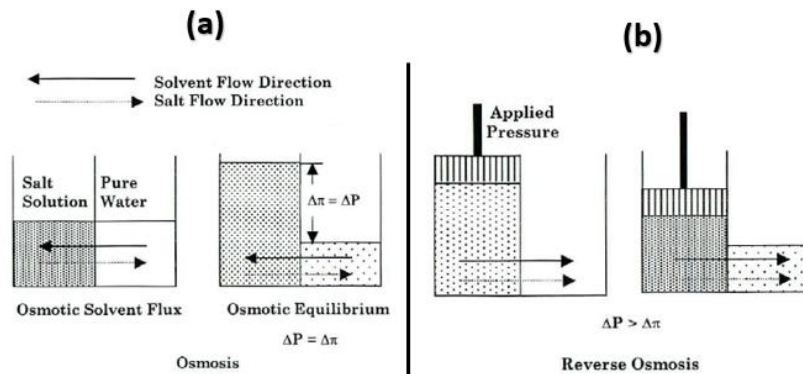


Figure 1.12. RO principle. Taken from [57]
(a) osmosis phenomenon, (b) reverse osmosis principle.

1.4.2. Hydrate-Based technologies

1.4.2.1. Description

HBD was proposed in the 1940s and received considerable attention in the 1960s and 1970s [3,43]. Indeed, it could be a cheaper alternative to the traditional thermal and membrane desalination processes [59]. HBD is classified as a freezing-crystallization technique. Therefore, it is based on a liquid-to-solid phase change and the fact that the ions present in the liquid phase are excluded from the solid phase formed. The hydrate former is added to the system so that to crystallize water to gas hydrate rather than ice. Because gas hydrates can crystallize at temperature higher than 0 °C (ice normal melting temperature), the process should require less energy [20]. Once the gas hydrates have formed, the hydrate crystals are separated from the remaining brine, in which salts are concentrated. The separated crystals are then melted and desalinated water is obtained. Melting of one cubic meter of gas hydrates can produce up to 0.8 m³ of pure water (and 164 m³ of guest) at standard temperature and pressure [5]. A HBD process consists in cycle(s) of crystallizing-melting of gas hydrates. It includes three main steps [3,60] as shown in Figure 1.13:

- **Gas hydrate formation (crystallization):** under the suitable pressure and temperature, determined from the equilibrium conditions of the gas hydrates formed, gas hydrate crystallization is

performed in a chemical reactor. Because salts do not participate to the hydrate structure, the salinity of the unconverted water increases gradually with the amount of gas hydrate formed, until reaching a value that corresponds to the thermodynamic equilibrium state of the system “salt water + guest + hydrate”.

- **Separation / filtration:** a physical process such as vacuum filtering is used to separate the formed hydrate from the remaining salty concentrated liquid (brine). Usually other techniques (*e.g.* centrifugation, washing, sweating, etc.) called post-treatment methods are used at this stage to enhance the separation/filtration efficiency.
- **Gas hydrate dissociation (melting):** The separated hydrate crystals are melted by decreasing the pressure below the hydrate equilibrium pressure and/or increasing the temperature above the hydrate equilibrium temperature. Thus, desalinated water is obtained.

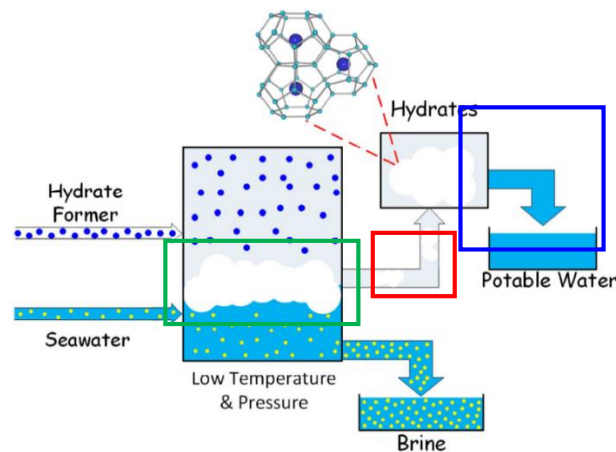


Figure 1. 13. HBD concept. Adapted from [3].

1.4.2.2. Comparison of HBD with the major desalination processes

The comparison of the major processes used in desalination market with HBD is reported in Table 1.7. This latter is taken from Babu *et al.* (2018) and adapted by the author. From there, one can infer that HBD could be an alternative process for high TDS water desalination.

Table 1. 7. Comparison of HBD, MSF and RO processes.

Process	Advantages and limitations	Water recovery (%)	Salt removal	Cost (\$/m ³ of water)	Energy consumption (kWh/m ³ of water)
MSF	<ul style="list-style-type: none"> - Applicable for high TDS - High energy cost - Low water recovery 	Up to 20	Treated water TDS <50 ppm [54]	1.10 – 1.50	13.5 – 25.5
RO	<ul style="list-style-type: none"> - Applicable for low TDS [56] (up to 45 g/L [57]) - Applied pressure: 50 to 80 bar - Very sensitive to impurities - Requires pretreatment - Frequent replacement of membrane. - Low water recovery 	Up to 55	90 – 99 % [61]	0.45 – 0.92 0.46 – 0.79 [58]	1.85 – 36.3
HBD	<ul style="list-style-type: none"> - Applicable for high TDS - Low maintenance - High water recovery 	NA	60 – 93 % [60]	0.46 – 0.52	0.6 – 65.29

1.4.2.3. Development and challenges of HBD technology

In an attempt to succeed an industrial application of HBD process, this latter has been developed since its emergence. Babu *et al.* (2018) reported the timeline research progress of HBD (Figure 1.14).

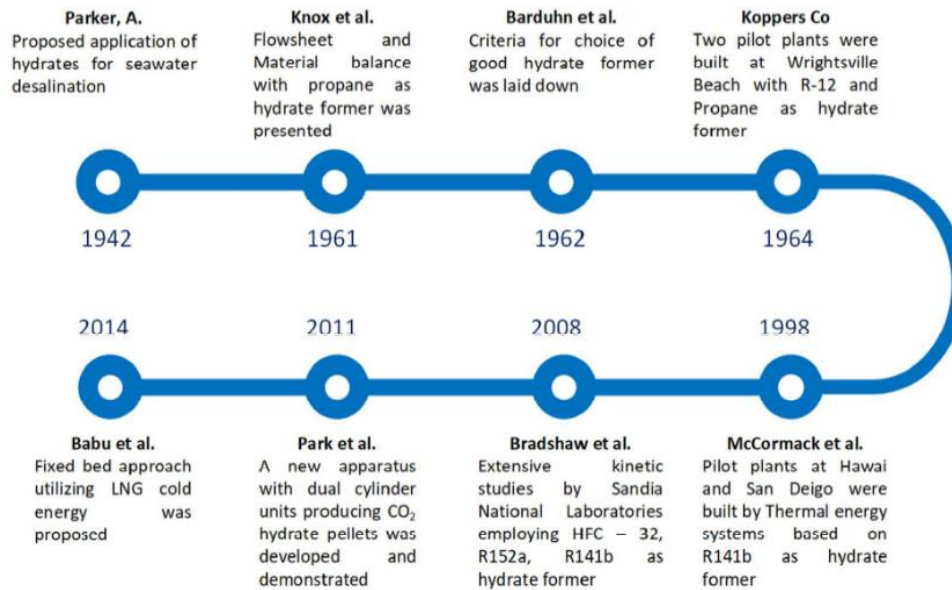


Figure 1. 14. HBD research progress over time. Taken from [3].

Even though the noticeable progress, HBD still suffers from various limitations. Several authors reported that the main reasons that prevent HBD from being developed at industrial scale are [3,4,15,43,60]:

- hydrate formation slow kinetics: very often due to the limited contact area between the water phase and the guest (which generally has a very low solubility in water), thus limiting the mass transfer between the two phases.
- difficult separation of hydrate crystals from brine: on the one hand, salt adheres to the separated- crystal surface (concentration-polarization effect) which reduces the removal salt efficiency. On the other hand, the non-separated crystals, which remain within the residual brine, and thus would not be melted, lowers the water recovery *i.e.* the fraction of the obtained desalinated water.
- relatively high supplied energy: it encompasses the energy supplied for hydrate formation, crystals separation (filtration, etc.) and post-treatment methods used for enhancing the salt removal efficiency (washing, sweating, etc.).

According to Fakharian *et al.* (2017) no HBD pilot-plant exists yet [19]. Park *et al.* (2011) reported that the Bureau of Reclamation in the US sponsored a preliminary study, followed by a pilot test conducted at the Natural Energy Laboratory of Hawaii.

1.4.2.4. BGH process

In 2015, a French startup called BGH patented a hydrate-based desalination process here denoted as “BGH process” [62]. This latter was devised in an attempt to overcome the challenges and limitations that prevented HBD from acting at commercial/industrial scale (see section 1.4.2.3).

BGH process relies on the concept of HBD technology but with the added innovation of using PACP soaked in CP which can form gas hydrates at atmospheric pressure. As in HBD (see section 1.4.2.1), CP hydrates are formed then dissociated in order to obtain the desalinated water. The CP released during the hydrate dissociation is recycled and the PACP regenerated to be reused (Figure 1.15). The governing mechanisms and phenomena of the hydrate formation stage are not understood yet and should be investigated so that better control and optimization of the process could be achieved.

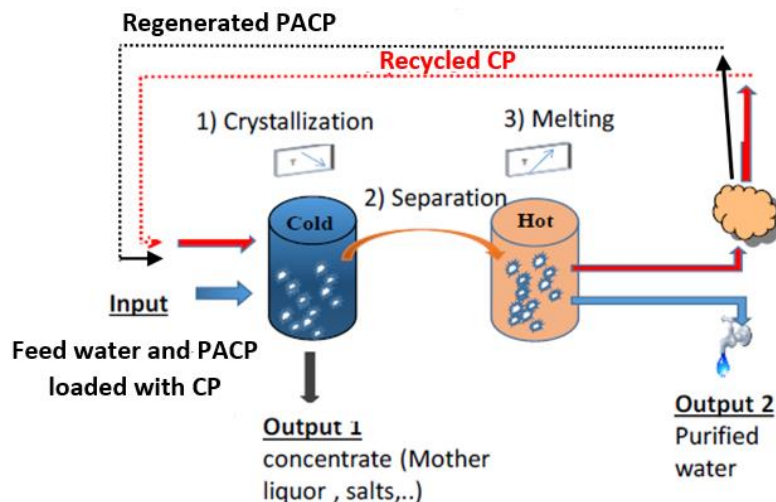


Figure 1. 15. BGH process concept. Taken from BGH startup.

1.5. Porous media

1.5.1. Definition

A porous medium can be defined as a material containing empty spaces called pores. It can be either consolidated or unconsolidated. The former is a confining solid formed by cemented grains or monoliths whereas the latter are characterized by the absence of grains bonds and thus form packed beds. Porous media are often used as adsorbents due to their high specific surface area [63].

1.5.2. Main Characteristics

1.5.2.1. Porosity

Porosity can be defined as the ratio of the pore volume V_P to the total volume V_T of the porous medium [63] (Equation 1.8).

$$\phi = \frac{V_P}{V_T} \quad (\text{Eq. 1.8})$$

Pores can be either interconnected or isolated. From there, several pore types can be distinguished: through pores, open pores, closed pores, dead-end pores and ink-bottle pores (Figure 1.16).

According to IUPAC classification, the pore size are classified into three categories [64]:

- Micropores: pores with sizes lower than 2 nm
- Mesopores: pores with sizes between 2 nm and 50 nm
- Macropores: pores with sizes exceeding 50 nm

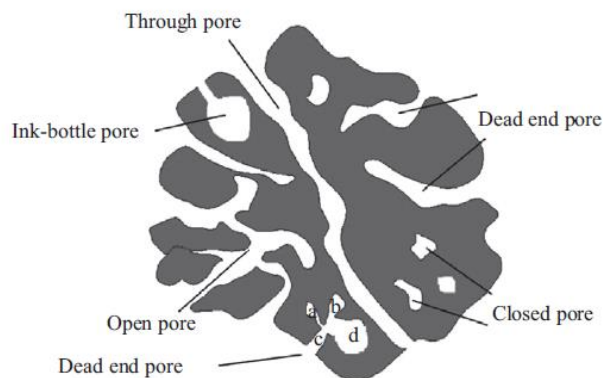


Figure 1. 16. Pore features in coal. Taken from [65].

1.5.2.2. Pore size distribution

The porous structure of a given adsorbent can be described with the so-called pore size distribution (PSD). It is deduced from the derivation of the cumulative pore volume (PV) obtained either with gas or mercury intrusion porosimetry (see sections 2.3.1.2 and 2.3.1.3 in Chapter 2). Therefore, it corresponds to the distribution of the pore volumes according to their widths. PSD can be seen as one of the most important quantitative characteristics of porous media since it is involved in transport and equilibrium phenomena. According to their PSD, porous media can be either specific or non-specific. The former presents a very narrow mono-disperse PSD and considered as molecular sieve (*e.g.* zeolites), whereas the latter present a polydisperse PSD (*e.g.* activated carbons).

1.5.2.3. Specific surface

A solid surface reported to a solid amount, generally mass, is known as specific surface. It corresponds to both the external and pore wall surfaces. The surface of a solid can be defined in three different ways [64] (Figure 1.17) :

- van der Waals surface (1): formed by the outer part of the van der Waals spheres of the surface atoms.
- Connolly surface (2): known as the probe accessible surface, that is the surface drawn by the bottom of a spherical probe molecule rolling over the van der Waals surface.
- r-distance surface (3): the surface located at a distance r from the Connolly surface.

The solid surface determined by gas porosimetry corresponds to the Connolly surface. The most used models/methods for the assessment of a solid surface are the so-called BET method (widely reported in literature [64,66]) and Density Functional Theories (DFT) [67].

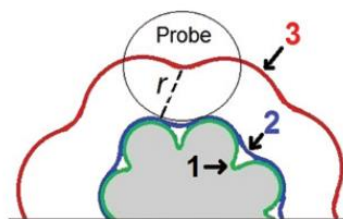


Figure 1. 17. Schematic representation of a solid surface. Taken from [64].

1.5.3. Example of porous media

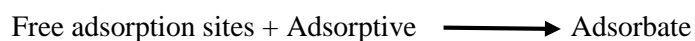
Activated carbon is one the most common porous media used in adsorption-based purification processes. It is composed of carbonic plates, which are connected by carbon-carbon bonds [68]. It is obtained through distinct stages: decomposition of substances containing a high carbon content (*e.g.* wood, coconut, bituminous coal, lignite) at high temperatures (850°C) and activation at higher temperatures (up to 1,100 °C) under an atmosphere of water vapor or carbon dioxide for instance. It presents a large specific surface area generally larger than 1,000 m² per gram which provides a high-adsorption capacity [66]. Nowadays, several types and forms of activated carbons are manufactured depending on their origins and the target application (*e.g.* air filtration, water treatment, etc.), namely beaded, granular, pelletized, extruded, powdered and cloth activated carbons.

1.5.4. Adsorption phenomena

1.5.4.1. Definitions

Sorption: is a term that embraces two phenomena, absorption and adsorption. The former denotes the penetration of a compound into the bulk material whereas the latter corresponds to the enrichment of an interface/surface with a substance [64].

Adsorption: Adsorption is a spontaneous exothermic process taking place when a gas or liquid substance, in a bulk state, gets in contact with a solid surface or two-fluid-phases interface. Indeed, these latter tend to retain ions, atoms or molecules in order to lower their high surface energy resulting from the unbalanced residual forces. Accordingly, the density (or concentration) of the surrounding substance is increased in the vicinity of the involved interface due to the prevailing molecular interactions. This phenomenon can be represented by a reaction in which the reactant is the free adsorption sites within the adsorbing material, known as adsorbent, and the compound to be adsorbed, known as adsorptive. Once adsorbed, the adsorptive is denoted “adsorbate” which occupies the so called adsorption space [64].



Adsorption is affected by the surrounding conditions mainly pressure, temperature. The higher the pressure, the higher is the adsorbed quantity, whereas the higher the temperature, the lower is the adsorbed quantity. According to the adsorbent-adsorptive prevailing interactions, we distinguish two kinds of adsorption on solids: physical and chemical adsorptions known as physisorption (van der Waals and electrostatic interactions between the adsorbent and adsorptive) and chemisorption (covalent bonds between the adsorbent and adsorptive), respectively. Hereafter, we focus only on physisorption which was employed in this thesis.

Desorption: is the reverse process of adsorption, that is a non-spontaneous endothermic phenomenon where the adsorbed amount progressively decreases under the imposed driving force. Nonetheless, it does not necessary follow the same path than the adsorption process [64].

1.5.4.2. Adsorption/Desorption mechanisms

Adsorption and desorption mechanisms are usually studied using model materials containing well-defined pores. The main mechanisms governing these two processes are reported hereafter [64,69] and illustrated in the framework of gas porosimetry for which gases such as N₂, Ar are adsorbed at cryogenic temperature and low pressure.

1.5.4.2.1. Adsorption mechanisms

Adsorption mechanisms can be defined as the way of bringing in contact the adsorptive with the adsorbent. Understanding the underlying adsorption mechanism is necessary for the analysis and the interpretation of adsorption isotherms. This allows, for example, the extraction of information about the adsorbent structural properties (pore size, specific surface, etc.). Adsorption mechanisms are mainly dictated by the adsorbent pore size and surface chemistry. Figure 1.18 depicts the main mechanisms governing adsorption process.

Micropore filling: a continuous process whereby the micropores are filled with the adsorptive molecules. It is mainly governed by enhanced gas-solid interactions. The ultramicropores filling occurs

at relative pressure (P/P_0) lower than 0.01 whereas supermicropores are filled at relative pressure between 0.01-0.2. The filling relative-pressure is dictated by several parameters namely pore shape and effective size, and both nature and size of the adsorptive molecules. The prevailing interactions during micropore filling are of solid-fluid type.

Surface coverage: it takes place on the surfaces of open mesopores or macropores at relatively high relative-pressure ($> \sim 0.2$). This mechanism occurs in two distinct stages. A monolayer adsorption stage, where all the adsorbate is in direct contact with the adsorbent surface, followed by multilayer adsorption which consists in the formation of several layers of adsorbed molecules. Accordingly, one can understand that the involved interactions are of type solid-fluid-fluid (close to the adsorbent surface) and fluid-fluid (far from the adsorbent surface).

Capillary condensation: this process follows multilayer adsorption and takes place only in mesopores. It is a phenomenon by which a gas condenses to a liquid-like phase at a pressure lower than the saturation pressure of the bulk fluid. This vapor-liquid transition is delayed as it requires nucleation (metastable state). The shift in saturation pressure is due to the influence of the attractive wall-fluid interactions (solid-fluid interactions). Capillary condensation results in the admission of relatively high amounts of adsorptive molecules.

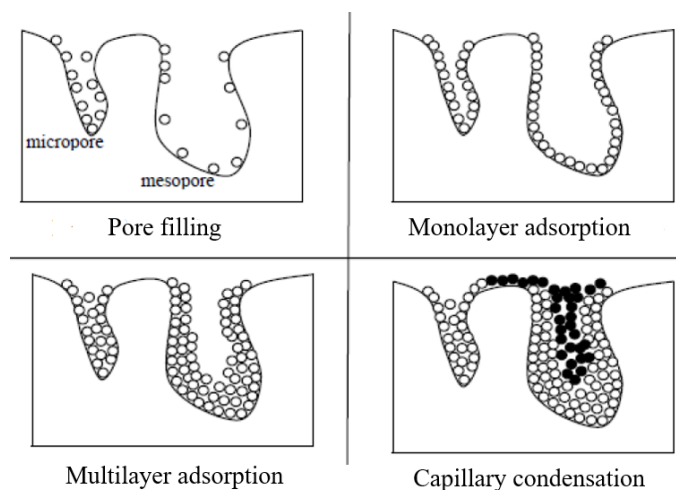


Figure 1. 18. Mechanisms of adsorption. Taken from [66].

1.5.4.2.2. Desorption mechanisms

Desorption mechanisms can be defined as the way of removing the adsorbate from the adsorbent. Desorption process also depends on the structural properties of the adsorbent. Therefore, the governing mechanisms need to be understood so that this process could be exploited for instance in porous media characterization.

Evaporation: it is the typical desorption mechanism in ordered porous media with open cylindrical pores filled with liquid-like condensate. Evaporation occurs via receding meniscus following the equilibrium liquid-vapor phase transition.

Pore blocking and cavitation: these mechanisms govern desorption process in disordered adsorbents, namely materials with ink-bottle pores. These pores present a narrow pore entrance, known as “pore neck”, leading to the so called “wide body” (see Figures 1.16 and 1.19). The pore neck width (W) dictates the desorption-governing mechanism. Indeed, in the case where its width is greater than a given critical size W_c (depending on both the adsorptive and the experimental temperature), desorption is delayed as the wide body remains filled until the neck-pore content evaporates at lower vapor pressure. This mechanism is known as “pore blocking”. For pore-neck size lower than the critical size, desorption is delayed until spontaneous nucleation of bubbles takes place in the wide body which empties while the pore neck remains filled. This mechanism is called “cavitation” (Figure 1.19). For nitrogen and argon adsorption at 77 K and 87 K, respectively, the critical size was reported between 5 and 6 nm.

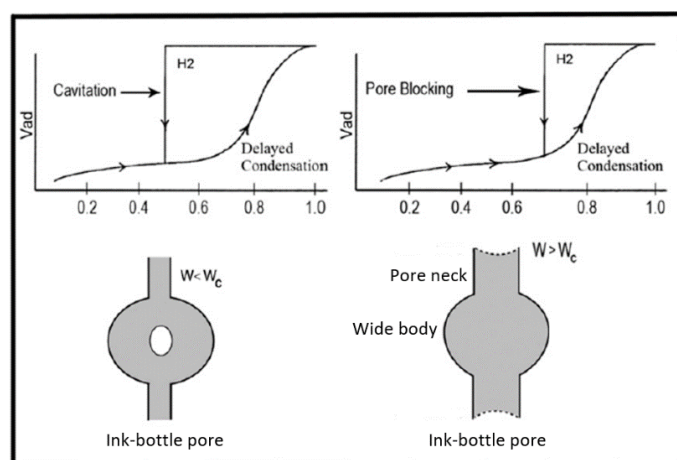


Figure 1. 19. Schematic representation of as cavitation and pore blocking mechanisms. Adapted from [69].

1.5.4.3. Surface-excess adsorbed amount

As mentioned before, adsorption results in an increase of the adsorptive density ρ in the vicinity of the adsorbent surface A compared to its bulk density (sufficiently far from the adsorbent). The adsorbate density decreases as the distance z from the adsorbent increases until reaching a bulk density ρ_b at a given thickness t (Figure 1.20). From there, the total-adsorbed amount n_{ads}^{total} can be expressed as:

$$n_{ads}^{total} = A \int_0^t \rho(z) dz \quad (\text{Eq. 1.9})$$

However, the thickness t can hardly be determined experimentally. As an alternative, Gibbs proposed a formalism which consists in replacing the adsorbent surface by an imaginary surface called Gibbs dividing surface (GDS). This latter can be determined experimentally through the use of a non-adsorbed gas (see an example of Helium (He) calibration in Appendix B-1). Therefore, it serves in expressing the adsorbed amount determined experimentally (*e.g.* manometric or gravimetric techniques (see sections 2.3.1.2 and 2.3.2.1 in Chapter 2)), known as surface-excess adsorbed amount n_{ads}^{excess} and expressed as follows:

$$n_{ads}^{excess} = A \int_0^{\infty} [\rho(z) - \rho_b] dz \quad (\text{Eq. 1.10})$$

Note that the difference between the total adsorbed amount and the surface excess amount can be neglected when the adsorptive density is very low, at very low pressures [66].

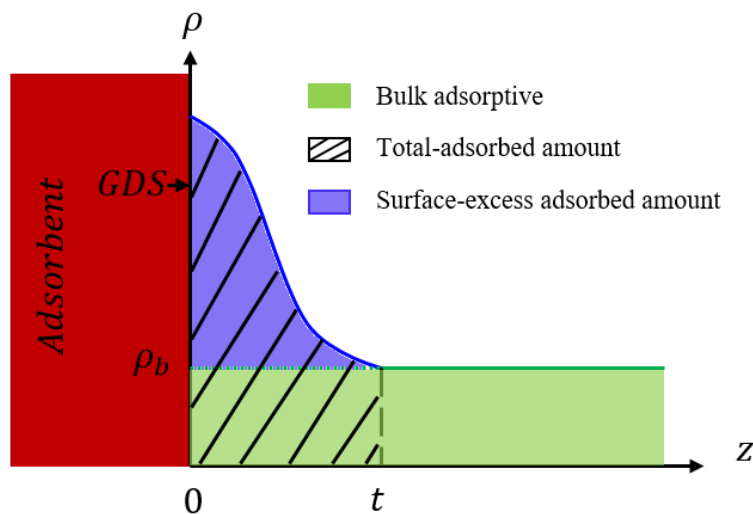


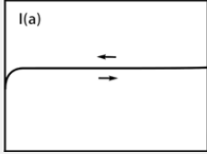
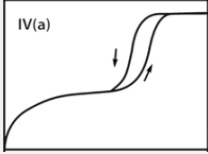
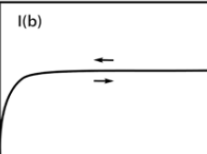
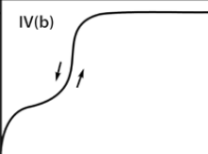
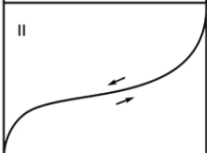

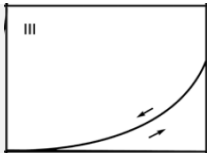

Figure 1. 20. Schematic description of surface-excess adsorbed amount. Adapted from [66].

1.5.4.4. Adsorption isotherms

Adsorption isotherms can be defined as the relation, at constant temperature, between the surface-excess adsorbed amount per unit mass of the adsorbent and the equilibrium pressures of the adsorptive. They are commonly presented as the plot of the surface-excess adsorbed mass or number of moles per gram of adsorbent against the relative pressure *i.e.* the equilibrium pressure divided by the saturation pressure of the adsorptive at the adsorption temperature. In the case where this latter is above the critical temperature of the adsorptive, namely for gases at ambient temperature, one must use the equilibrium pressure instead of the relative one since saturation pressure does not exist. Adsorption isotherms are determined point-by-point by injecting successive amounts of the adsorptive into the cell containing the adsorbent. For that purpose, manometric or gravimetric techniques can be used. As mentioned before, desorption process does not necessarily follow the same path followed by adsorption. In such case, the so-called “hysteresis” loops are generated. These latter are generally located in the multilayer range where capillary condensation takes place. Their shapes are attributed to adsorption metastability and/or network effects for ordered adsorbents and to network effects and pore blocking in the case of disordered adsorbents [64] .

Adsorption isotherms are closely related to the texture of the adsorbent. They are classified (by IUPAC) into six main types [64]. Table 1.8 reports their shapes and the main corresponding adsorbent features. Note that the x-axes correspond to the relative pressure whereas the y-axes correspond to the adsorbed amounts.

Table 1. 8. Adsorption isotherms and their corresponding adsorbent.

Isotherms	Features	Isotherms	Features
	Microporous adsorbents with mainly narrow pores (pore size < 1 nm)		Mesoporous adsorbent with pore size > critical size
	Mainly microporous adsorbents (pore size < ~2.5 nm)		Mesoporous adsorbent with pore size < critical size
	Nonporous or macroporous adsorbents		Water adsorption on hydrophobic microporous and mesoporous adsorbents
	Nonporous or macroporous (but finite adsorbed amounts at saturation)		Layer by layer adsorption on highly nonporous adsorbent

1.5.4.5. Adsorption enthalpy

The adsorption enthalpy informs on the surface state of the adsorbent and the prevailing adsorbent-adsorbate interactions. Two types of adsorption enthalpy are usually found in literature.

1.5.4.5.1. Differential enthalpy of adsorption

Differential enthalpy of adsorption $\Delta H_{T,A}$ can be defined as the heat Q_{ads} released by the infinitesimal adsorption of an excess amount n_{ads} at constant temperature T (Equation 1.11) [66].

$$\Delta H_T = \left(\frac{\partial Q_{ads}}{\partial n_{ads}} \right)_T \quad (\text{Eq. 1.11})$$

This quantity is determined experimentally by injecting small doses of the adsorptive into a cell containing the adsorbent. Therefore, it may be expressed as follows:

$$\Delta H_T \approx \left(\frac{Q_{ads}}{\Delta n_{ads}} \right)_T \quad (\text{Eq. 1.12})$$

From equation 1.12, one can understand that the measurement of the differential enthalpy of adsorption involves both manometric and calorimetric techniques for the determination of surface-excess adsorbed amount and the corresponding released thermal energy, respectively. Details on the measurement of differential enthalpy of adsorption are provided in section 2.3.2.2 Chapter 2.

1.5.4.5.2. Isosteric enthalpy of adsorption

As the differential enthalpy of adsorption varies with the quantity adsorbed, it is sometimes convenient to deal with the differential enthalpy of adsorption at constant coverage, namely the isosteric enthalpy (or heat) of adsorption. It can be calculated from a set of isotherms measured at close but different temperatures with the Clausius - Clapeyron equation by adopting the assumption that the gas phase behaves as an ideal phase and that the volume of the adsorbed phase is negligible compared to that of the gas phase.

$$\Delta H_{iso} = R \left(\frac{\partial \ln P}{\partial \left(\frac{1}{T} \right)} \right)_{n_{ads}} = -\Delta H_T + RT \quad (\text{Eq. 1.13})$$

where R is the ideal gas constant

Note that the adsorption process is supposed to be reversible and thermodynamic equilibrium is assumed to be reached when determining the adsorption isotherms. Accordingly, isosteric enthalpy should be determined only in the case of physisorption and high adsorptive pressures [66].

1.6. Hydrate formation in presence of solid materials/porous media

Several studies were conducted so as to determine the mechanisms of hydrate formation in presence of porous media mainly within the context of promoting /inhibiting hydrate formation kinetics. Various mechanisms were reported depending mainly on the nature of the involved surface.

1.6.1. Open-solid surfaces

Open-solid surfaces were found to act as heterogeneous nucleation sites. However, there is no unanimity on their impact on hydrate formation kinetics. Surface chemistry of the solid materials was suggested to be a determining factor [30]. Indeed, hydrophobic surfaces were found to present a promoting effect resulting from both the tetrahedral arrangement of water molecules they induce at their contact, and the higher gas density at the solid-water interface [30]. On the other hand, hydrophilic surfaces present an inhibiting effect due both to the distortion of water structure and low gas density at solid-water interface [30]. Govindaraj *et al.* (2015) observed a promoting effect of activated carbon suspensions on methane hydrate formation, whereas they observed an inhibiting effect of deactivated carbons at the same conditions [70]. Baek *et al.* (2015) observed that the use of small-size activated carbon particles (< 150 μm) in a tightly-packed layer configuration inhibited the formation of CP-propane mixed hydrates in the presence of non-hydrate formers (molecules of high molecular weight such as isooctane) and a surfactant [24].

1.6.2. Confining solids

The effect of confining solids on hydrate formation is more complex compared to open solid-surfaces due to the implication of several parameters, in particular the size and surface chemistry of the pores which are reported to be determinant factors [71]. Micropores (< 2 nm) likely do not provide sufficient space for hydrate nucleation [30]. In contrast, mesopores (2 to 50 nm) of activated-carbons and porous glass were found to host methane hydrate formation [72,73]. Casco *et al.* (2019) observed higher methane hydrate formation in prewetted hydrophobic mesopores than in hydrophilic ones [72]. They also showed a very high rate of methane hydrate formation in activated carbon pores [74]. Uchida *et al.* (2002) noticed a shift in the equilibrium temperatures, at a given pressure, of gas hydrates (methane, carbon dioxide and propane hydrates) confined in small pores (4 to 100 nm) of porous glass [73]. The obtained shift is inversely proportional to the pore size. For example, the equilibrium temperature of methane hydrates formed in 4 nm wide pores, at 8 MPa, showed a shift of -12.3°C , which decreased to

-0.5°C, at pressures from 2.95 to 5.72 MPa, for 100 nm wide pores. The shift towards lower equilibrium temperatures shows an inhibition effect in such pores.

1.6.3. Packed-beds

Packed-beds were also investigated in literature namely glass beds, silica particles, clays, minerals, zeolites, etc. Linga *et al.* (2009) studied methane hydrate formation in beds of silica sand particles of different sizes [33]. They found that hydrate is formed within the intra-particle spaces and the water-to-hydrate conversion, after three formation growth stages, is high (74 – 98%). They concluded that hydrate formation rate is dependent on the bed size. Siansgai *et al.* (2014) evaluated the size effect of activated-carbon particles, within a fixed bed, on methane hydrate formation. The authors reported enhanced hydrate formation for all particle sizes (from 250 to 1680 μm) [75]. The main result of their work is that hydrate growth rate is faster with small particles but water conversion, at the end of the experiments, is higher with large particles. They explained the faster growth by the higher interconnectivity spaces between the particles, and the higher water conversion by the larger interstitial spaces. The pattern of methane hydrate formation within sand silica and activated-carbon beds was investigated by Babu *et al.* (2013) [32]. Their video recordings showed hydrate fronts moving across the silica sand and smaller-sized activated carbon beds. In the silica sand bed, hydrate nucleation was observed to take place in the interstitial spaces, whereas it was produced on the surface of activated-carbon particles. Very recently, Nguyen *et al.* (2020) reported that hydrate nucleation, within beds of different-wettability mesoporous materials initially filled with water, takes place on the solid surface when this latter is hydrophobic, or at the water-gas interface in the case of a hydrophilic surface. Besides, they concluded that packed beds with mild wettability and partial saturation are optimal for hydrate formation since they allow a maximum water-gas contact [30].

1.7. Conclusion

In the literature, most of the systems involved in hydrate formation consist of packed-solid materials pre-wetted with water and in contact of gaseous compound as the hydrate former. These packed solids are generally formed with porous or non-porous particles and the authors are mainly interested in the hydrate formation within the interstitial spaces. In this thesis, we deal with porous particles of activated carbon loaded with CP as a liquid hydrate former and we are interested in hydrate formation within the pores and on the external surface of these particles (PACP). The main points that will be investigated in this work are: the role of the PACP, the effect of their characteristics (mainly SD, PSD and PV), CP-loading rate and water salinity on both hydrate formation kinetics and formed hydrate amount, and an experimental assessment of an expected thermal partial energy compensation. In order to conduct this study, various experimental techniques and setups are employed such as gas porosimetry and MIP for the PACP characterization, batch-chemical reactors for hydrate formation evaluation and calorimetry for the assessment of the prevailing energies during hydrate formation. The used techniques/setup are presented and described in the next Chapter.

1.8. References

- [1] Sloan ED, Gas Hydrates: Review of physical/chemical properties, *Energy fuels* **1998** ;12:191–6. <https://doi.org/10.1021/ef970164+>.
- [2] Sloan ED, Koh CA, Clathrate hydrates of natural gases. Third edition. CRC Press, Taylor & Francis Group, Boca Raton, **2008**.
- [3] Babu P, Nambiar A, He T, Karimi IA, Lee JD, Englezos P, A review of clathrate hydrate based desalination to strengthen energy–water nexus, *ACS Sustain Chem. Eng.*, **2018**; 6:8093–107. <https://doi.org/10.1021/acssuschemeng.8b01616>.
- [4] Zheng J, Cheng F, Li Y, Lü X, Yang M. Progress and trends in hydrate based desalination (HBD) technology: A review, *Chin. J. Chem. Eng.* **2019**; 27:2037–43. <https://doi.org/10.1016/j.cjche.2019.02.017>.
- [5] Sangwai J.S., Patel R.S., Mekala P., Mech D, Busch M. desalination of seawater using gas hydrate technology – current status and future direction. *Water Resour.* **2013**.
- [6] Touil A, Étude par microscopie optique de la nucléation, croissance et dissociation des hydrates de gaz. These de doctorat. Pau, **2018**.
- [7] Tohidi B, Burgass RW, Danesh A, Østergaard KK, Todd AC. Improving the accuracy of gas hydrate dissociation point measurements. *Ann N Y Acad Sci* **2000**; 912:924–31. <https://doi.org/10.1111/j.1749-6632.2000.tb06846.x>.
- [8] Ho-Van S, Bouillot B, Douzet J, Babakhani SM, Herri JM. Experimental measurement and thermodynamic modeling of cyclopentane hydrates with NaCl, KCl, CaCl₂, or NaCl-KCl present. *AIChE J* **2018**; 64:2207–18. <https://doi.org/10.1002/aic.16067>.
- [9] Vysniauskas A, and Bishnoi P, A kinetic study of methane hydrate formation. *Chemical Engineering Science*; **1983**.
- [10] Arjmandi M, Tohidi B, Danesh A, Todd AC, Is subcooling the right driving force for testing low-dosage hydrate inhibitors?, *Chem. Eng. Sci.*, **2005**; 60:1313–21. <https://doi.org/10.1016/j.ces.2004.10.005>.
- [11] Martinez ML, Mechanisms of formation and dissociation of cyclopentane hydrates. These de doctorat. Pau, **2015**.
- [12] Dirksen JA, Ring TA. Fundamentals of crystallization: Kinetic effects on particle size distributions and morphology. *Chem. Eng. Sci.*, **1991**; 46:2389–427. [https://doi.org/10.1016/0009-2509\(91\)80035-W](https://doi.org/10.1016/0009-2509(91)80035-W).

- [13] Khurana M, Yin Z, Linga P, A review of Clathrate Hydrate Nucleation, *ACS Sustain. Chem. Eng.* **2017**; 5:11176–203. <https://doi.org/10.1021/acssuschemeng.7b03238>.
- [14] Elwell D and Scheel HJ, *Crystal growth from high-temperature solutions*, Acad Press Lond **1975**.
- [15] Ho-Van S, Bouillot B, Douzet J, Babakhani SM, Herri JM. Cyclopentane hydrates – A candidate for desalination?, *J. Environ. Chem. Eng.* **2019**; 7:103359. <https://doi.org/10.1016/j.jece.2019.103359>.
- [16] Cai L, Pethica BA, Debenedetti PG, Sundaresan S. Formation of cyclopentane methane binary clathrate hydrate in brine solutions. *Chem Eng Sci* **2016**; 141:125–32. <https://doi.org/10.1016/j.ces.2015.11.001>.
- [17] Kishimoto M, Iijima S, Ohmura R. Crystal Growth of Clathrate Hydrate at the Interface between Seawater and Hydrophobic-Guest Liquid: Effect of Elevated Salt Concentration. *Ind. Eng. Chem. Res.* **2012**; 51:5224–9. <https://doi.org/10.1021/ie202785z>.
- [18] Lee W, Baek S, Kim J-D, Lee JW. Effects of salt on the crystal growth and adhesion force of clathrate hydrates, *Energy Fuels* **2015**; 29:4245–54. <https://doi.org/10.1021/acs.energyfuels.5b00768>.
- [19] Fakharian H, Ganji H, Naderifar A, Desalination of high salinity produced water using natural gas hydrate. *J. Taiwan Inst. Chem. Eng.* **2017**; 72:157–62. <https://doi.org/10.1016/j.jtice.2017.01.025>.
- [20] Han S, Rhee YW, Kang SP, Investigation of salt removal using cyclopentane hydrate formation and washing treatment for seawater desalination. *Desalination* **2017**; 404:132–7. <https://doi.org/10.1016/j.desal.2016.11.016>.
- [21] Delroisse H, Torré JP, Dicharry C, Effect of a hydrophilic cationic surfactant on cyclopentane hydrate crystal growth at the water/cyclopentane interface, *Cryst. Growth Des.* **2017**; 17:5098–107. <https://doi.org/10.1021/acs.cgd.7b00241>.
- [22] Atig D, Broseta D, Pereira JM, Brown R, Contactless probing of polycrystalline methane hydrate at pore scale suggests weaker tensile properties than thought. *Nat. Commun.* **2020**; 11:3379. <https://doi.org/10.1038/s41467-020-16628-4>.
- [23] Qanbari F, Pooladi-Darvish M, Hamed Tabatabaie S, Gerami S, Storage of CO₂ as hydrate beneath the ocean floor. *Energy Procedia* **2011**; 4:3997–4004. <https://doi.org/10.1016/j.egypro.2011.02.340>.
- [24] Baek S, Min J, Lee JW, Inhibition effects of activated carbon particles on gas hydrate formation at oil-water interfaces, *RSC Adv.* **2015**; 5:58813–20. <https://doi.org/10.1039/c5ra08335d>.
- [25] Liu W, Li X, Hu J, Wu K, Sun F, Sun Z, Research on flow assurance of deepwater submarine natural gas pipelines: hydrate prediction and prevention, *J. Loss Prev. Process Ind.* **2019**; 61:130–46. <https://doi.org/10.1016/j.jlp.2019.06.007>.

- [26] Olajire AA, Flow assurance issues in deep-water gas well testing and mitigation strategies with respect to gas hydrates deposition in flowlines: a review, *J. Mol. Liq.* **2020**; 318:114203. <https://doi.org/10.1016/j.molliq.2020.114203>.
- [27] Cha J-H, Seol Y. Increasing Gas Hydrate Formation Temperature for Desalination of High Salinity Produced Water with Secondary Guests. *ACS Sustain Chem. Eng.* **2013**; 1:1218–24. <https://doi.org/10.1021/sc400160u>.
- [28] Dawe RA, S. Thomas, M. Kromah, Hydrate technology for transporting natural gas. *Eng. J. of Univ. of Qatar* 16 **2003**; 11–18
- [29] Torré JP, Dicharry C, Ricaurte M, Daniel-David D, Broseta D, CO₂ capture by hydrate formation in quiescent conditions: in search of efficient kinetic additives, *Energy Procedia* **2011**; 4:621–8. <https://doi.org/10.1016/j.egypro.2011.01.097>.
- [30] Nguyen NN, Galib M, Nguyen AV, Critical Review on Gas Hydrate Formation at Solid Surfaces and in Confined Spaces—Why and How Does Interfacial Regime Matter?, *Energy Fuels* **2020**; 34:6751–60. <https://doi.org/10.1021/acs.energyfuels.0c01291>.
- [31] Linga P, Clarke MA. A Review of Reactor Designs and Materials Employed for Increasing the Rate of Gas Hydrate Formation. *Energy Fuels* **2017**; 31:1–13. <https://doi.org/10.1021/acs.energyfuels.6b02304>.
- [32] Babu P, Yee D, Linga P, Palmer A, Khoo BC, Tan TS, Morphology of methane hydrate formation in porous media. *Energy Fuels* **2013**; 27:3364–72. <https://doi.org/10.1021/ef4004818>.
- [33] Linga P, Haligva C, Nam SC, Ripmeester JA, Englezos P, Gas Hydrate formation in a Variable Volume Bed of Silica Sand Particles. *Energy Fuels* **2009**; 23:5496–507. <https://doi.org/10.1021/ef900542m>.
- [34] Li F, Chen Z, Dong H, Shi C, Wang B, Yang L, Promotion effect of graphite on cyclopentane hydrate based desalination. *Desalination* **2018**; 445:197–203. <https://doi.org/10.1016/j.desal.2018.08.011>.
- [35] Mallek R, Miqueu C, Jacob M, Le Mélinaire P, Dicharry C, Effect of porous activated carbon particles soaked in cyclopentane on CP-hydrate formation in synthetic produced water, *J. Water Process Eng.* **2020**; 38:101660. <https://doi.org/10.1016/j.jwpe.2020.101660>.
- [36] Zylyftari G, Lee JW, Morris JF, Salt effects on thermodynamic and rheological properties of hydrate forming emulsions. *Chem. Eng. Sci.* **2013**;95:148–60. <https://doi.org/10.1016/j.ces.2013.02.056>.
- [37] Babu P, Nambiar A, Chong ZR, Daraboina N, Albeirutty M, Bamaga OA, Hydrate-based desalination (HyDesal) process employing a novel prototype design, *Chem. Eng. Sci.* **2020**; 218:115563. <https://doi.org/10.1016/j.ces.2020.115563>.

- [38] He T, Nair SK, Babu P, Linga P, Karimi IA, A novel conceptual design of hydrate based desalination (HyDesal) process by utilizing LNG cold energy, *Applied Energy* **2018**; 222:13–24. <https://doi.org/10.1016/j.apenergy.2018.04.006>.
- [39] Chong ZR, He T, Babu P, Zheng J, Linga P, Economic evaluation of energy efficient hydrate based desalination utilizing cold energy from liquefied natural gas (LNG), *Desalination* **2019**; 463:69–80. <https://doi.org/10.1016/j.desal.2019.04.015>.
- [40] Montazeri V, Rahimi M, Zarenezhad B. Energy saving in carbon dioxide hydrate formation process using Boehmite nanoparticles. *Korean J. Chem. Eng.* **2019**; 36:1859–68. <https://doi.org/10.1007/s11814-019-0375-y>.
- [41] Lee SH, Park K, Conceptual design and economic analysis of a novel cogeneration desalination process using LNG based on clathrate hydrate. *Desalination* **2021**; 498 <https://doi.org/10.1016/j.desal.2020.114703>.
- [42] Li X, Negadi L, Firoozabadi A, Anti-agglomeration in cyclopentane hydrates from bio- and co-surfactants. *Energy Fuels* **2010**; 24:4937–43. <https://doi.org/10.1021/ef100622p>.
- [43] Park K, Hong SY, Lee JW, Kang KC, Lee YC, Ha M-G, A new apparatus for seawater desalination by gas hydrate process and removal characteristics of dissolved minerals (Na⁺, Mg²⁺, Ca²⁺, K⁺, B³⁺). *Desalination* **2011**; 274:91–6. <https://doi.org/10.1016/j.desal.2011.01.084>.
- [44] Sefidroodi H, Abrahamsen E, Kelland MA, Investigation into the strength and source of the memory effect for cyclopentane hydrate. *Chem. Eng. Sci.* **2013**; 87:133–40. <https://doi.org/10.1016/j.ces.2012.10.018>.
- [45] Delroisse H, Plantier F, Marlin L, Dicharry C, Frouté L, André R, et al. Determination of thermophysical properties of cyclopentane hydrate using a stirred calorimetric cell. *J Chem Thermodyn* **2018**; 125:136–41. <https://doi.org/10.1016/j.jct.2018.05.023>.
- [46] Zhang Y, Debenedetti PG, Prud'homme RK, Pethica BA, Differential scanning calorimetry studies of clathrate hydrate formation, *J. Phys. Chem. B.* **2004**; 108:16717–22. <https://doi.org/10.1021/jp047421d>.
- [47] Nakajima M, Ohmura R, Mori YH, Clathrate hydrate formation from Cyclopentane-in-Water emulsions. *Ind Eng. Chem. Res.* **2008**; 47:8933–9. <https://doi.org/10.1021/ie800949k>.
- [48] Çakmakce M, Kayaalp N, Koyuncu I, Desalination of produced water from oil production fields by membrane processes. *Desalination* **2008**; 222:176–86. <https://doi.org/10.1016/j.desal.2007.01.147>.
- [49] Al-Ghouti MA, Al-Kaabi MA, Ashfaq MY, Da'na DA, Produced water characteristics, treatment and reuse: a review, *J. Water Process Eng.* **2019**; 28:222–39. <https://doi.org/10.1016/j.jwpe.2019.02.001>.

- [50] Benko KL, Drewes JE. Produced water in the western united states: geographical distribution, occurrence, and composition, *Environ. Eng. Sci.* **2008**; 25:239–46. <https://doi.org/10.1089/ees.2007.0026>.
- [51] Khatib Z, Verbeek P, Water to value - Produced water management for sustainable field development of mature and green fields, *JPT J Pet Technol* **2003**; 55:26–8. <https://doi.org/10.2118/0103-0026-JPT>.
- [52] Abousnina R. an overview on oil contaminated sand and its engineering applications, *Int J geomate* **2015**; 10:1615–22. <https://doi.org/10.21660/2016.19.150602>.
- [53] Nair RR, Protasova E, Strand S, Bilstad T, Membrane performance analysis for smart water production for Enhanced oil recovery in carbonate and sandstone reservoirs, *Energy Fuels* **2018**; 32:4988–95. <https://doi.org/10.1021/acs.energyfuels.8b00447>.
- [54] Islam MS, Sultana A, Saadat AHM, Islam MS, Shammi M, Uddin MK. Desalination Technologies for Developing Countries: a review. *J Sci Res* **2018**; 10:77–97. <https://doi.org/10.3329/jsr.v10i1.33179>.
- [55] Galama O, Ion exchange membranes in seawater applications processes and characteristics. **2015**; ISBN 978-94-6257-225-6
- [56] Ghalavand Y, Hatamipour MS, Rahimi A, A review on energy consumption of desalination processes, *Desalination Water Treat.***2014**; 1-16. <https://doi.org/10.1080/19443994.2014.892837>.
- [57] Younos T, Tulou KE, Overview of desalination techniques: overview of techniques, *J. Contemp. Water Res. Educ.* **2009**; 132:3–10. <https://doi.org/10.1111/j.1936-704X.2005.mp132001002.x>.
- [58] El-Dessouky HT, Ettouney HM, Fundamentals of salt water desalination, Elsevier Science: Amsterdam, The Netherlands, **2002**.
- [59] Millero FJ, Feistel R, Wright DG, McDougall TJ. The composition of standard seawater and the definition of the reference-composition salinity scale. *Deep-Sea Res. Part Oceanogr. Res. Pap.* **2008**; 55:50–72. <https://doi.org/10.1016/j.dsr.2007.10.001>.
- [60] Han S, Shin JY, Rhee YW, Kang SP, Enhanced efficiency of salt removal from brine for cyclopentane hydrates by washing, centrifuging, and sweating. *Desalination* **2014**; 354:17–22. <https://doi.org/10.1016/j.desal.2014.09.023>.
- [61] R. Lacey, G. Walker. Decontamination in Hospitals and Healthcare, pages 651-678, **2014**; ISBN 978-0-85709-657-9
- [62] Mottet B, Method for crystallising clathrate hydrates, and method for purifying an aqueous liquid using the clathrate hydrates thus crystallised, Applicant: BGH[FR]. EP3153606,

<https://worldwide.espacenet.com/patent/search/family/054476876/publication/WO2017060456A1?q=PCT%2FEP2016%2F074044>.

- [63] Satken B, Adsorption/retention of polymer solution in porous media, phd thesis. Université de Bordeaux, **2021**.
- [64] Thommes M, Kaneko K, Neimark AV, Olivier JP, Rodriguez-Reinoso F, Rouquerol J, et al., Physisorption of gases, with special reference to the evaluation of surface area and pore size distribution (IUPAC Technical Report). *Pure Appl. Chem.* **2015**; 87:1051–69. <https://doi.org/10.1515/pac-2014-1117>.
- [65] Qi L, Tang X, Wang Z, Peng X, Pore characterization of different types of coal from coal and gas outburst disaster sites using low temperature nitrogen adsorption approach, *Int J Min Sci Technol* **2017**; 27:371–7. <https://doi.org/10.1016/j.ijmst.2017.01.005>.
- [66] Mouahid A, Mise au point point d'un dispositif couple manométrique calorimétrique pour l'étude de l'adsorption de fluides supercritiques dans des milieux microporeux et mesoporeux. Physique[physics]. Université de Pau et des Pays de l'Adour., **2010**. Français. NNT: 10PAUU3020. tel-00573997. n.d.
- [67] Landers J, Gor GYu, Neimark AV, Density functional theory methods for characterization of porous materials. *Colloids Surf. Physicochem Eng. Asp.* **2013**; 437:3–32. <https://doi.org/10.1016/j.colsurfa.2013.01.007>.
- [68] Corporation CC, activated carbon, Calgon carbon corpo., <https://www.calgoncarbon.com>.
- [69] Thommes M, Cychosz K, Neimark A, Advanced Physical Adsorption Characterization of Nanoporous Carbons. *Nov. Carbon Adsorbents*, **2012**, p. 107–45. <https://doi.org/10.1016/B978-0-08-097744-7.00004-1>.
- [70] Govindaraj V, Mech D, Pandey G, Nagarajan R, Sangwai JS, Kinetics of methane hydrate formation in the presence of activated carbon and nano-silica suspensions in pure water. *J. Nat. Gas Sci. Eng.*, **2015**; 26:810–8. <https://doi.org/10.1016/j.jngse.2015.07.011>.
- [71] Pasięka J, Coulombe S, Servio P. The effect of hydrophilic and hydrophobic multi-wall carbon nanotubes on methane dissolution rates in water at three phase equilibrium (V–Lw–H) conditions, *Ind. Eng. Chem. Res.* **2014**; 53:14519–25. <https://doi.org/10.1021/ie502457c>.
- [72] Casco ME, Zhang E, Grätz S, Krause S, Bon V, Wallacher D, Experimental Evidence of confined methane hydrate in hydrophilic and hydrophobic model carbons, *J. Phys. Chem. C.* **2019**; 123:24071–9. <https://doi.org/10.1021/acs.jpcc.9b06366>.
- [73] Uchida T, Ebinuma T, Takeya S, Nagao J, Narita H, Effects of pore sizes on dissociation temperatures and pressures of methane, carbon dioxide, and propane hydrates in porous media, *J. Phys. Chem. B.* **2002**; 106:820–6. <https://doi.org/10.1021/jp012823w>.

- [74] Casco ME, Silvestre-Albero J, Ramírez-Cuesta AJ, Rey F, Jordá JL, Bansode A, Methane hydrate formation in confined nanospace can surpass nature, *Nat. Commun.* **2015**; 6. <https://doi.org/10.1038/ncomms7432>.
- [75] Siangsai A, Rangsunvigit P, Kitiyanan B, Kulprathipanja S, Linga P, Investigation on the roles of activated carbon particle sizes on methane hydrate formation and dissociation, *Chem. Eng. Sci.* **2015**; 126:383–9. <https://doi.org/10.1016/j.ces.2014.12.047>.

Chapter 2. Experimental techniques and setups

2.1. Introduction

As mentioned in the general introduction, the vocation of this thesis is the investigation of hydrate formation from CP-loaded PACP immersed in water so that to understand the prevailing mechanisms. For that purpose, several experimental techniques and setups were used/combined. In this chapter, we present the used materials and describe the employed experimental techniques/setups.

2.2. Materials

CP (purity of 97%) was purchased from Sigma Aldrich. Its density, measured in our laboratory ($0.7437 \pm 0.0001 \text{ g/cm}^3$ at 20°C) is in perfect agreement with published values [1]. Deionized water (resistivity of $18.2 \text{ M}\Omega\cdot\text{cm}$) was produced by a Purelab® laboratory water-purification system. Sodium chloride NaCl (purity of 99.5%) was supplied by Acros Organics. PACP, of different PSD and/or SD were used (Table 2.1).

Table 2. 1. *The different PACP used in this work.*

PACP	Given name	Form	Particle size (μm)	Origin	Supplier
G-BAC-G70R	Gbac	Beaded	700	Petroleum pitch	Keruha GmbH
A-BAC-SP	Abac	Beaded	400	Petroleum pitch	Keruha GmbH
Chem-A	ChemA	Powder	<177	Coconut	Chemviron SA
Cyclecarb 401	Cycarb	Granular	1000	Bitumine coal	Chemviron SA
Cyclecarb 401	Cycarb	Powder	<177	Bitumine coal	Chemviron SA
BGX	BGX	Granular	1000	Wood	Chemviron SA

The samples were weighed with a ALC-110.4 balance (from Accurlab®) with an uncertainty of 10^{-4} g. A vacuum preparation apparatus, called VacPrep™ (from Micromeritics) was used to purify the PACP samples at 200 °C, under primary vacuum (120 mtorr). A density meter DMA 4100 M (from Anton-Paar®) was used for measuring the density of CP with an uncertainty of 10^{-4} g/cm³. A set of glass flasks with a 30-mL capacity, and two Julabo F32™ cryostats, using ethane-diol as a refrigerant, were used to determine the CP-hydrate equilibrium temperatures as a function of NaCl concentration. The refractive index of the unconverted water (residual water after hydrate formation) was measured, at a wavelength of 589.3 nm and a temperature of 20°C, using two refractometers (from Anton Paar®): Abbemat 3200™ (uncertainty of 10^{-4}) and Abbemat 550™ (uncertainty of 10^{-5}) in Chapters 3 and 6, respectively. Plastic syringes of 3-mL capacity and cellulose acetate syringe filters of 0.8- μ m mesh size were purchased from Sodipro® in order to take and filter samples of the aqueous solution. Adsorption capacities of the PACP at 1°C were determined using a closed vessel, partially filled with CP, here referred to as CP-adsorption chamber, and a set of closable-flasks with a 5-mL capacity. The closed vessel was inserted into a universal convection incubator (from Memmert®).

2.3. Description of experimental techniques and setups

The experimental techniques/setups used in this work are classified depending on the investigated systems: virgin PACP, PACP loaded with CP and PACP loaded with CP immersed in water.

2.3.1. Characterization of virgin PACP

The virgin PACP were characterized first by using laser diffraction to determine their particle size distribution (SD). Gas porosimetry (with Argon at 87 K (-186.15 °C)) was used to obtain the pore size distribution (PSD) and pore volumes (PV) of the micro- and small mesopores (size < 30 nm) together with specific surface area (SSA) of the PACP. The pore volumes of the largest pores were determined by mercury intrusion porosimetry (MIP).

2.3.1.1. Laser diffraction

The SD of PACP was determined using a Mastersizer 2000 particle size analyzer from Malvern Instruments Ltd (Figure 2.1) where the collected raw data were interpreted with Mastersizer 2000 v5.61 software. Laser diffraction, also called static light scattering, relies on angular dependence of the scattered intensity. It is the most frequent technique used for particle size determination. The particles are dispersed and routed through a dispersion unit (here Hydro 2000) towards the optical bench where they are exposed to a laser beam. Detectors record the resulting diffraction pattern (Figure 2.2) which is then interpreted using Mie scattering theory while assuming spherical particles and elastic scattering. Hence, the particle granulometry (or SD) is provided [2,3].



Figure 2. 1. Mastersizer 2000 apparatus. (1) Hydro 2000; (2) Optical bench

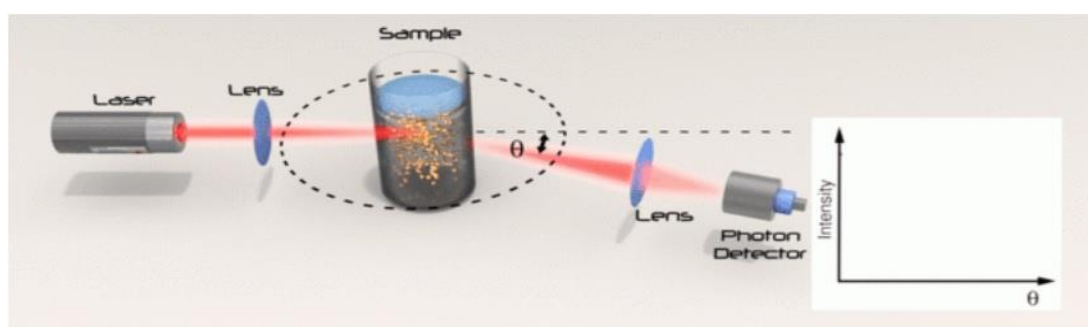


Figure 2. 2. Principle of laser diffraction technique. Taken from [4].

2.3.1.2. Gas porosimetry

The PSD, PV and SSD of the PACP were evaluated with gas porosimetry using an Autosorb IQ gas sorption analyzer from Quantachrome Instruments (Figure 2.3). The raw data were interpreted with

ASiQwin v5.0 software. Gas porosimetry is a technique used for the characterization of porous materials through adsorption phenomenon, in particular physisorption for textural characteristics determination (PSD, PV, SSA, etc.). This technique is based on the generation and interpretation of isotherms (adsorption, desorption or both) of a probe molecule (most frequently N₂, Ar or CO₂) on the porous medium, at an appropriate temperature (77, (77 or 87), 273 K, respectively). The choice of both the probe molecule and the isotherm temperature is chosen according to the analyzed porous material. Indeed, argon at 87 K is more adapted for microporous materials since argon does not present a quadrupole moment and at this temperature, its cross-sectional area is less sensitive to the differences in the structure of the adsorbent surface. Besides, at 87 K, argon fills the micropores at relative pressures about 100 times higher than nitrogen. Because diffusion in the micropores is faster under these conditions, equilibrium times are shorter and high-resolution isotherm measurements are more readily available than with nitrogen at 77 K [5]. In order to measure the isotherms, the sample is first outgassed under secondary vacuum, at 200°C during 12 hrs. The dead space (void volume) of both the cell and the circuit is calibrated with helium. Afterwards, the adsorptive (probe molecules) is introduced into a dosing volume (an enclosure of known volume) at a given pressure, then injected into the measurement cell so that to be adsorbed by the sample (adsorbent). The equilibrium pressure within the cell is measured and surface-excess adsorbed amount (defined in section 1.5.4.3 Chapter 1) is determined as classically done for adsorption measurements with such a manometric technique [6] (Figure 2.4). The process is repeated until the isotherm points are obtained. The isotherm is interpreted using adapted theoretical models so that the porous medium characteristics are obtained. One of the reliable used models is the so-called Quenched Solid Density Functional Theory (QSDFT) [7]. Indeed, it is a recent developed version of non-local density functional theory which considers the heterogeneity of the solid surface by introducing a roughness parameter. A set of theoretical isotherms of a given probe molecule within a pore of a given nature, geometry, at the analysis temperature and for the whole pressure range, known as kernel, is generated with QSDFT for a given series of pore sizes. This latter is correlated with the experimental isotherm through the integral adsorption equation, also called generalized adsorbed equation (equation 2.1). The resolution of this equation results in the PSD $f(D)$ of the analyzed porous medium (Figure 2.5).

$$N_{\text{exp}}(P/P_0) = \int_{D_{\text{min}}}^{D_{\text{max}}} N_{QSDFT}(P/P_0, D) f(D) dD \quad (\text{Eq. 2.1})$$

where $N_{\text{exp}}(P/P_0)$ and N_{QSDFT} are the experimental isotherm and the kernel, respectively. D_{max} and D_{min} are respectively the maximum and minimum pore diameters in the kernel for a given pore diameter D .

It should be noted that the theoretical investigated porosity lays between 0.5 nm and 50 nm, whereas in practice the kernel are given for pore sizes in the range of 0.5 - 30 nm [8].

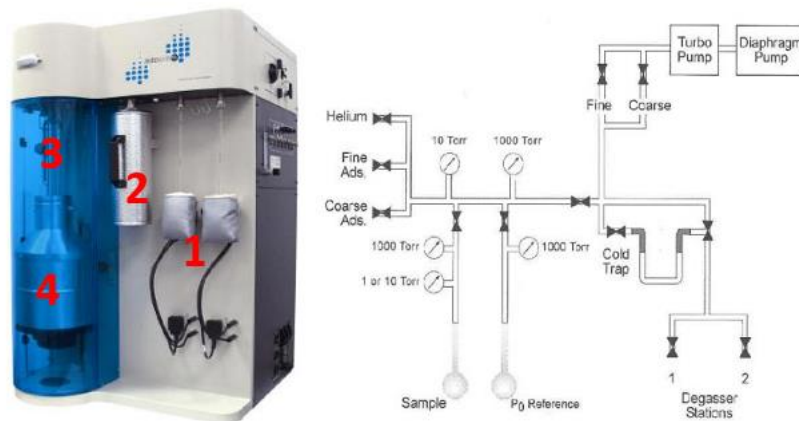


Figure 2. 3. Autosorb Quantachrome IQ instrument.

- (1) Outgas stations: used for sample purification. (2) Cold trap Dewar flask: it traps the sample impurities left from outgassing. (3) Analysis stations: used for analyzing the sample. (4) Analysis Dewar: filled with liquid nitrogen so that to cool down the cell.

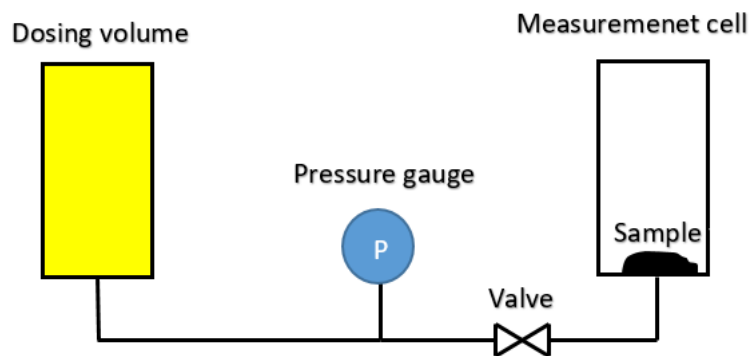


Figure 2. 4. Basic schematic of manometric technique. Adapted from [9].

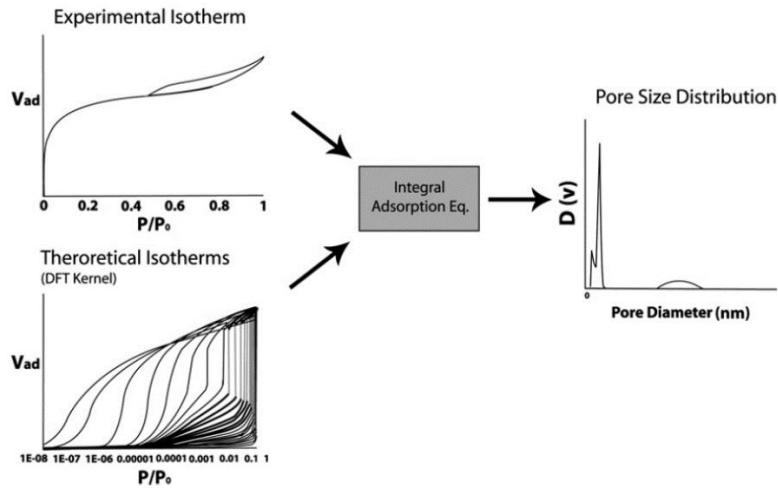


Figure 2. 5. Schematic representation of the procedure used in calculating a DFT pore-size distribution from experimental adsorption/desorption isotherms. Taken from [7].

2.3.1.3. Mercury intrusion porosimetry

The PSD developed towards meso and macroporous regions and the meso-macro PV of PACP were assessed with MIP using Autopore IV 9500 mercury intrusion porosimeter from Micromeritics® (Figure 2.6) where the raw data were interpreted with MicroActive v2.03.00 software.

MIP is a characterization technique based on the suggestion of Washburn (1921) which is how pressure-volume data from mercury (a non-wetting compound towards most substances) penetration into a porous medium could result in its fingerprint determination [10]. Indeed, a mercury intrusion curve is generated and interpreted so that to obtain the material characteristics. The sample to be analyzed is sealed into a glass vessel tapered into a capillary tube known as a penetrometer. The capillary tube, made of glass (insulator) and filled with mercury (conductor) is covered with a metal (conductor) so that it acts as a coaxial capacitor. Therefore, the mercury volume leaving, under pressurization steps, is determined since it is proportional to the measured capacitance. Hence, intrusion curve is obtained and the PSD is determined by converting the intrusion pressure into pore radius using Washburn law:

$$D_i = \frac{-4\delta \cos\theta}{P_i} \quad (\text{Eq. 2.2})$$

where D_i is the pore diameter, δ is the surface tension of mercury, θ is the material wettability and P_i is the intrusion pressure.

For further structural/textural investigations, mercury extrusion and pressurization/depressurization cycles are performed. Indeed, porous materials with an ink-bottle pore morphology, for instance some cementitious materials, require such analysis so that to overcome the so called the ink-bottle effect [11]. MIP allows investigation of a porosity theoretically ranging between 3 nm and 1.1 mm and practically from approx. 10 nm to 300 μm [12].

Note that MIP technique presents several limitations. Indeed, there are some assumptions behind the use of Washburn law such as assuming an arrangement from large pores to narrow ones. Besides, very high pressures may lead to sample degradation and both mercury and porous material compressibility should be corrected. Moreover, the measurement of mercury surface tension and contact angle within the pores as pressure increases/decreases cannot be done and is thus generally adjusted through the combination with other techniques. As an example, the Mayer-Stowe method can be used to determine the size distribution of spherical particles from the intrusion data in the range of interstitial filling, and the contact angle can be fitted so that this distribution is consistent with the one obtained by laser diffraction.



Figure 2. 6. Autopore IV 9500 instrument. a) low pressure port; b) high pressure port.

2.3.2. Analysis of CP adsorption-desorption on/from the PACP

Loading and unloading of CP in/from the PACP were investigated. Indeed, adsorption/desorption isotherms, adsorption differential enthalpy and post-desorption characterization of PACP were respectively obtained through gravimetry of adsorption, calo-manometric technique and both gas porosimetry and thermogravimetric analysis. From there, the CP-adsorption/desorption capacities of the PACP were determined, the CP-PACP interactions described and the effect of SD, PSD, temperature and CP-loading method on adsorption and/or desorption capacities investigated.

2.3.2.1. Gravimetric technique

Adsorption and desorption isotherms of CP on/from PACP were measured by gravimetric technique using a magnetic suspension balance from Rubotherm® GmbH connected to a homemade steam generator (CP-tank partially filled with CP so that vapor CP is generated) (Figures 2.7 and 2.9). The raw data were recorded through an acquisition unit together with MessPro software. From there, the adsorbed/desorbed excess masses calculated [13].

Gravimetry is a technique used for the measurement of equilibrium and/or kinetics sorption of gases and vapors on porous materials. Therefore, adsorption/desorption capacities and rates can be determined. For that purpose, very sensitive balances (10^{-5} g up to 10^{-6} g), denoted as microbalances, are used to measure the excess adsorbed amounts namely spring balances, piezoelectric balances and magnetic suspension balances (MSB) [14].

MSB monitors the mass of a sample (adsorbent) in contact with gas or vapor (adsorptive). The “measurement system (MS)” consists of a crucible that hosts the sample to be analyzed coupled, through a coupling system, with both a cylinder (used for determining the density of the surrounding gas/vapor) and a stem rigidly connected with a permanent magnet. The MS is located within the adsorption chamber where it is exposed to the gas/vapor to be adsorbed. The adsorption chamber is thermally regulated by means of a double envelope in which silicone oil circulates at a temperature imposed by a thermostatic bath. The position of the permanent magnet is detected and controlled through a regulation system

consisting of two solenoids and a magnet bar. An electromagnet, placed outside the adsorption chamber and supplied with the induced current of the regulation system, maintains the MS in suspension. The measurement principle of the MSB is based on the mechanical equilibrium of the forces acting on the MS: the magnetic force (M) generated between the electromagnet and the permanent magnet, the weight (W) of the MS and the buoyancy (B) induced by the surrounding gas/vapor within the adsorption chamber (Equation 2.3). Indeed, the magnetic force balances both the weight and the buoyancy forces so that the permanent magnet is maintained at a constant position.

$$\vec{M} + \vec{B} + \vec{W} = \vec{0} \quad (\text{Eq. 2.3})$$

Projecting vertically the previous relation leads to:

$$M + \rho_{gas/vapor} V_{MS} g - m_{MS} g = 0 \quad (\text{Eq. 2.4})$$

where $\rho_{gas/vapor}$, V_{MS} , m_{MS} and g are the gas or vapor density, the volume of the “measurement system”, the mass of the “measurement system” and the gravitational acceleration, respectively.

Equation 2.4 can be rearranged as follows:

$$\frac{M}{g} + \rho_{gas/vapor} V_{MS} - m_{MS} = 0 \quad (\text{Eq. 2.5})$$

The quantity $\frac{M}{g}$, homogenous to a mass, presents the signal delivered by the MSB. This latter allows three distinct measurements, denoted as ZP, MP1, MP2, depending on the “measurement system” in suspension (Figure 2.8). By applying equation 2.5 to each position, the expression of the three measurement positions is obtained.

ZP (Zero Point): the stem (St) connected to the permanent magnet is in suspension

$$ZP = m_{St} - \rho_{gas/vapor} V_{St} \quad (\text{Eq. 2.6})$$

MP1 (Measuring Point 1): the stem connected to the permanent magnet + the crucible (Cr) are in suspension

$$MP1 = m_{St} + m_{Cr} - \rho_{gas/vapor} (V_{St} + V_{Cr}) \quad (\text{Eq. 2.7})$$

MP2 (Measuring point 2): the stem connected to the permanent magnet + the crucible + the cylinder (Cy) are in suspension.

$$MP2 = m_{St} + m_{Cr} + m_{Cy} - \rho_{gas/vapor} (V_{St} + V_{Cr} + V_{Cy}) \quad (\text{Eq. 2.8})$$

The expression of the adsorbed amount ($m_{adsorbate}$) (equation 2.9) is obtained by introducing the masses and volumes of the sample to be analyzed ($m_{absorbent}$ and $V_{adsorbent}$) and the adsorbed gas/vapor ($m_{adsorbate}$ and $V_{adsorbate}$) into equation (2.7) and combining it with equation 2.6.

$$m_{adsorbate} = (MP1 - ZP) - (m_{Cr} + m_{absorbent}) + \rho_{gas/vapor} (V_{Cr} + V_{adsorbent} + V_{adsorbate}) \quad (\text{Eq. 2.9})$$

While MP1 and ZP are directly measured with the MSB, the terms $m_{absorbent}$, $V_{adsorbent}$, m_{Cr} , V_{Cr} and $V_{adsorbate}$ must be previously calibrated so as to determine the adsorbed amount (see Appendix B-1). The volume of the adsorbed amount $V_{adsorbate}$ cannot be provided experimentally, thus only a quantity known as surface-excess adsorbed amount (m_{excess}) (see section 1.5.4.3 in chapter 1) can be evaluated (Equation 2.10):

$$\begin{aligned} m_{excess} &= m_{adsorbate} - \rho_{gas/vapor} V_{adsorbate} \\ &= (MP1 - ZP) - (m_{Cr} + m_{absorbent}) + \rho_{gas/vapor} (V_{Cr} + V_{adsorbent}) \quad (\text{Eq. 2.10}) \end{aligned}$$

It should be noted that MP2 can be used instead of MP1 for calibration and determination of the excess adsorbed amount.

MSB presents an uncertainty of 10 μg and operates up to 150 bar (15 MPa) and 150°C. The temperature within the adsorption chamber is measured with a PT100 probe with an accuracy of $\pm 0.1^\circ\text{C}$. The pressure is measured with a pressure gauge from Wika with a full-scale accuracy of $\pm 0.025\%$. The global uncertainty associated to the adsorbed mass is less than 1%.

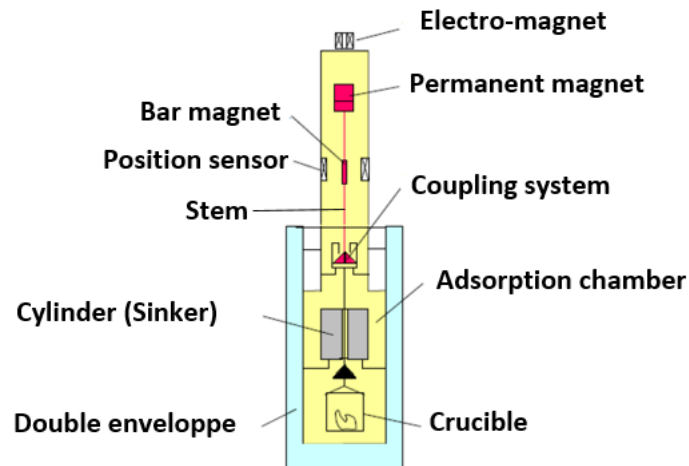


Figure 2. 7. Magnetic suspension balance (MSB). Adapted from [9].

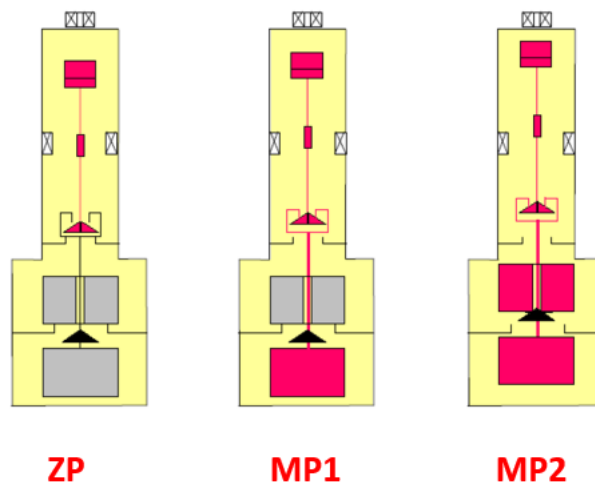


Figure 2. 8. Measurement positions of the MSB. Taken from [9]
(The red color corresponds to the system in suspension).

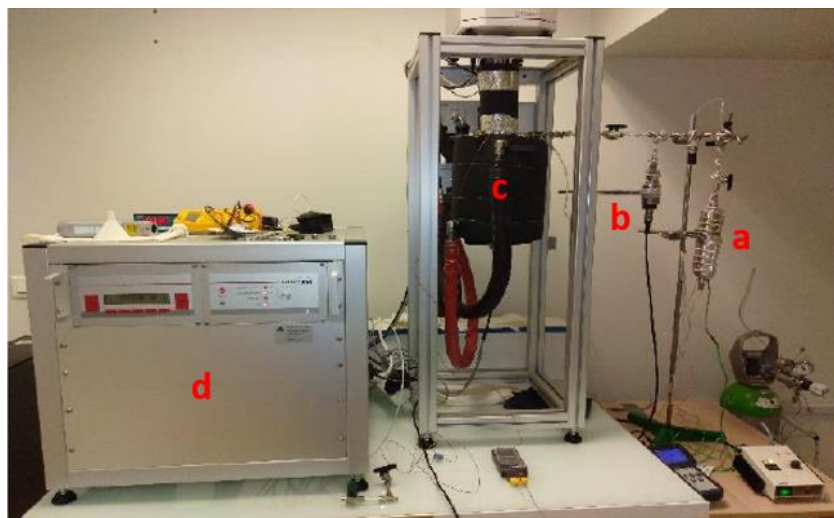


Figure 2. 9. Experimental setup used for determination of adsorption/desorption isotherms.
a) CP-tank b) Pressure gauge c) MSB d) Acquisition unit.

2.3.2.2. Calorimetric-manometric technique

In order to measure the differential enthalpy of adsorption ΔH_{diff} (defined in section 1.5.4.5.1 of Chapter 1) of CP on PACP, a homemade calo-manometric device connected to CP-tank partially filled with CP (steam generator) was used [9,15] (Figure 2.10a). Since ΔH_{diff} presents the adsorption enthalpy of an adsorptive (here CP) on a given porous material (here PACP) reported to the amount of adsorbate (here adsorbed CP), one needs to combine the manometric technique, used for determining the adsorbed amounts on a given adsorbent, and the calorimetric technique, used for evaluating the associated heat. To do so, Mouahid *et al.* (2010) [9] developed an experimental setup based on the combination of both calorimetric and manometric techniques in order to evaluate the differential enthalpy. They used a C80 calorimeter from Setaram in which they implemented a manometric unit. The calorimeter consists basically of a calorimetric block, which is heated/cooled using a resistance/ventilator, hosting both a reference and measurement cell. It is based on Calvet principle (*i.e.* the cells are completely surrounded by thermocouple network, known as 3D CALVET sensor) and adapted to perform measurements at high temperatures (from ambient temperature to 250 °C) and isothermal conditions. The calorimetric signal (electric signal) delivered from the sensor is proportional to a thermal power through a sensibility coefficient previously determined through a calibration based on the Joule effect. The calorimeter is controlled through a CS32 controller and a PID regulation system. Further details on calorimetric measurements are provided below in section 2.3.3.2. The manometric modulus consists basically of a dosing volume containing the adsorptive, connected through a set of 1/16 stainless tube and 1/16 valves to the measurement cell of the calorimeter containing the adsorbent. A pressure gauge (MKS Baraton type 121A; 1 to 25,000 torr (10^{-3} to 33 bar)) with 0.01 % full-scale accuracy is implemented between the dosing volume and the measurement cell. The 1/16 valves are controlled through metallic stem emerging at the surface of the manometric modulus (Figure 2.10b). The measured temperature, pressure and calorimetric signals are recorded versus time through a homemade program.

In order to determine the differential enthalpy of adsorption, both the adsorbed amounts Δn and the corresponding adsorption heat Q_{ads} are evaluated. The adsorbed amounts are determined through a mass balance before and after adsorption, as follows:

$$\Delta n (T, P_{d+M}) = \frac{V_d}{\vartheta(T, P_d)} - \frac{V_d+V_M}{\vartheta(T, P_{d+M})} \quad (\text{Eq. 2.11})$$

where $T, V_M, V_d, P_d, P_{d+M}, \vartheta(T, P_d), \vartheta(T, P_{d+M})$ are respectively the temperature of the experiment, the adsorption volume (illustrated in Figure 10b), the dosing volume, the pressure of the adsorptive (gas/vapor) within the dosing volume (*i.e.* before connecting the dosing volume with the measurement cell), the equilibrium pressure of the adsorptive within both the dosing volume and the measurement cell (*i.e.* after connecting the dosing volume with the measurement cell), the molar volume of the adsorptive at T and P_d and the molar volume at T and P_{d+M} .

The calorimetric signals $E(t)$, recorded after each injection of the adsorptive into the measurement cell, are integrated and multiplied by the sensibility coefficient k so that the corresponding energy Q is determined. This latter results from the contribution of both adsorption heat Q_{ads} and compression heat Q_{comp} .

$$Q = k \int E(t) dt = Q_{ads} + Q_{comp} \quad (\text{Eq. 2.12})$$

Compression heat corresponds to the heat resulting from both adsorptive expansion and the measurement cell compression after adsorptive injection. This latter is considered as reversible so that the compression heat expression could be established as:

$$Q_{comp} = -V_E(\alpha_p - \alpha_{ss})T\Delta P \quad (\text{Eq. 2.13})$$

where $V_E, \Delta P, T, \alpha_p, \alpha_{ss}$ are respectively the effective volume (volume effectively considered by the thermopiles illustrated in Figure 2.10b), the pressure variation in the measuring cell between two consecutive adsorption points, the temperature of the experiment, the isobaric expansion coefficient of the adsorptive and the stainless steel from which the measurement cell is manufactured.

Therefore, the heat of adsorption can be expressed as follows:

$$Q_{ads} = Q + V_E(\alpha_p - \alpha_{ss})T\Delta P \quad (\text{Eq. 2.14})$$

The differential enthalpy of adsorption ΔH_{diff} is obtained by dividing the heat of adsorption Q_{ads} by the corresponding adsorbed amount Δn as follows:

$$\Delta H_{diff} = \frac{Q + V_E(\alpha_p - \alpha_{ss})T\Delta P}{\Delta n} \quad (\text{Eq. 2.15})$$

The global uncertainty as regards the measured differential adsorption enthalpy is estimated at 5% in this work [9].

It should be noted that the adsorption isotherm can be obtained by determining the cumulative adsorbed amount at a given equilibrium pressure and the experiment temperature $n_{ads}^i(T, P_i)$ using the following equation:

$$n_{ads}^i(T, P_i) = V_d \left(\sum_{k=1}^i \frac{1}{\vartheta_{2k-2}} - \sum_{k=1}^i \frac{1}{\vartheta_{2k-1}} \right) - \frac{V_M}{v_{i+1}} \quad (\text{Eq. 2.16})$$

The quantities of equation 2.16 are those defined in equation 2.11.

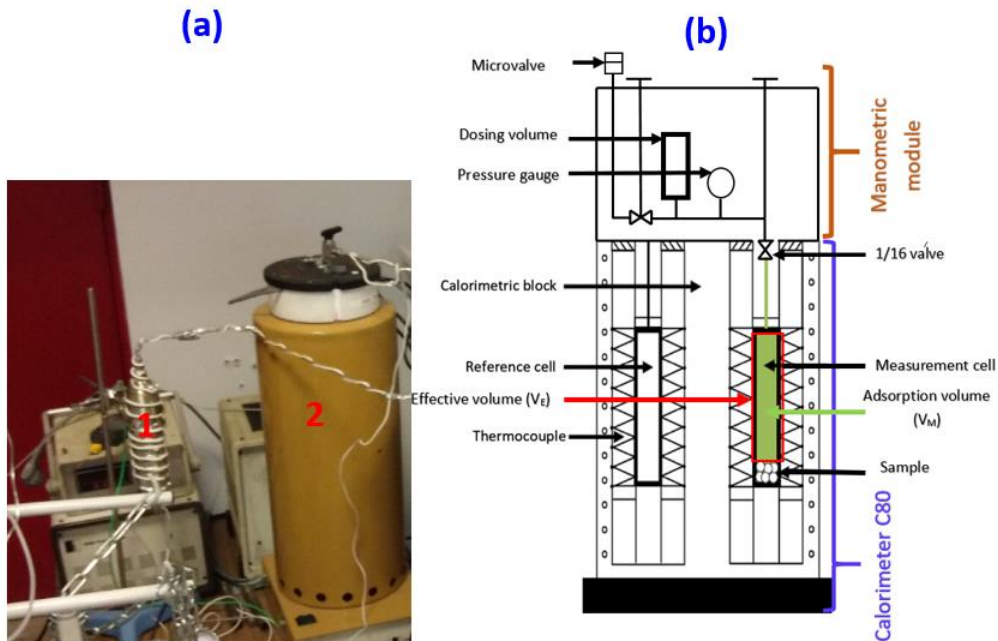


Figure 2. 10. Calometric-manometric apparatus developed by Mouahid et al. (2010) [9].
 (a) experimental setup used for determining the differential enthalpy of adsorption
 (1) CP-tank (2) calorimetric/manometric device
 (b) schematic of calo-manometric device. Adapted from [9].

2.3.2.3. Gas Porosimetry

After the measurement of CP desorption from PACP (using the gravimetric technique), the PACP were subjected to primary vacuum at 30°C during 24 hrs. These post-desorption PACP were analyzed by gas porosimetry (argon at 87 K) in order to study the effect of PSD, temperature and CP-loading method on CP-trapping. For that reason, both the automatic quick outgassing and leak test steps occurring before the first-measured point were skipped. This technique is explained in section 2.3.1.2 for virgin-PACP characterization.

2.3.2.4. Thermogravimetric analysis

With the aim to determine the temperature at which CP is completely desorbed from the PACP, the post-desorption PACP were analyzed with thermogravimetric analysis (TGA) using TGA 2 from Mettler Toledo. TGA is a technique used for thermal characterization of materials. It monitors the mass of a substance, which is placed in a controlled atmosphere and subjected to a temperature ramping, as a function of temperature or time.

Indeed, the sample is introduced in a crucible placed on a highly-sensitive balance within a furnace under an inert gas flow (such as helium). The temperature of the system is controlled and the mass of the sample is continuously monitored so that a mass-loss curve, expressing the variation in the sample mass as a function of temperature or time, is generated.

2.3.3. Analysis of hydrate formation from CP-loaded PACP

The PACP were loaded with CP using direct liquid imbibition or vapor adsorption. The CP-loaded PACP were immersed in water at a subcooling of 6°C (*i.e.* 6°C below the hydrate equilibrium temperature) so as to form hydrate. Depending on the targeted analysis, the hydrate formation experiments were performed either in batch-chemical reactors, or DSC and μ DSC cells, or a transparent glass cell. From there, water-to-hydrate conversion (WHC), CP conversion rate, the prevailing energetic phenomena and hydrate crystals morphology were respectively evaluated.

2.3.3.1. Batch-chemical reactors

In order to form CP hydrates and evaluate hydrate formation from CP-loaded PACP, batch-chemical reactors were used. The hydrate formation kinetics and the formed hydrate amount, expressed as variants of WHC ($R\dot{W}HC$ and $RW\dot{H}C_f$, respectively (see section 3.2.2 in Chapter 3)), were deduced from refractive index measurements of the solution not converted to hydrate (Figure 2.11). The two reactors were similar jacketed glass vessels of 1-L capacity. Each reactor was fitted with a mechanical stirrer with a 4-bladed glass double propeller-stirrer shaft. A Lauda cryostat (RE 1050 GTM), with a silicone oil (Kryo 51TM) as a refrigerant, controlled the temperature inside the reactors. The reactor temperature, measured with a PT100 temperature sensor ($\pm 0.15^\circ\text{C}$ uncertainty), was recorded by a data logger and a computer at regular intervals. The reactors have several inlets and outlets: the former were used to introduce brine and CP-loaded PACP, and the latter to collect the samples of the unconverted water. The refractive index n_D of the collected brine samples was measured using an Abbemat 3200 refractometer. The sample salinity was then deduced using a “ $n_D - [\text{NaCl}]$ ” calibration curve previously determined [16].

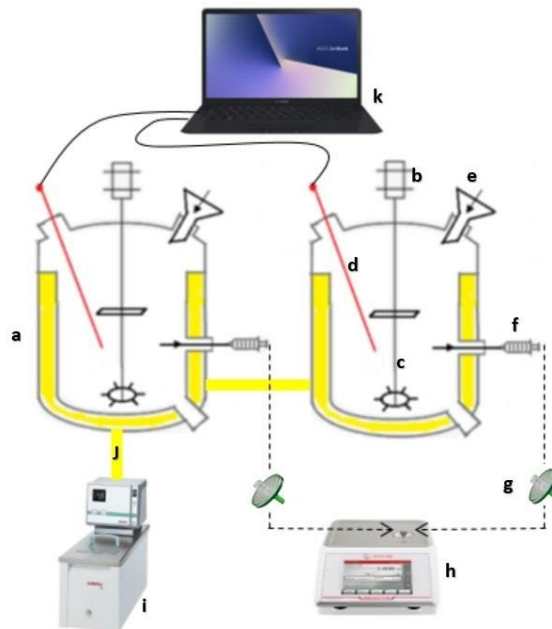


Figure 2. 11. Experimental setup for CP-hydrate formation: a) 1-L reactor, b) mechanical stirrer, c) stirring shaft, d) temperature sensor (PT100), e) funnel, f) syringe, g) syringe filter (0.8 μm), h) refractometer, i) cryostat, j) refrigerant fluid.

2.3.3.2. Calorimetric measurements

Calorimetry is a fundamental technique for thermal analysis of materials. It is mainly used for determining their thermophysical properties (heat capacity, etc.), transitions (vitreous, eutectic, etc.) and phase changes (dissociation enthalpy). In this thesis, CP-conversion rate and the prevailing thermal energies, in particular CP desorption and/or hydrate crystallization ones, as a result of hydrate formation from CP-loaded PACP were evaluated using two calorimeters: differential scanning μ DSC7 evo and Tian-Calvet BT2.15 calorimeters. Both calorimeters present a calorimetric block hosting measurement and reference cells surrounded by a network of thermocouples forming the heat flow sensor. This latter is differential, that is the heat flow data of the measurement cell are constantly compared with the heat flow data of the reference cell. Accordingly, the heat effects mainly associated to the heat capacity of the cell are deducted [17].

The sensor measures an electrical signal proportional to a thermal power and obtained through a calibration based on Joule effect. Thus, a proportionality coefficient, known as sensibility coefficient is determined. The sample temperature is measured using a platinum-resistance sensor placed within the calorimetric block rather than the sample. Therefore, a temperature deviation is observed mainly due to the time taken for heat transfer through the measurement cell wall. Accordingly, temperature correction is realized through several standard materials of well-known fusion temperatures.

2.3.3.2.1. Differential scanning calorimeter micro-DSC7 evo

A differential scanning calorimeter (DSC) is a thermal-analysis apparatus used for a direct assessment of the heat energy uptake taking place in a sample within a regulated increase or decrease in temperature (Figure 2.12) [18]. Micro-DSC7 evo (from Setaram instrumentation) was mainly used for determining the CP conversion rate after applying several hydrate formation/dissociation cycles thanks to relatively fast heating and cooling of the cell within and outside the hydrate zone stability. The measurement and reference cells (1-mL capacity) are made of Hastelloy. Each cell is surrounded with a plan network of thermocouples so that to measure heat flow. The calorimetric block is thermally related to three

enclosures heated/cooled with a Peltier module and water circulation provided by a thermostatic water bath. The calorimetric block is permanently swept with inert gas (nitrogen) in order to avoid moisture condensation. The calorimeter is controlled through a set of modules (CPU, command, amplification, acquisition) and PID regulation using Calisto software. The obtained uncertainties as regards the measured energy and temperature are 2% and 0.2°C, respectively.

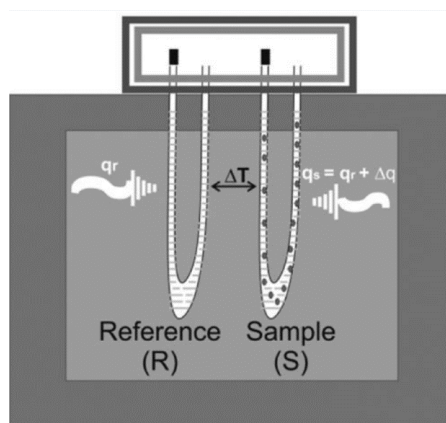


Figure 2. 12. Principle of DSC measurements. Taken from [18].

2.3.3.2.2. Tian-Calvet BT2.15 calorimeter

The Tian-Calvet BT2.15 calorimeter was employed for determining the absorbed/released thermal energies during hydrate formation mainly at an isotherm mode (constant temperature corresponding to a subcooling of 6 °C). The calorimetric block is heated using a resistance and cooled with ethanol circulation, provided by a thermostatic bath (Huber CC410) together with an internal ventilator. It hosts the measurement and reference stainless steel cells (7-mL capacity), both surrounded with a cylindrical network of thermocouples (9 rings of 19 thermocouples each) [17]. The thermocouple arrangement, known as 3D-Calvet sensor (Figure 2.13), allows the heat flow measurement in all directions. The calorimeter is controlled through a CS32 controller and PID regulation using CALISTO software. The obtained uncertainties as regards the measured energy and temperature are 4% and 0.25°C, respectively.

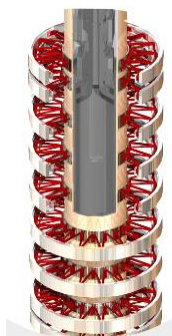
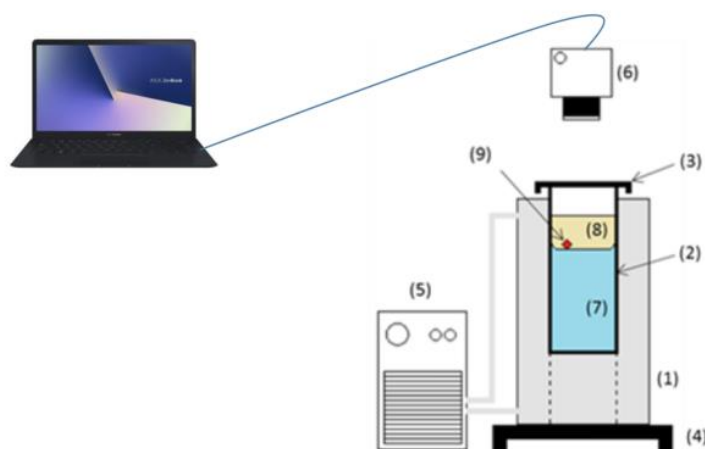


Figure 2. 13. 3D-Calvet sensor. Taken from [19].

2.3.3.3. Optical microscopy

A binocular magnifier was used in order to observe the hydrate crystals formed from the CP-loaded PACP. For this purpose, water and CP-loaded PACP were introduced into a sealed cylindrical glass cell of 3 cm diameter and 30 mL capacity. The cell was placed in a cylindrical metal-jacketed vessel, through which ethane-diol was circulated to control the temperature. The water/CP interface was observed using a binocular magnifier (Wild Heerbrugg) fitted with a CCD camera (IDS UI124xSE-C) and positioned above the glass cell. The cell was backlit by an LED light table (Edmund Optics) (Figure 2.14 [20]). The snapshots of the interface were recorded on a PC at regular intervals using a homemade program. It should be noted that this technique was also used to measure the hydrate growth rate in a system without PACP.



*Figure 2. 14. Experimental setup used in observing hydrate formation. Adapted from [20]
(1) Double envelope, (2) Glass cell, (3) Petri dish, (4) LED slate, (5) Cryostat,
(6) Binocular (7) Brine, (8) Cyclopentane, (9) CP-hydrate seed.*

2.4. Conclusion

In this Chapter, we described the different experimental techniques and setups used to accomplish the present thesis namely the PACP characterization, CP adsorption-desorption from/on PACP and hydrate formation from the CP-loaded PACP. The batch-chemical reactors setup is used in Chapter 3. Chapter 4 involved a set of techniques: gas porosimetry, gravimetric, calo-manometric and TGA. Besides calorimetry, gas porosimetry and MIP are also used in Chapter 5. Finally, Chapter 6 only requires the use of calorimetry and refractive index measurements. The obtained results are presented in the next Chapters.

2.5. References

- [1] Assael MJ, Dalaouti NK, Measurement of the viscosity of cyclopentane from 210 to 310 K and pressures up to 25 MPa. *High Temp - High Press* **2000**; 32:179–84. <https://doi.org/10.1068/htwu197>.
- [2] <https://www.manualslib.com/manual/2187695/Malvern-Mastersizer-2000.html?page=3#manual>
- [3] Brochette P. Émulsification - Élaboration et étude des émulsions. *Techniques de l'ingénieur* **2013**.
- [4] https://fr.wikipedia.org/wiki/Diffusion_statique_de_la_lumi%C3%A8re
- [5] Thommes M, Kaneko K, Neimark AV, Olivier JP, Rodriguez-Reinoso F, Rouquerol J, et al. Physisorption of gases, with special reference to the evaluation of surface area and pore size distribution (IUPAC Technical Report). *Pure Appl. Chem.* **2015**; 87. <https://doi.org/10.1515/pac-2014-1117>.
- [6] Keller JU, Staudt R, editors. *Volumetry / Manometry, Gas Adsorpt. equilibria exp. methods adsorpt. isotherms*, Boston, MA: Springer US, p. 79–116, **2005**; https://doi.org/10.1007/0-387-23598-1_3.
- [7] Thommes M, Cychosz K, Neimark A. Advanced Physical Adsorption Characterization of Nanoporous Carbons. *Nov. Carbon Adsorbents*, p. 107–45, **2012**, <https://doi.org/10.1016/B978-0-08-097744-7.00004-1>.
- [8] Landers J, Gor GYu, Neimark AV. Density functional theory methods for characterization of porous materials. *Colloids Surf Physicochem Eng. Asp.* **2013**; 437:3–32. <https://doi.org/10.1016/j.colsurfa.2013.01.007>.
- [9] Mouahid A, Mise au point point d'un dispositif couple manométrique calorimétrique pour l'étude de l'adsorption de fluides supercritiques dans des milieux microporeux et mesoporeux. *Physique[physics]*. Université de Pau et des Pays de l'Adour., **2010**. Français. NNT : 10PAUU3020. tel-00573997.
- [10] Brakel J, Modrý S, Svatá M, Mercury porosimetry: state of the art **1981**. [https://doi.org/10.1016/0032-5910\(81\)85001-2](https://doi.org/10.1016/0032-5910(81)85001-2).
- [11] Zhang Y, Yang B, Yang Z, Ye G, Ink-bottle effect and pore size distribution of cementitious materials identified by pressurization-depressurization cycling mercury intrusion porosimetry. *materials* **2019**; 12. <https://doi.org/10.3390/ma12091454>.
- [12] Webb PA, An introduction to the physical characterization of materials by mercury intrusion porosimetry with emphasis on reduction and presentation of experimental data. *Micromeritics Instrument Corp, Norcross, Georgia* **2001**.

- [13] Khaddour F, Knorst-Fouran A, Plantier F, Piñeiro MM, Mendiboure B, Miqueu C. A fully consistent experimental and molecular simulation study of methane adsorption on activated carbon. *Adsorption* **2014**; 20:649–56. <https://doi.org/10.1007/s10450-014-9611-2>.
- [14] Wang JY, Mangano E, Brandani S, Ruthven DM, A review of common practices in gravimetric and volumetric adsorption kinetic experiments. *Adsorption* **2021**; 27:295–318. <https://doi.org/10.1007/s10450-020-00276-7>.
- [15] Mouahid A., Bessieres. D., Plantier. F., Pijaudier-Cabot G., A thermostated coupled apparatus for the simultaneous determination of adsorption isotherms and differential enthalpies of adsorption at high pressure and high temperature. **2011**.
- [16] Mallek R, Miqueu C, Jacob M, Le Mélinaire P, Dicharry C. Effect of porous activated carbon particles soaked in cyclopentane on CP-hydrate formation in synthetic produced water. *J. Water Process Eng.* **2020**; 38:101660. <https://doi.org/10.1016/j.jwpe.2020.101660>.
- [17] Delroisse H, Plantier F, Marlin L, Dicharry C, Frouté L, André R, et al., Determination of thermophysical properties of cyclopentane hydrate using a stirred calorimetric cell. *J. Chem. Thermodyn.* **2018**; 125:136–41. <https://doi.org/10.1016/j.jct.2018.05.023>.
- [18] Gill P, Moghadam TT, Ranjbar B. Differential Scanning Calorimetry Techniques: Applications in Biology and Nanoscience, *J. Biomol. Tech. JBT* **2010**; 21:167–93.
- [19] <https://setaramsolutions.com/fr/solutions-standard/calorimetres-calvet>
- [20] Delroisse H, Torr  JP, Dicharry C, Effect of a hydrophilic cationic surfactant on cyclopentane hydrate crystal growth at the water/cyclopentane interface, *Cryst. Growth Des.* **2017**; 17:5098–107. <https://doi.org/10.1021/acs.cgd.7b00241>.

Chapter 3. Effect of porous activated carbon particles soaked in cyclopentane on CP-hydrate formation in synthetic produced water

3.1. Introduction

This chapter deals with the hydrate formation stage of BGH process. In this part of the work, CP hydrates were formed in two stirred-glass reactors of 1-L capacity. Hydrate formation kinetics and hydrate-formed amount vs. time were determined from refractive index measurements of the unconverted water. The effects of the presence of CP-loaded PACP, stirring rate, CP-loading rate, PACP size and water salinity were evaluated. Prior to this, preliminary experiments were performed without PACP to evaluate the thermodynamic and kinetic effects of NaCl on CP-hydrate formation. The results presented in this chapter have been reported in a publication cited as follows:

Rafik Mallek, Christelle Miqueu, Matthieu Jacob, Pascal Le Mélinaire, Christophe Dicharry, Effect of porous activated carbon particles soaked in cyclopentane on CP-hydrate formation in synthetic produced water, Journal of Water Process Engineering, Volume 38, 2020, 101660, ISSN 2214-7144, <https://doi.org/10.1016/j.jwpe.2020.101660>.

3.2. Experimental methods

3.2.1. Preliminary investigation

The aim of the preliminary experiments without PACP was to analyze the effect of NaCl concentration on both the CP-hydrate equilibrium temperature and CP-hydrate growth rate. Moreover, they served to choose the initial experimental conditions (initial water salinity; initial experimental temperature), referred to as the “starting points” in the following sections, for assessing the hydrate formation in BGH process.

3.2.1.1. Effect of NaCl concentration on CP-hydrate equilibrium temperature

Fourteen flasks, each containing 2 g of CP, 18 g of water with different NaCl concentrations between 0 and 23 wt%, and a small rod (to promote fluid mixing), were prepared, split into two concentration groups (group#1 (< 10 wt% NaCl) and group#2 (> 10 wt% NaCl)), and placed in two cryostats. Group#1 and group#2 were cooled down to -10°C and -22°C respectively and maintained at these temperatures for 24 hrs to form ice. The ice was then melted by increasing the bath temperature to -4 and -18°C for group#1 and #2 respectively in order to trigger hydrate formation. The flasks were shaken manually at regular intervals over the course of 16 hrs to promote the formation of CP hydrates. The bath temperature was then increased to 0 and -14°C for group#1 and #2 respectively. These temperatures were 1°C lower than the lowest CP-hydrate equilibrium temperatures at NaCl concentrations of 10 wt% and 23 wt% found in the literature [1–4].

The CP-hydrate equilibrium temperatures were determined using a “step-heating method” [5], which consists in applying a stepwise heating method combined with a sufficiently long equilibrium time at each step. In our experiments, the bath temperature was increased by steps of 0.2°C and maintained at the new temperature for 4 to 12 hrs. The bath temperature was monitored using a PT100 probe ($\pm 0.15^{\circ}\text{C}$ uncertainty). The presence of CP hydrates in the flasks was visually checked at each step. If CP hydrates were still present, the flask was manually shaken before the next temperature increase. When only a small amount of CP hydrates remained, the temperature step was reduced to 0.1°C . The process was

repeated until the last CP-hydrate crystals had melted. The CP-hydrate equilibrium temperatures were calculated as the arithmetic mean of the last two temperatures (before and after the last CP-hydrate crystals melting). Any uncertainties regarding the measured equilibrium temperatures were evaluated as the sum of PT100 uncertainty ($\pm 0.15^\circ\text{C}$) and either $\pm 0.05^\circ\text{C}$, for the temperature step of 0.1°C , or $\pm 0.1^\circ\text{C}$ if the CP-hydrate crystals had melted, before the temperature step was reduced from 0.2 to 0.1°C .

3.2.1.2. Effect of NaCl concentration on CP-hydrate growth rate

In order to determine the hydrate growth rate at different NaCl concentrations, optical microscopy was employed. Nine aqueous solutions with different NaCl concentrations (0, 1, 2, 3.5, 4, 6, 8, 10, and 16 wt%) were prepared. 20 mL of NaCl solution and 4 mL of CP were transferred to the cylindrical glass cell. The latter was placed in the metal-jacketed vessel and covered with a petri dish to limit CP evaporation. The temperature of the system was set such as to obtain the desired subcooling. Two different subcoolings (2°C and 6°C) were investigated: at 6°C , the lateral hydrate growth rates of all the different NaCl preparations were measured, whereas at 2°C , they were measured only for NaCl concentrations of 0, 3.5, 10, and 16 wt%. Hydrate crystallization was triggered by seeding the system with a few CP-hydrate crystals prepared beforehand. Because of their intermediate density, the seeds settled at the water/CP interface. The binocular magnifier was then focused on the crystals located on the flat part of the interface (around the vertical shaft of the cell). The lateral hydrate growth rate (GR) was evaluated by measuring the distance covered by the hydrate crystallization front at the water/CP interface in a given growth direction on two snapshots taken at different times. Three measurements were performed, each on a different point of the crystallization front, and the mean GR value was calculated. The GR uncertainty was calculated as the deviation from the mean GR value. The uncertainty of the imposed subcooling was $\pm 0.3^\circ\text{C}$.

3.2.2. Hydrate formation experiments in BGH process

The effects of the presence and absence of PACP at different stirring rates and, in the case of the system with PACP, the effect of CP-loading rate, PACP size and water salinity on the CP-hydrate formation kinetics and the total hydrate-formed amount were investigated.

For this purpose, a series of experiments was carried out using the setup described in section 2.3.3.1 Chapter 2. Synthetic water was first introduced into the batch-chemical reactors and cooled down to the experiment temperature. Stirring was started and set to the target rate (0, 180, or 360 rpm). Alongside that, CP - or PACP soaked in CP - were cooled in a freezer for 16 hrs to -0.5°C and 0.5°C respectively, before being introduced into the reactors. This procedure was used to prevent hydrate crystallization before the system temperature reached the target experiment temperature. Note that, to avoid moisture crystallizing on the soaked PACP - which could trigger hydrate formation before the PACP were introduced into the reactors - these latter were not cooled to negative temperatures in the freezer. If they had been, it would have been impossible to evaluate the effect of PACP on induction time since hydrate formation would have been spontaneous.

The hydrate formation kinetics were quantified based on the induction time for hydrate crystallization t_{ind} and the relative water-to-hydrate conversion rate $R\dot{W}HC$ determined one hr after the onset of hydrate crystallization:

- t_{ind} was calculated as the time elapsed from the moment when CP or the soaked PACP were introduced into the reactor to the start of temperature increase due to hydrate crystallization. Note that when hydrate crystallization did not occur in the first two hrs, it was triggered by seeding the system with a few CP-hydrate crystals prepared beforehand. Moreover, t_{ind} was measured only in the experiments where the effect of PACP and the stirring rate were investigated. In the other experiments, hydrate crystallization was systematically initiated by seeding the system with a few CP-hydrate crystals.

- $R\dot{W}HC$ was calculated as $R\dot{W}HC = \frac{100}{\Delta t} \Delta \frac{WHC}{WHC_{th,max}}$ where $\Delta t = 1\text{hr}$ and WHC is the water-to-hydrate conversion, $WHC_{th,max}$ the maximum value of WHC that should be obtained, either when all the CP

initially present in the system is converted to hydrates or when the system reaches the CP-hydrate equilibrium curve (Figure 3.1). In all the experiments of this study, water was in excess since the molar ratio of water to CP is 30:1, which is greater than the stoichiometric water to CP molar ratio for complete conversion to hydrate (17:1).

The amount of hydrates formed at time t was quantified through $RWHC = 100 \times \left(\frac{WHC}{WHC_{th,max}} \right)_t$, and

the final amount of hydrates formed was quantified through $RWHC_f = 100 \times \left(\frac{WHC}{WHC_{th,max}} \right)_{t=t_f}$ where

t_f is the time at which the experiment is stopped.

During the experiments, WHC was determined based on the difference between the initial water salinity $[NaCl]_{t_0}$ and the water salinity at time t $[NaCl]_t$ using Equation 3.1.

$$WHC = 100 - \frac{100 * [NaCl]_{t_0} * (100 - [NaCl]_t)}{(100 - [NaCl]_{t_0}) * [NaCl]_t} \quad (\text{Eq. 3.1})$$

$[NaCl]_t$ was obtained from the refractive index (nD) measurement of the NaCl solution sample collected at time t and using the following “nD – [NaCl]” (see Appendix A-1) calibration equation (Equation 3.2):

$$[NaCl] = 564.55 \text{ nD} - 752.49 \quad (\text{Eq. 3.2})$$

The nD measurements were performed at 20°C. The samples collected were filtered to remove any suspended solids (hydrate crystals, PACP or impurities) before measuring nD. We checked that the use of filters and the solubility of CP in water (86 mg/L at 10°C [6]) did not impact the nD values obtained. A check was also run to make sure that NaCl did not adsorb on the PACP at the salinities used (3.5, 10, and 16 wt%).

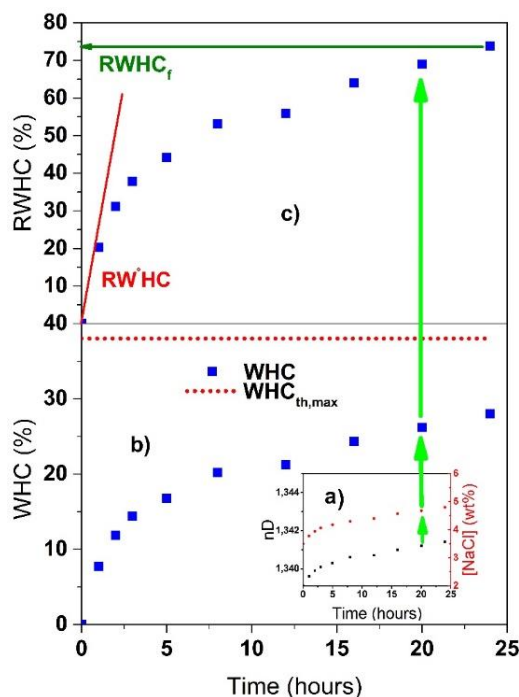


Figure 3. 1. Experimental procedure to determine the relative water-to-hydrate conversion rate ($RWHC$) and the final relative water-to-hydrate conversion rate ($RWHC_f$). a) Measured refractive index of the synthetic PW and deduced NaCl concentration vs. time (insert), b) calculated water-to-hydrate conversion (WHC) vs. time, c) determination of $RWHC$ and $RWHC_f$.

All the hydrate formation experiments performed in the glass reactor were duplicated. Consequently, each experimental point and value given in the corresponding figures and tables is the mean value of two experiments. The error bars in the figures and the uncertainties in the tables are calculated as the difference between the mean and minimum experimental values.

3.2.2.1. Effect of PACP and stirring rate on CP-hydrate formation

The CP-hydrate formation experiments - without and with Gbac loaded with 0.8 g of CP per gram of PACP - were conducted at the starting point 1 (3.5 wt% NaCl; -0.5°C) and at stirring rates of 0, 180, and 360 rpm for 78 hrs. For these experiments, 777.2 g of a NaCl solution (750 g of deionized water and 27.2 g of NaCl) and 100 g of CP - or 125 g of PACP soaked in 100 g of CP - were introduced into each reactor where the temperature was set to -0.5°C . Stirring started once the system temperature had reached the target temperature.

3.2.2.2. Effect of the CP-loading rate of PACP on CP-hydrate formation

The CP-hydrate formation experiments were conducted using Gbac loaded with 0.5, 0.65, 0.8, and 1 g of CP per gram of PACP, at the starting point 1 (3.5 wt% NaCl; -0.5°C) for 24 hrs. 0.8 g of CP per gram of PACP was the loading rate typically used by the start-up BGH in its tests to work out its HBD process. Note that at this CP-loading rate, the particles were wet and stuck together, which suggests that both their pores and external surface were saturated with CP. The other loading rates used in the present study were chosen such as to evaluate the effect of this parameter on the hydrate formation kinetics and water-to-hydrate conversion over a range on either side of this value. For the CP-hydrate formation experiments, 777.2 g of a NaCl solution (750 g of deionized water and 27.2 g of NaCl) and 125 g of PACP soaked in 62.5, 81.25, 100 and 125 g of CP respectively were introduced into each reactor where the temperature was set to -0.5°C . A stirring rate of 180 rpm was used.

3.2.2.3. Effect of the size of PACP on CP-hydrate formation

The CP-hydrate formation experiments were conducted using Gbac (average particle diameter 700 μm) and Abac (average particle diameter 400 μm) loaded with 0.8 g of CP per gram of PACP, at the starting point 1 (3.5 wt% NaCl; -0.5°C) for 24 hrs. For these experiments, 777.2 g of a NaCl solution (750 g of deionized water and 27.2 g of NaCl) and 125 g of PACP soaked in 100 g of CP were introduced into each reactor where the temperature was set to -0.5°C . A stirring rate of 180 rpm was used.

3.2.2.4. Effect of water salinity on CP-hydrate formation

In this part of the study, the CP-hydrate formation experiments were performed at two additional starting points defined as starting point 2 (10 wt% NaCl; -4.9°C) and starting point 3 (16 wt% NaCl; -9.5°C) for 24 hrs. Although the operating points 1, 2 and 3 have different temperatures, they have the same initial subcooling of 6°C . The PACP used were Gbac loaded with 0.8 g of CP per gram of PACP. A stirring rate of 180 rpm was used.

3.3. Results and discussion

3.3.1. Effect of NaCl on CP-hydrate formation

3.3.1.1. Effect of NaCl concentration on CP-hydrate equilibrium temperature

The CP-hydrate equilibrium temperatures obtained at the different NaCl concentrations investigated (0 to 23 wt%) are plotted in Figure 3.2 and the measured values are given in Table 3.1. As expected, the increase in water salinity resulted in a decrease of the CP-hydrate equilibrium temperatures. Our experimental values are consistent with those published by Ho-Van *et al.* (2018) [1], Delroisse *et al.* (2017) [4], Zyliftari *et al.* (2013) [3] and Kishimoto *et al.* (2012) [2] (Figure 3.2). More precisely, they range between the equilibrium points found in Ho-Van *et al.*'s study (2018), determined by what they called rapid and slow processes. Ice equilibrium temperatures for the same range of NaCl concentrations are also shown in Figure 3.2 [7]. The starting points used for the hydrate formation experiments conducted in the glass reactors should be chosen in the region between the CP-hydrate and ice curves.

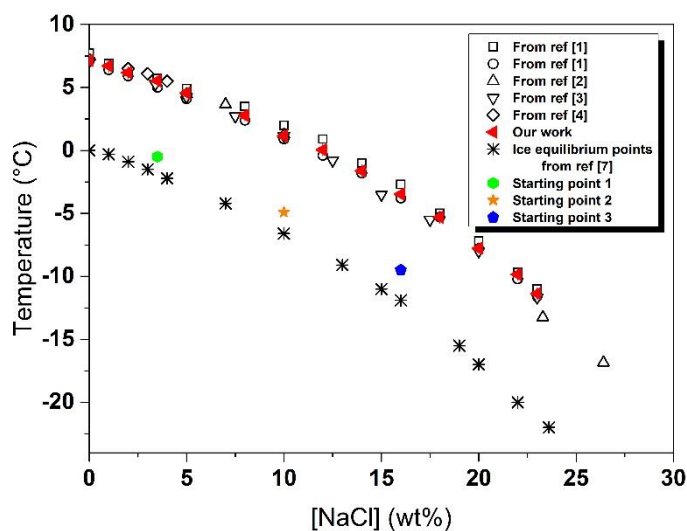


Figure 3. 2. CP-hydrate and ice equilibrium temperatures as a function of NaCl concentration. This graph also shows the three initial experimental conditions (starting points 1, 2 and 3) used for the CP-hydrate formation experiments.

Table 3. 1. CP-hydrate equilibrium temperatures (T_{eq}) measured at different NaCl concentrations ([NaCl]).

[NaCl] ^a (wt%)	0	1	2	3.5	5	8	10
T_{eq} (°C)	7.13 ±	6.72 ±	6.18 ±	5.53 ±	4.56 ±	2.78 ±	1.15 ±
	0.20	0.20	0.25	0.19	0.26	0.24	0.21
[NaCl] ^a (wt%)	12	14	16	18	20	22	23
T_{eq} (°C)	-0.05 ±	-1.63 ±	-3.47 ±	-5.3 ±	-7.78 ±	-9.85 ±	-11.37 ±
	0.20	0.20	0.20	0.19	0.18	0.20	0.20

^a: ± 0.01 wt%

3.3.1.2. Effect of NaCl concentration on CP-hydrate growth rate

In these experiments, CP-hydrate formation and growth occurred at the (quiescent) water/CP interface. A thin hydrate layer ended up covering the entire water/CP interface (~7.1 cm²) available. Once the latter was totally covered, the hydrate growth stopped. Consequently, only a very small amount of hydrates formed in the system compared to the volume of NaCl solution (20 mL). This implies that the water salinity remained almost constant and that the imposed subcooling varied very little during hydrate formation. The measured lateral hydrate growth rate at the NaCl concentrations investigated (0 to 16 wt%) and the subcoolings of 2 and 6°C are shown in Figure 3.3. Images showing the morphology of the CP-hydrate crystals formed are provided in Appendix A-2. The CP-hydrate crystal morphology was found to depend essentially on the imposed subcooling. The lateral hydrate growth rate values obtained at these subcooling conditions are consistent with those measured by Kishimoto *et al.* (2012) [2] at around the same subcoolings.

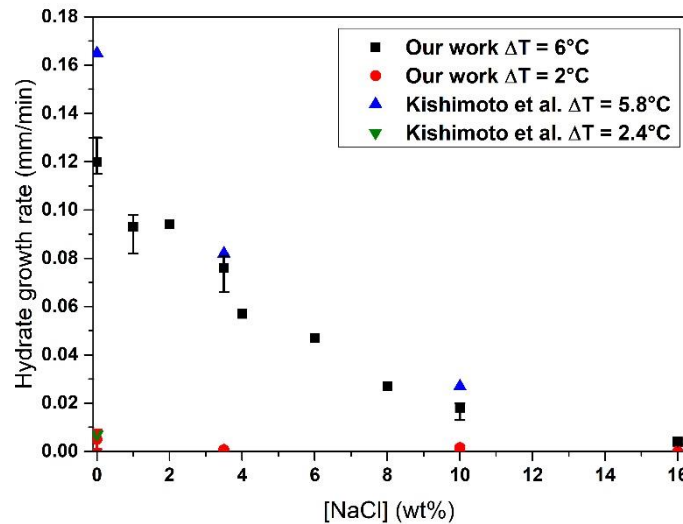


Figure 3.3. Measured lateral growth rate of CP-hydrates formed at the water/CP interface, at different NaCl concentrations and subcoolings of 2 and 6°C.

We can see that both the NaCl concentration and the imposed subcooling drastically affect the hydrate growth rate. The latter decreases as the water salinity at a given subcooling increases and rises with the subcooling at a given salinity. The subcooling acts as a driving force and NaCl as a kinetic inhibitor for hydrate formation (in addition to its thermodynamic inhibitor effect (see section 3.3.1.1)). According to the results shown in Figure 3.3, a high subcooling must be chosen to obtain a high hydrate growth rate in a hydrate-based desalination process. Consequently, in all the hydrate formation experiments performed, a subcooling of 6°C was chosen so that the system was deep inside the hydrate stability zone but remained outside the ice stability zone (see the three starting points in Figure 3.2). However, it is important to keep in mind that i) the introduction of the soaked PACP into the reactor, ii) the exothermicity of hydrate crystallization and, iii) the consumption of water molecules by the growing hydrate phase (which causes an increase in the salinity of the remaining liquid water and thus a decrease in the CP-hydrate equilibrium temperature) caused the subcooling to drop during the hydrate formation experiments. Considering these effects, we determined that the minimum subcoolings reached during the experiments performed at the starting points 1, 2 and 3 were 3.9, 4.1, and 5.1°C respectively. Note that the decrease in the imposed subcooling was mainly due to the exothermicity of the crystallization and the increase in salinity and not to the introduction of the soaked PACP into the reactor.

3.3.2. Hydrate formation experiments in BGH process

3.3.2.1. Effect of PACP and stirring rate on CP-hydrate formation

The effects of the presence of PACP (Gbac loaded with 0.8 g of CP per gram of PACP) and of the stirring rate on CP-hydrate formation are shown in Figure 3.4 and Table 3.2. For ease of comparison, data in Figure 3.4 are presented with a common base time $t = 0$, which corresponds to the onset of hydrate crystallization (whether the crystallization occurred spontaneously or had to be triggered by adding a few CP-hydrate crystals).

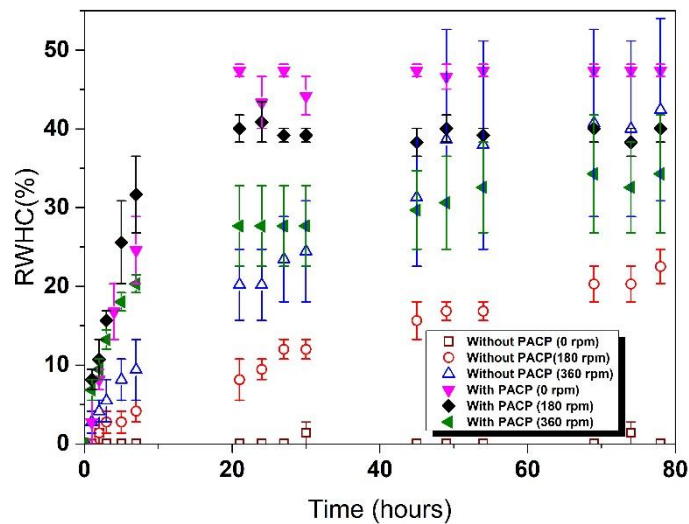


Figure 3. 4. Effect of PACP (Gbac loaded with 0.8 g of CP per gram of PACP) and stirring rate on the relative water-to-hydrate conversion. The NaCl concentration is 3.5 wt%.

Table 3. 2. Values of the induction time, the relative water-to-hydrate conversion rate and the final relative water-to-hydrate conversion (at $t = 78$ hrs) for the systems with and without PACP (Gbac loaded with 0.8 g of CP per gram of PACP) and different stirring rates. The initial conditions for these experiments correspond to starting point 1 (Figure 3.2).

Stirring rate (rpm)	Without PACP						With PACP					
	0		180		360		0		180		360	
t_{ind} (hr)	>2	>2	>2	>2	>2	>2	~0.02	>2	~0.02	>2	>2	>2
$RWHC$ (% /hr)	~ 0		~ 0		2.8 ± 1.4		2.8 ± 2.8		8.2 ± 1.3		6.8 ± 1.3	
$RWHC_f$ (%)	~ 0		22.5 ± 2.2		42.4 ± 11.6		47.4 ± 0.8		40.0 ± 1.7		34.3 ± 7.5	

For all the experiments performed without PACP, hydrate crystallization never occurred spontaneously in the first two hrs the system spent at the target temperature of -0.5°C (*i.e.* the induction time t_{ind} was greater than two hrs). With PACP, t_{ind} lasted just a few minutes for one third of the experiments performed and more than two hrs for the others. The presence of PACP therefore increases the probability of early hydrate crystallization. The large number of nucleation sites provided by the PACP may explain this result. The stirring rates investigated do not affect the trend observed for t_{ind} .

$R\dot{W}HC$ is much higher for the system with PACP than without at a given stirring rate, and stirring increases $R\dot{W}HC$ in both systems. The increased contact area between water and CP, due either to the PACP (soaked in CP) or to the stirring of the system or both, can explain the trend observed. As expected, for the systems without PACP, a higher stirring rate ensures more efficient mixing of water and CP and thus a greater interface between the two phases. In the presence of PACP, the stirring causes dispersion of the particles, which tend to agglomerate in the water phase when no stirring is applied. However, in this case, the contact area between water and CP is predominantly controlled by the external specific surface area of the particles (in which CP is adsorbed), which does not vary with the agitation. This is why $R\dot{W}HC$ changes very little when the stirring rate is increased from 180 to 360 rpm.

$RWHC_f$ is much higher for the system with PACP than without at the stirring rates of 0 and 180 rpm. There is quite a spectacular difference in the $RWHC_f$ values obtained for the quiescent systems (0 rpm), where $RWHC_f$ after 78 hrs of experimentation is around 0 and 47.4% for the system without and with PACP, respectively. This is due to the difference in the size of the contact area between the water and the CP where hydrate formation and growth take place. Without PACP, the contact area is about 80 cm^2 (the cross-section of the glass reactor), whereas with PACP it is at least $11,000\text{ cm}^2$ (the total external surface area of the particles for 125 g of Gbac). Moreover, the variation of $RWHC_f$ with the stirring rate displays an opposite trend according to whether or not PACP are present: $RWHC_f$ increases with the stirring rate in the systems without PACP and decreases in other cases. For the former, the increase in the contact area between water and CP with stirring explains the trend observed. For the latter, the reason why $RWHC_f$ decreases as the stirring rate increases remains unclear. One of the reasons might be that the increase in the initial hydrate growth rate caused by the mixing leads to the early formation of an

impermeable hydrate crust at the surface of the PACP, which limits (or stops) the hydrate formation process. Corak *et al.* (2011) [8] observed a similar tendency in their research on CP-hydrate formation in brines (3 wt% NaCl solutions). They reported that faster hydrate crystallization led to a greater amount of encapsulated CP and thus a smaller amount of hydrates (since the encapsulated CP is unavailable for hydrate formation).

An important finding in this section is that the CP-soaked PACP both increases the hydrate formation kinetics and “supplies” the hydrate reaction with CP. Note that the kinetics enhancement of hydrate formation observed in the presence of the PACP is consistent with the results reported by other authors for submillimetric particles, which were obtained mainly within the context of methane storage [9–12].

In the following sections, the effect of the PACP CP-loading rate, PACP size and water salinity on $R\dot{W}HC$ and $RWHC_f$ are investigated. Because $RWHC$ remains almost constant for the systems with PACP after around 20 hrs of experimentation (Figure 3.4), 24 hrs was chosen as the duration for all the following experiments. A stirring rate of 180 rpm was chosen to ensure homogeneity of the system during the experiments. Moreover, hydrate crystallization was triggered by seeding the system with a few CP-hydrate crystals.

3.3.2.2. Effect of CP-loading rate of PACP on CP-hydrate formation

The effect of CP-loading rate on CP-hydrate formation is illustrated in Figure 3.5, and the corresponding values of $R\dot{W}HC$ and $RWHC_f$ are given in Table 3.3.

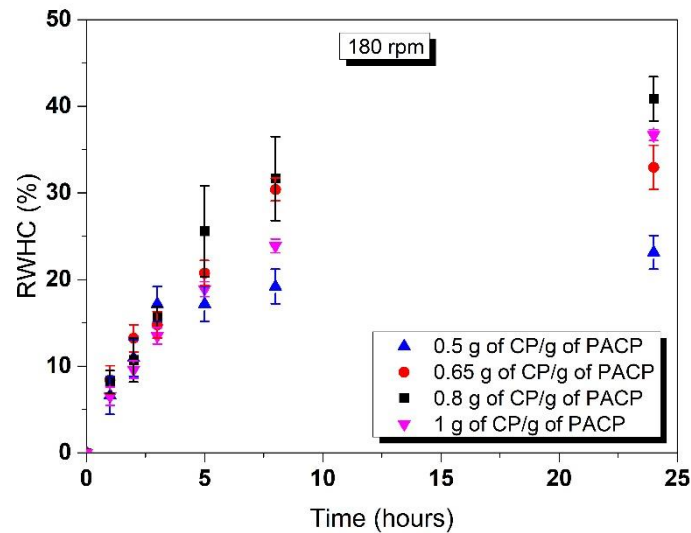


Figure 3. 5. Effect of the CP-loading rate of PACP (G_{bac}) on the relative water-to-hydrate conversion rate with 3.5 wt% NaCl. The stirring rate is 180 rpm.

Table 3. 3. Values of the relative water-to-hydrate conversion rate and the final relative water-to-hydrate conversion (at $t = 24$ hrs) for the systems with PACP (G_{bac}) at different CP-loading rates. The initial conditions for these experiments correspond to starting point 1 (Figure 3.2). The stirring rate is 180 rpm.

CP-loading rate (gram of CP per gram of PACP)	0.5	0.65	0.8	1
$R\dot{W}HC$ (% / hr)	6.6 ± 2.2	8.4 ± 1.6	8.2 ± 1.3	6.5 ± 1.1
$RWHC_f$ (%)	23.1 ± 1.9	33.0 ± 2.6	40.9 ± 2.6	36.7 ± 0.6

The $R\dot{W}HC$ points for the different CP-loading rates overlap for the first three hrs of the experiment (Figure 3.5) meaning that $R\dot{W}HC$ hardly depends on CP-loading (Table 3.3). About five hrs into the experiments, the variation rate of $R\dot{W}HC$ decreases for all the systems (Figure 3.5). At the end of the experiments (24 hrs), we can see that $RWHC_f$ significantly increases with the CP-loading rate when the latter is lower than or equal to 0.8 g of CP per gram of PACP (Table 3.3). This can be explained by the increase in the amount of CP available for hydrate formation. However, a further increase in the CP-loading rate (to 1 g of CP per gram of PACP) causes $RWHC_f$ to drop. This decrease, due to the normalization of WHC, indicates a reduction in the ratio of the CP converted to hydrates to the CP

present in the system. The main possible reason for this behavior is given below. When preparing the PACP, soaked in 1 g of CP per gram of PACP, some of the CP added was not adsorbed by the PACP but remained as a free liquid phase. Note that free liquid CP was not observed at the lower CP-loading rates used, which suggests that the maximum loading rate of PACP is approximately 0.8 g of CP per gram of PACP. When the PACP prepared with 1 g of CP per gram of PACP are added to the NaCl solution, the excess CP is dispersed as droplets in the bulk phase by agitation (180 rpm). Because the agitation used is not very vigorous, the increase in the water/CP interface caused by the excess CP in the bulk phase is small compared to the interface between the CP adsorbed in the PACP and the water. The hydrate-formed amount therefore increases less significantly than the amount of CP added, and $RWHC_f$ decreases as a consequence.

The results obtained in this section show that the optimal rate for loading PACP with CP in order to obtain high hydrate formation kinetics and conversion is around 0.8 g of CP per gram of PACP.

3.3.2.3. Effect of the size of PACP on CP-hydrate formation

The $RWHC$ values obtained for the 400- μm PACP (Abac) were higher than those obtained with the 700- μm PACP (Gbac) at the beginning of the hydrate formation experiment, but then became lower after about five hrs (Figure 3.6). $RWHC$ is therefore higher in the case of the smaller particles and $RWHC_f$ is higher in the case of the larger ones (Table 3.4). Because these PACP have the same PSD and the same porosity, the difference in the $RWHC$ obtained can probably be explained by the difference in the external specific surface area of the particles. Smaller particles effectively have a larger external specific surface area, which provides a higher water/CP contact area and more nucleation sites. Consequently, a higher hydrate growth rate can be expected. However, $RWHC_f$ is higher when using 700- μm PACP, *i.e.* in the system with the PACP that offer the smaller water/CP contact area. A possible explanation might be that the slower initial hydrate growth rate ($RWHC$) obtained with these PACP delays or limits the formation of an impermeable hydrate crust on the CP layer at the PACP surface. The CP transfer is sustained, and a greater amount of hydrates forms. The trends observed here for the effect

of the PACP size on *RWHC* are consistent with those reported by Li *et al.* (2018) in their study on the promotion effect of graphite on CP-hydrate formation [13]. The authors observed that the water-to-hydrate conversion was initially faster and then increased more slowly for the smallest particles than for the largest ones.

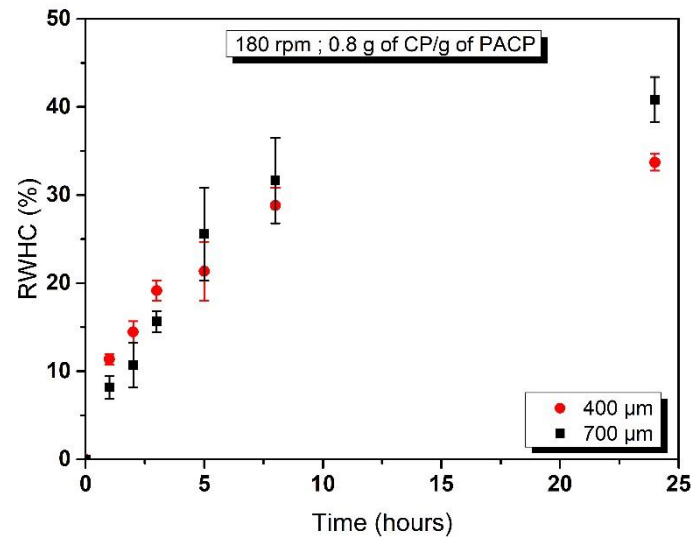


Figure 3. 6. Effect of PACP size (400 and 700 μm) on the relative water-to-hydrate conversion with 3.5 wt% NaCl. The PACP are loaded with 0.8 g of CP per gram of PACP. The stirring rate is 180 rpm.

Table 3. 4. Values of the relative water-to-hydrate conversion rate and the final relative water-to-hydrate conversion (at $t = 24$ hrs) for the different sizes of PACP (Gbac (700 μm) and Abac (400 μm)) loaded with 0.8 g of CP per gram of PACP. The initial conditions for these experiments correspond to starting point 1 (Figure 3.2). The stirring rate is 180 rpm.

Particle size (μm)	400 (Abac)	700 (Gbac)
RWHC (% /hr)	11.4 ± 0.6	8.2 ± 1.3
RWHC _f (%)	33.7 ± 0.9	40.9 ± 2.6

3.3.2.4. Effect of water salinity on CP-hydrate formation

In Figure 3.7 and Table 3.5, the results of the CP-hydrate formation experiments conducted with the 700- μm PACP (loaded with 0.8 g of CP per gram of PACP) at concentrations of 10 and 16 wt% NaCl (starting points 2 and 3 in Figure 3.2) are shown and compared with those obtained in experiments using 3.5 wt% NaCl (given in section 3.3.2.1).

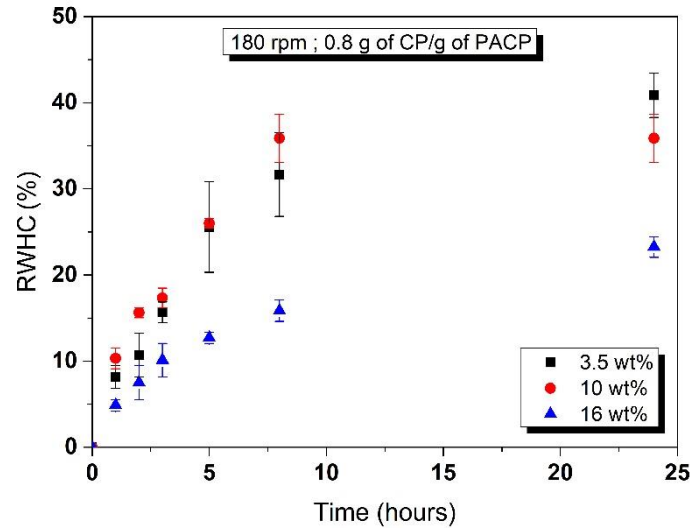


Figure 3. 7. Effect of water salinity on the relative water-to-hydrate conversion. The PACP (*Gbac*) are loaded with 0.8 g of CP per gram of PACP. The stirring rate is 180 rpm.

Table 3. 5. Values of the relative water-to-hydrate conversion rate and the final relative water-to-hydrate conversion (at $t = 24$ hrs) for the system with PACP (*Gbac* loaded with 0.8 g of CP per gram of PACP). The initial conditions for these experiments correspond to starting points 1, 2 and 3 (Figure 3.2). The stirring rate is 180 rpm.

NaCl concentration (wt%)	3.5	10	16
$R\dot{W}HC$ (% /hr)	8.2 ± 1.3	10.3 ± 1.2	4.9 ± 0.7
$RWHC_f$ (%)	40.9 ± 2.6	35.9 ± 2.8	23.3 ± 1.2

The $R\dot{W}HC$ points obtained at time t for NaCl concentrations of 3.5 and 10 wt% are very similar (Figure 3.7). Consequently, $R\dot{W}HC$ and $RWHC_f$ have roughly the same values for both concentrations (Table 3.5). This very interesting result suggests that the PACP soaked in CP “cancel” the kinetic inhibition effect of NaCl (demonstrated in section 3.3.1.2) for low to moderate salt concentrations. However, both $R\dot{W}HC$ and $RWHC_f$ significantly decrease in the system with 16 wt% NaCl. We saw in section 3.3.1.2 that the kinetic inhibition effect of NaCl on CP-hydrate formation is much stronger with 16 wt% NaCl than with 3.5 and 10 wt% NaCl. In fact, the hydrate growth rate (measured at the water/CP interface) with 16 wt% NaCl was 5 times lower than the growth rate with 10 wt% NaCl and 19 times lower than the one with 3.5 wt%. We can therefore infer that above a certain salinity, the presence of PACP is no longer able to “cancel” the kinetic inhibition effect of NaCl.

In their work on the desalination of PW using natural gas hydrates, Fakharian *et al.* (2017) [14] did not observe any hydrate formation in waters with a TDS higher than 160 g/L (*i.e.* 13.7 wt% of salts). In the present study, we succeeded in forming hydrates in water with 16 wt% NaCl. This illustrates another beneficial effect of using PACP soaked in CP.

3.4. Conclusion

This chapter demonstrates that using PACP soaked in CP significantly enhances hydrate formation kinetics and water-to-hydrate conversion. Therefore, PACP act both as a kinetic promoter and a CP source for hydrate formation. Combining PACP and stirring increases the formation kinetics but unexpectedly reduces the final water-to-hydrate conversion. The formation kinetics and water-to-hydrate conversion increase with the CP-loading rate of the PACP and then level off (or even slightly decrease) above a given loading rate (0.8 g CP per gram of PACP in our case). It was found that the smaller PACP size induces higher hydrate formation kinetics but a lower final conversion. It is interesting to note that the use of PACP soaked in CP makes it possible to overcome the kinetic inhibition effect of NaCl for salinities of up to 10 wt%. Above this value, PACP still enhance hydrate formation but both the formation kinetics and the conversion decrease (compared to lower salinities).

BGH process, which cleverly combines the use of a guest molecule (CP) forming hydrates at atmospheric pressure, and guest-soaked porous particles that promote hydrate formation and growth, appears as a promising desalination method. Nevertheless, the final water-to-hydrate conversion needs to be improved since more than one half of the CP adsorbed in the PACP is not converted to hydrates (Tables 3.2 and 3.5). Possible reasons for this behavior might be the formation of an impermeable hydrate layer on the PACP surface that blocks the contact between CP and water, and/or a fraction of CP tightly trapped in the pores of the PACP making it unavailable for hydrate formation. These points will be addressed in the next chapters.

3.5. References

- [1] Ho-Van S, Bouillot B, Douzet J, Babakhani SM, Herri JM. Experimental measurement and thermodynamic modeling of cyclopentane hydrates with NaCl, KCl, CaCl₂, or NaCl-KCl present. *AIChE J* **2018**; 64:2207–18. <https://doi.org/10.1002/aic.16067>
- [2] Kishimoto M, Iijima S, Ohmura R. Crystal Growth of Clathrate Hydrate at the Interface between Seawater and Hydrophobic-Guest Liquid: Effect of Elevated Salt Concentration. *Ind Eng Chem Res* **2012**; 51:5224–9. <https://doi.org/10.1021/ie202785z>.
- [3] Zyllyftari G, Lee JW, Morris JF. Salt effects on thermodynamic and rheological properties of hydrate forming emulsions. *Chemical Engineering Science* **2013**; 95:148–60. <https://doi.org/10.1016/j.ces.2013.02.056>.
- [4] Delroisse H, Torr  J-P, Dicharry C. Effect of a hydrophilic cationic surfactant on cyclopentane hydrate crystal growth at the water/cyclopentane interface. *Crystal Growth & Design* **2017**; 17:5098–107. <https://doi.org/10.1021/acs.cgd.7b00241>.
- [5] Tohidi B, Burgass RW, Danesh A, Østergaard KK, Todd AC. Improving the accuracy of gas hydrate dissociation point measurements. *Annals of the New York Academy of Sciences* **2000**; 912:924–31. <https://doi.org/10.1111/j.1749-6632.2000.tb06846.x>.
- [6] Cha J-H, Seol Y. Increasing Gas Hydrate Formation Temperature for Desalination of High Salinity Produced Water with Secondary Guests. *ACS Sustainable Chemistry & Engineering* **2013**; 1:1218–24. <https://doi.org/10.1021/sc400160u>.
- [7] Alkali Metal and Ammonium Chlorides in Water and Heavy Water (Binary Systems), Volume 47 - 1st Edition, <https://www.elsevier.com/books/alkali-metal-and-ammonium-chlorides-in-water-and-heavy-water-binary-systems/cohen-adad/978-0-08-023918-7>.
- [8] Corak D, Barth T, H iland S, Skodvin T, Larsen R, Skjetne T, Effect of subcooling and amount of hydrate former on formation of cyclopentane hydrates in brine. *Desalination* **2011**; 278:268–74. <https://doi.org/10.1016/j.desal.2011.05.035>.
- [9] Babu P, Yee D, Linga P, Palmer A, Khoo BC, Tan TS, et al, Morphology of Methane Hydrate Formation in Porous Media. *Energy Fuels* **2013**; 27:3364–72. <https://doi.org/10.1021/ef4004818>.
- [10] Siangsai A, Rangsunvigit P, Kitiyanan B, Kulprathipanja S, Linga P. Investigation on the roles of activated carbon particle sizes on methane hydrate formation and dissociation. *Chemical Engineering Science* **2015**; 126:383–9. <https://doi.org/10.1016/j.ces.2014.12.047>.
- [11] Siangsai A, Rangsunvigit P, Kitiyanan B, Kulprathipanja S. Improved methane hydrate formation rate using treated activated carbon and tetrahydrofuran. *Journal of chemical engineering of japan* **2014**; 47:352–7. <https://doi.org/10.1252/jcej.13we206>.

- [12] Yan L, Chen G, Pang W, Liu J, Experimental and modeling study on hydrate formation in wet activated carbon, *J. Phys. Chem. B.* **2005**; 109:6025–30. <https://doi.org/10.1021/jp045679y>.
- [13] Li F, Chen Z, Dong H, Shi C, Wang B, Yang L, et al, Promotion effect of graphite on cyclopentane hydrate based desalination. *Desalination* **2018**; 445:197–203. <https://doi.org/10.1016/j.desal.2018.08.011>.
- [14] Fakharian H, Ganji H, Naderifar A, Desalination of high salinity produced water using natural gas hydrate, *Journal of the Taiwan Institute of Chemical Engineers* **2017**; 72:157–62. <https://doi.org/10.1016/j.jtice.2017.01.025>.

Chapter 4. Experimental characterization of cyclopentane adsorption/desorption in porous activated carbon particles

4.1. Introduction

In the previous chapter, we have shown that the PACP used in BGH process act as both CP source and kinetic promoter of hydrate formation. However, the hydrate formed amount was found to be less than 50% of the possible maximum. This implied that at least one half of the CP initially present in the system could not be converted to hydrate. In light of these results, this chapter is dedicated to the investigation of CP loading/unloading on/from the PACP irrespective of hydrate formation. In the first part of this chapter, the virgin PACP are characterized (external morphology, SD, skeleton density, PV, SSA, PSD and micro-mesoporosity) and their CP capture/release determined through the measurement of adsorption and desorption isotherms at 30°C. The CP release from the PACP required more investigations which make the subject of the second part of this chapter. The influence of PACP pore size distribution (by using other PACP), CP-loading method (vapor-CP adsorption and liquid-CP imbibition) and purification temperature (from 30 up to 300°C) on the release of CP by the PACP was investigated. The results presented in this chapter have been reported in a publication cited as follows:

Rafik Mallek, Frédéric Plantier, Christophe Dicharry, Matthieu Jacob, Christelle Miqueu, Experimental characterization of cyclopentane adsorption/desorption in microporous activated carbons, Carbon Trends, Volume 2, 2021, 100021, ISSN 2667-0569, <https://doi.org/10.1016/j.cartre.2020.100021>.

4.2. Experimental Methods

4.2.1. PACP characterization

Gbac and Abac were observed with a light microscope (Nikon Eclipse LV100NDTM) in order to determine their external morphology. Their SD was determined by laser diffraction using a Malvern® Mastersizer 2000 granulometer. To do so, around 30 g of PACP were dispersed in around 400 g of pure water using the Hydro 2000 wet sample dispersion unit.

The four PACPs (Gbac, Abac, ChemA and Cycarb) were analyzed by gas porosimetry using the Autosorb IQTM from Quantachrome® with argon at 87 K as the testing probe. Before being used, around 0.1 g of each PACP were outgassed at 200°C during 12 hrs under secondary vacuum to remove any moisture and impurities within the pores of the materials. The PV, SSA and PSD were obtained with the QSDFT model (version : QSDFT -Ar-carbon equilibrium transition kernel at 87 K based on a slit-pore model) [1].

In order to investigate the release of CP by the PACP, the previous characteristics were again determined after a cycle of CP-adsorption/desorption followed by a prolonged evacuation under primary vacuum at 30°C for 24 hrs. It was assumed that argon solubility in the CP remaining inside the pores could be neglected in the experimental conditions of gas porosimetry. Several PACP of different PSD loaded through vapor-CP adsorption or liquid-CP imbibition were used. The comparison of the obtained results with the virgin-PACP characteristics allowed us to evaluate both the pore sizes responsible for CP-trapping and the effect of CP-loading method on this phenomenon. Furthermore, the temperature at which all the adsorbed CP is released was evaluated. In addition to the prolonged evacuation, Gbac was subjected to evacuation under secondary vacuum for two hrs at different temperatures: 30, 100, 200 and 300°C and characterized after each purification. For the sake of comparison, thermogravimetric analysis was also used. The sample was heated from 30 up to 300°C, at a heating rate of 2°C/min under a He flow of 100 mL/min.

4.2.2. Adsorption/desorption of CP

The adsorption/desorption isotherms of vapor CP in the four PACP were measured by gravimetry with a Rubotherm® magnetic suspension balance (MSB). Around 0.5 g of PACP were purified under primary vacuum at 200°C during 12 hrs before each adsorption isotherm measurement. The system was calibrated with helium to determine the volume and mass of the samples (see Appendix B-1). Vapor CP was generated through a 300 mL-tank half-filled with liquid CP and heated to 60°C. The tank was connected to the MSB through a set of 1/8 inch tubes, where a 0.025% full-scale accuracy pressure gauge is installed. The connection was also heated to 60°C to avoid condensation points. The use of micrometric valve made it possible to introduce very small amounts of vapor-CP in the adsorption chamber, thereby providing accurate measurements of the whole adsorption isotherm of CP. For the desorption isotherm measurement, the steam generator was replaced by a primary vacuum pump. The estimated uncertainties on the measured temperature, equilibrium pressure and adsorbed/desorbed CP amount are $\pm 1^\circ\text{C}$, ± 0.002 bar and $\pm 10^{-5}$ g of CP/g of PACP, respectively. It should be noted that the MSB was also used for the determination of the PACP skeleton densities (see Appendix B-2).

A coupled calorimetric-manometric device developed by Mouahid *et al.*(2010) [2] was used to measure the differential enthalpy of CP adsorption in Gbac and ChemA at 30°C. The apparatus consists of a Tian-Calvet Setaram C80 differential heat flow calorimeter coupled with a homemade manometric system operating isothermally. Around 0.5 g of PACP were purified, then introduced into the measurement cell and the device regulated at 30°C. The system was calibrated using helium in order to determine the adsorption and effective volumes, referred to as V_M and V_E , respectively (see Appendix B-3). After He evacuation, vapor CP, generated as described above, was injected through the microvalve into the dosing volume. The 1/16 valve located between the dosing volume and the measurement cell was opened (see Figure 2.10b in Chapter 2), thus bringing vapor CP into contact with the sample (PACP). The generated heat flow and pressure variation were recorded until equilibrium was reached. The operation was repeated and the obtained data treated (subtraction of the residual vacuum pressure from recorded equilibrium pressures; determination of the gas density at different pressures, calculation

of the adsorbed amount using mass balance, integration of the resulting thermal peaks) so that to determine the differential enthalpy of adsorption.

4.3. Results and discussion

4.3.1. Characterization of the virgin PACP

The microscopic observations showed that Gbac and Abac have a regular spherical shape (see Appendix B-5). Their SD are shown in Figure 4.1 and their mean particle diameters are given in Table 4.1. The PV and PSDs of the four PACP are shown in Figure 4.2. According to IUPAC nomenclature, they are essentially microporous with most of their PSD distributed below 2 nm. The PSD of Gbac and Abac are identical. Hence, the only difference between these two samples is their SD. The PSD of ChemA below 1.1 nm is nearly the same as those of Gbac and Abac, but it is more developed towards larger micropore sizes, especially with a third principal peak at 1.3 nm. Finally, the PSD of Cycarb is quite similar to that of ChemA in the micropore region, despite a lower micropore volume. However, small mesopores with a mean diameter of 30 nm are also present which made it possible to investigate the possibility of CP trapping at such pore sizes. The micro and meso-porosity of the PACP was deduced from their PV and skeleton densities. The main textural properties of the PACP are given in Table 4.1.

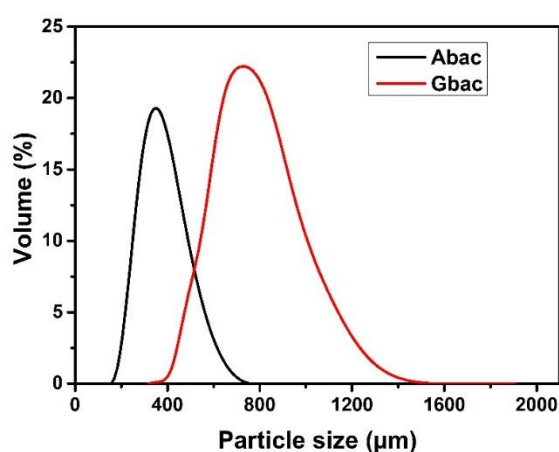
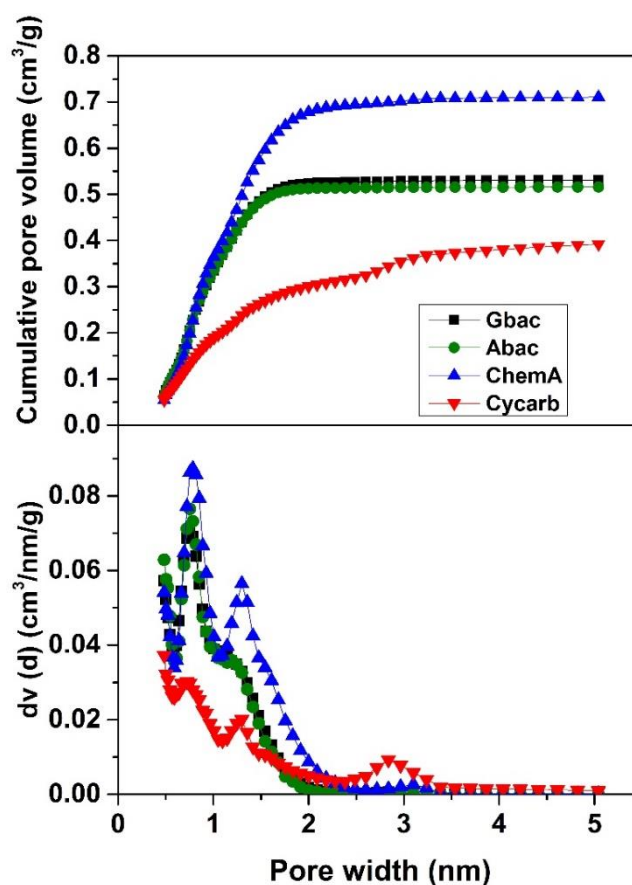


Figure 4. 1. Particle size distribution of Gbac and Abac.

Table 4. 1. Main characteristics of the four PACP used in this work.

	Gbac	Abac	ChemA	Cycarb
Mean particle diameter (μm)	687	326	< 177*	< 177*
Skeleton density	2.07	2.07	2.19	2.43
PV (cm^3/g)	0.536	0.519	0.718	0.466
Micro- and mesoporosity (%)	53	51.8	61.1	53.1
Principal pore sizes d (nm)	0.55 ; 0.79	0.55 ; 0.79	0.55 ; 0.79 ; 1.3	0.72 ; 1.30 ; 2.84
SSA (m^2/g)	1339	1317	1566	878
Proportion of micropore volume for $d < 0.7 \text{ nm}$ (%)	30	31	21	24
Proportion of micropore volume for $d < 1.1 \text{ nm}$ (%)	69	71	55	43

*ASTM definition

**Figure 4. 2.** (Top) pore volumes of the PACP measured by Ar adsorption at 87 K and obtained with a QSDFT model. (bottom) corresponding PSD.

4.3.2. Adsorption/desorption of CP in the PACP

4.3.2.1. Adsorption capacity and enthalpy

Adsorption capacities of the different PACP were evaluated through adsorption/desorption isotherms at 30°C (Figure 4.3). These isotherms present a typical shape of vapor adsorption in nanoporous activated carbons [3–6] with a sharp increase of adsorbed CP at low pressure corresponding to the filling of the micropores. For the highest pressures ($P/P_0 > 0.5$), the trend can be directly linked to the PSD. Indeed, for Gbac, Abac and ChemA, which are predominantly microporous, a saturation plateau is quickly obtained, while for Cycarb, which in addition contains mesopores, the quantity of adsorbed CP continues to increase, corresponding to the layering of CP in the mesoporosity. Besides these equilibrium properties, the order of magnitude of CP adsorption kinetics was evaluated at 10^{-2} g/min for the lowest pressures and 10^{-3} g/min for the highest pressures, which are typical values of vapor alkane adsorbed on activated carbons [7,8] (an example of MSB signal is given in Appendix B-4 in order to show how the CP-adsorption kinetics was evaluated).

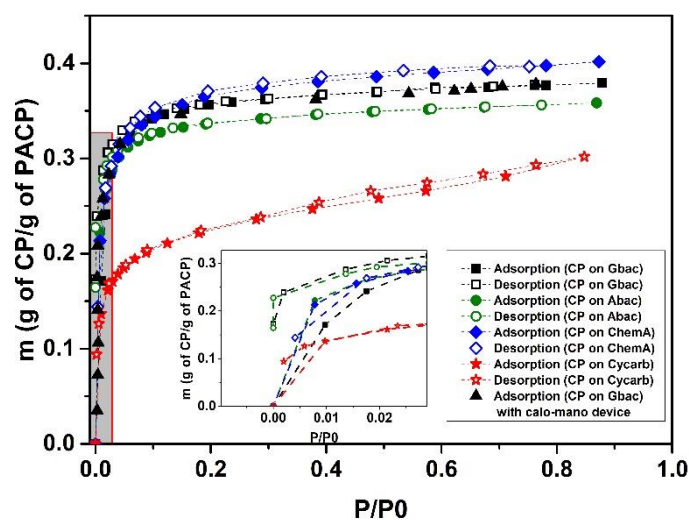


Figure 4. 3. Adsorption/desorption isotherms of CP at 30°C on the different AC measured by gravimetry. Filled marks: adsorption; empty marks: desorption. Squares: Gbac, circles: Abac, diamonds: ChemA, stars: Cycarb. Black triangles: Adsorption of CP on Gbac measured with manometric/calorimetric device. The inset is a zoom of the low-pressure measurements. Dotted lines are guide-for-the-eyes.

The adsorption capacities of the four PACP is directly correlated with their PV: the higher the PV, the higher the adsorption capacities. The comparison of CP adsorption isotherms of Gbac and Abac clearly evidences that their particle size does not significantly affect their CP adsorption capacities. This is obvious as the specific area of the external particle surface is negligible compared to that of the internal surface ($0.01 \text{ m}^2/\text{g}$ of PACP \ll $1300 \text{ m}^2/\text{g}$ of PACP). Adsorption capacities of the four samples are consistent with previous literature studies. Indeed, Lin and Lin (1999) [4] obtained an adsorption capacity of 0.14 g of CP / g of activated carbon at 25°C for an activated carbon with an average pore size of 2.4 nm and a SSA of $905 \text{ m}^2/\text{g}$. At the same temperature, Kabanova *et al.* (1988) [3] obtained 0.31 g of CP/ g of an activated carbon whose textural properties were not indicated.

The enthalpy of adsorption of CP on PACP was also measured for a PACP of each manufacturer (Gbac for Kureha and ChemA for Calgon) with a coupled calorimetric-manometric device. First, the good agreement between CP adsorption isotherms generated by both gravimetric and calo-manometric techniques shows the reliability of the obtained results (Figure 4.3). CP adsorption enthalpies are similar for both systems with an average value of 48 kJ/mol (Figure 4.4). The highest values ($> 55 \text{ kJ/mol}$) are obtained for the very first adsorbed amounts of CP (less than 0.0011 mole of CP/ g of PACP). These high energies are related to the interactions between CP molecules and active sites and to the overlapping of CP-walls interaction potentials in the narrowest pores of the PACP. As adsorbed amounts increase, adsorption enthalpies decrease to reach a constant value of 48 kJ/mol . This part of the curves corresponds to the filling of the micropores by CP and characterizes the fluid-fluid-solid interactions. The comparison with adsorption of linear alkanes on similar activated carbons – for which the adsorption enthalpy is around 30 kJ/mol of CP [9] – indicates a high affinity of CP towards activated carbon surface. For adsorbed amounts greater than 0.005 mole of CP/ g of activated carbon, the adsorption heat drops drastically to the value of the CP liquefaction enthalpy (approximately 29 kJ/mol [10]).

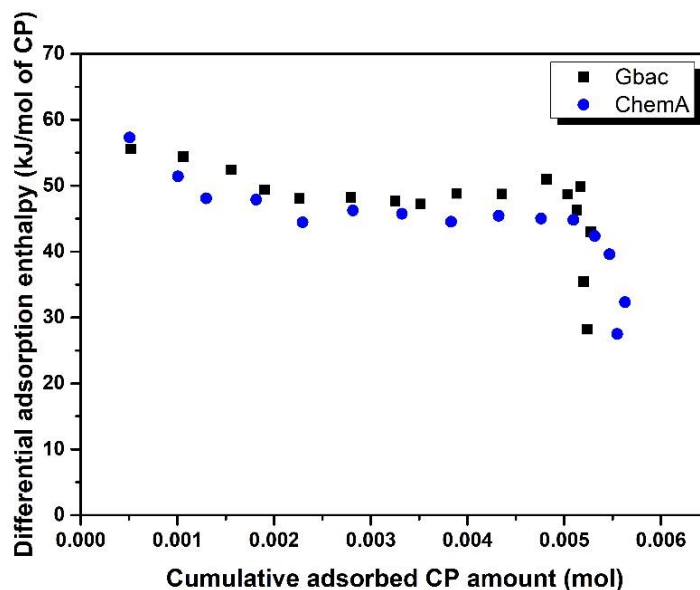


Figure 4. 4. Differential heat of adsorption of CP at 30°C on Gbac and ChemA measured with a manometric-calorimetric device.

4.3.2.2. Trapping capacity

As shown in Figure 4.3, CP adsorption isotherm on each PACP was followed by generation of desorption isotherm at the same temperature thanks to a primary vacuum pump and a micrometric valve. For the first desorption points, *i.e.* at the highest equilibrium pressures ($0.02 < P/P_0 < 0.9$), as can be seen in Figure 4.5a, equilibrium was reached after approximately 30 min and desorption kinetics was nearly 10^{-3} g of CP/min which is rapid and typical of vapor alkane desorption from PACP [9]. However, for the last desorption points, *i.e.* for the lowest equilibrium pressures ($P/P_0 < 0.02$), desorption kinetics became very low, around 10^{-6} g of CP/min (see an example in Figure 4.5b). Moreover, complete evacuation of CP was not reached even under prolonged evacuation during 24 hrs. The low kinetics of desorption at low pressures was a consequence of CP-molecules trapping in the smallest pores of the PACP. CP amounts trapped after 24 hrs of prolonged evacuation were 0.171, 0.174, 0.144 and 0.093 g of CP/g of PACP for Gbac, Abac, ChemA and Cycarb, respectively. This corresponds to proportions of trapped CP of approximately 45% for Gbac, 48% for Abac, 35% for ChemA, and 29% for Cycarb. Trapping of CP in activated carbons has been observed by few authors. Kabanova *et al.* (1988) [3] obtained 8% of trapped CP with prolonged evacuation at 25°C but under secondary vacuum. Lin and Lin (1999) [4] observed that trapping decreased with temperature. From the analysis of our experimental

results and literature data, we can assume that trapping is directly correlated with the PSD. First of all, the trapping rate is almost the same for both Gbac and Abac that have the same PSD. In addition, both ChemA and Cycarb which present PSDs more developed towards large pores have lower CP-trapping capacity.

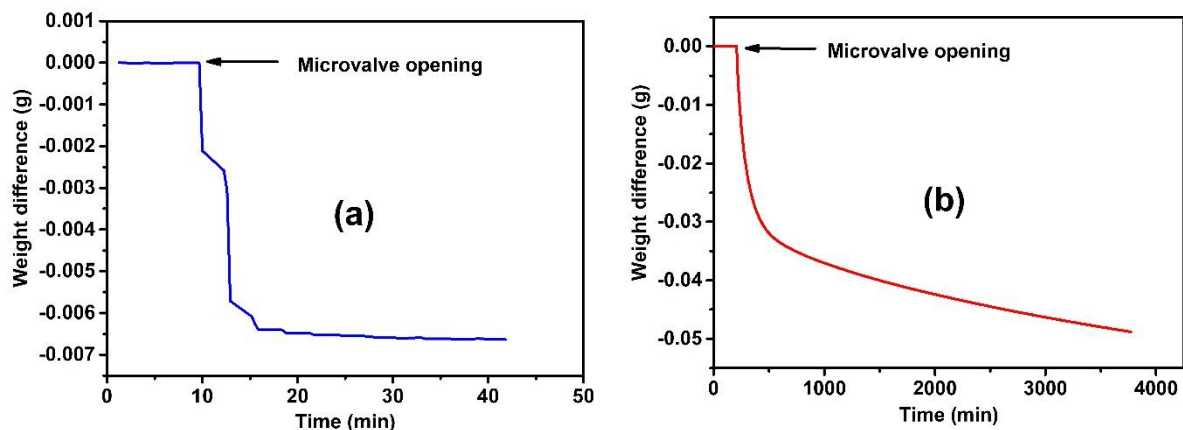


Figure 4.5. Weight of the sample as a function of time during desorption measured with the MSB. (left): typical of $P > 1$ kPa. (right): typical of $P < 1$ kPa with prolonged evacuation.

4.3.3. Characterization of the PACP after CP adsorption/desorption

4.3.3.1. Identification of the pore sizes responsible of CP trapping

The differences of PV and PSD before and after a cycle of CP adsorption/desorption and prolonged evacuation under primary vacuum during 24 hrs are depicted in Figure 4.6. All the accessible pore volumes have decreased, confirming that part of the porosity remains filled with CP. The analysis of the different PSD and the comparison between the samples make it possible to draw several conclusions. First, the quantity of mesopores (pore size > 2 nm) before and after CP adsorption/desorption is unchanged whatever the PACP, showing that CP can desorb from mesopores. On the opposite, almost all the ultra- and small micropores (pore size < 1.1 nm) have “disappeared” for each PACP showing that CP is still trapped in these pores due to the high interactions between the fluid and the solid in such small cavities, whatever the quantity and nature of active sites. For the intermediate micropores (1.1 nm $<$ pore size < 2 nm), the behavior is less general: for Gbac, Abac and Cycarb, CP totally desorbed as the PSD is recovered, while some micropores are still “clogged” for ChemA.

The analysis of the PACP before and after CP adsorption/desorption by gas porosimetry has given further insight into some already published studies that had observed the trapping of CP in activated carbons, without identifying the relevant porosity [3,4]. Moreover, our results are consistent with the trapping of other organic vapors evidenced and characterized by Lashaki and coworkers (2012-2020) [5,6,11,12].

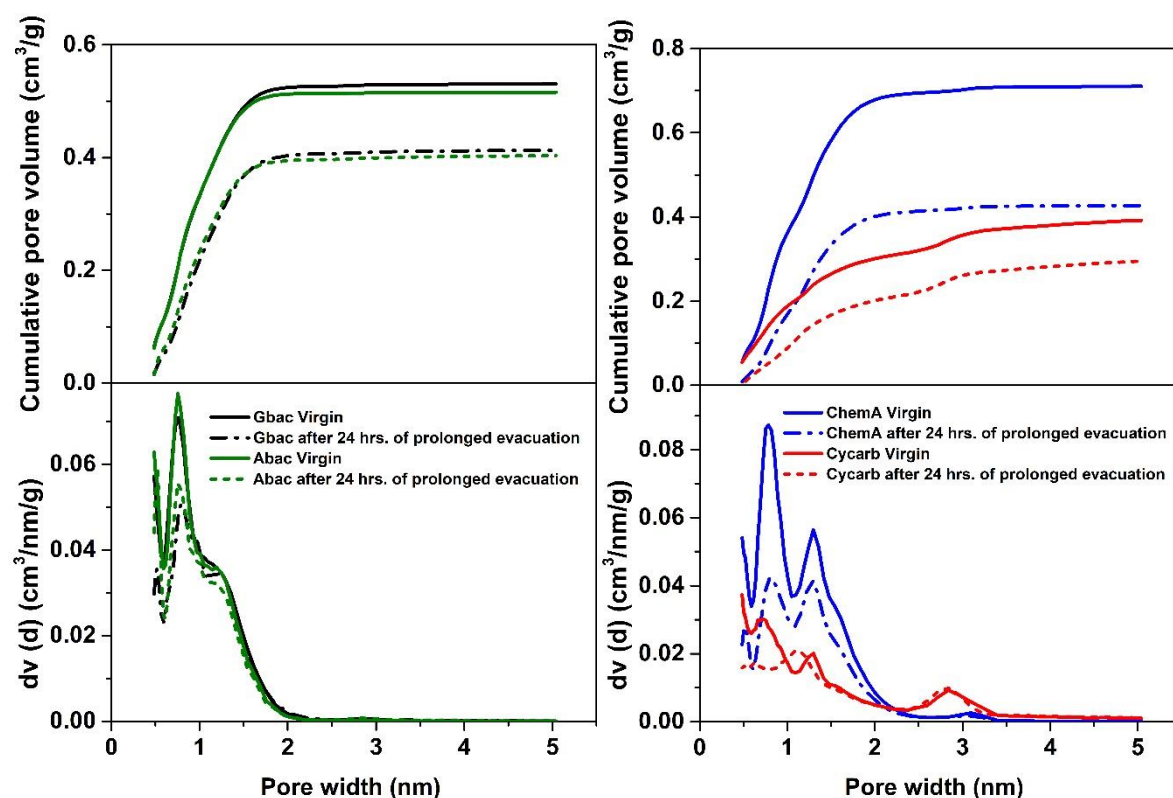


Figure 4. 6. (top) pore volumes of the PACP measured by Ar adsorption at 87 K and obtained with a QSDFT model. (bottom) corresponding pore size distributions. (left): Gbac and Abac. (right): ChemA and Cycarb. Solid lines: virgin PACP. Dashed lines: same PACP samples after CP adsorption/desorption. All the results are given per gram of PACP.

4.3.3.2. Influence of the CP loading process on CP trapping

The PV and PSD of Gbac and ChemA after vapor-CP adsorption and liquid-CP imbibition are compared in Figure 4.7.

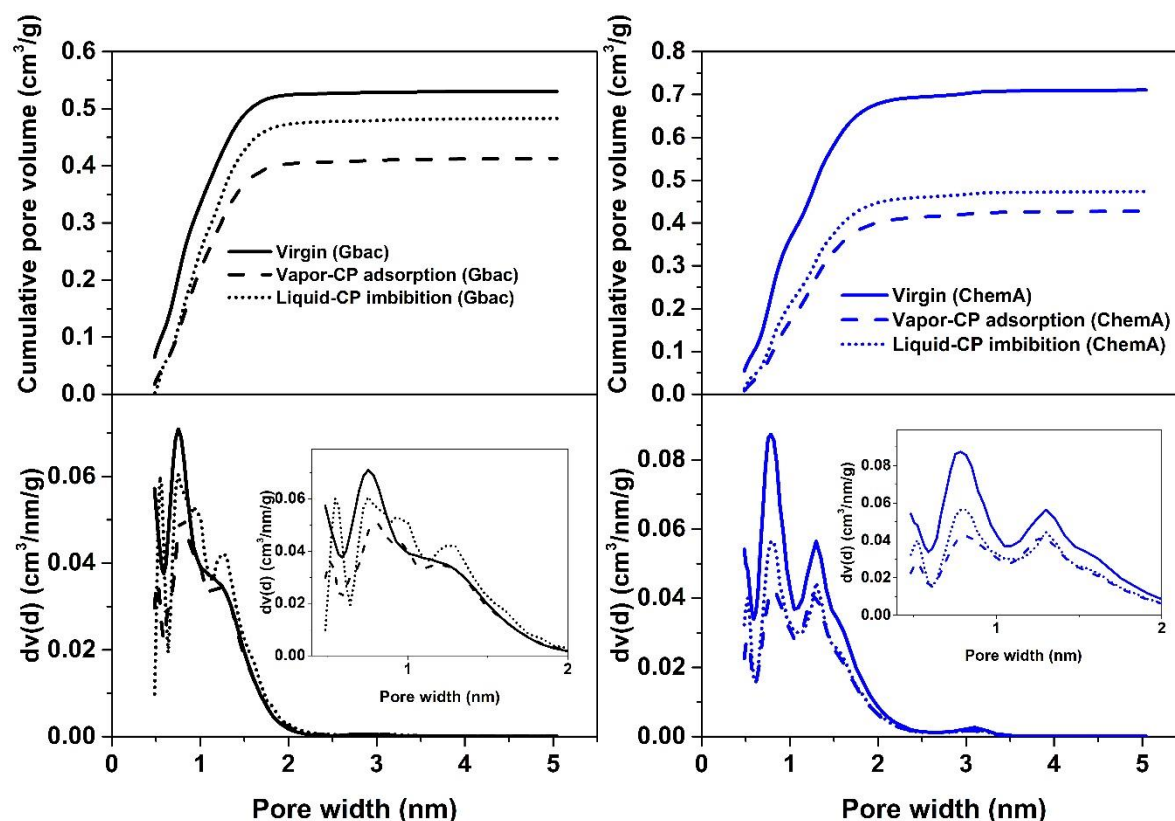


Figure 4. 7. Comparison of CP-loading method (vapor-CP adsorption vs. liquid-CP imbibition) in Gbac and ChemA. (top) Pore volumes of the PACP measured by Ar adsorption at 87 K and obtained with a QSDFT model. (bottom) corresponding pore size distributions. (left): Gbac. (right): ChemA. Solid lines: virgin PACP. Dashed lines: same samples after CP loading/evacuation.

The comparison of PV shows that more CP remains trapped in the case of the vapor-CP adsorption for both PACP, even if part of the CP introduced by liquid soaking cannot be evacuated. Hence, vapor-CP adsorption performs better in terms of adsorption capacity but liquid-CP soaking leads to a lower amount of CP trapped inside the micropores and thus to an enhanced recovery of CP after evacuation. The analysis of the PSD shows that CP-trapping depends on the CP-loading method only for pores lower than approximately 1.1 nm. This may be explained by the fact CP-loaded by liquid-CP soaking (occurring predominately by capillary imbibition) reaches less of these pore sizes compared to that loaded by vapor-CP adsorption (taking place by vapor diffusion).

4.3.3.3. Influence of purification temperature on CP trapping

In order to remove the trapped CP from the microporosity, other purification conditions were applied. Hence, after the 24 hrs of evacuation under primary vacuum, a second purification step consisting of evacuation under secondary vacuum and higher temperatures (up to 300°C) was applied to the materials. The impact of purification temperature on CP trapping is illustrated in Figure 4.8. “Clogged” pore volume decreases after purification under secondary vacuum at 100°C. This is mainly due to the use of secondary vacuum rather than a higher temperature. For higher purification temperatures, under secondary vacuum, the accessible micropore volume increases gradually with temperature. However, as better illustrated in Figure 4.9, a temperature of 277°C is needed to entirely remove CP from the micropores. This result has been confirmed with the mass loss measured with thermogravimetric analysis (TGA) on the same sample, also presented in Figure 4.9. Hence, the regeneration of narrow microporous PACP that adsorbed CP has a high energy cost, which agrees with the high enthalpies of adsorption in the narrowest pores (Figure 4.4).

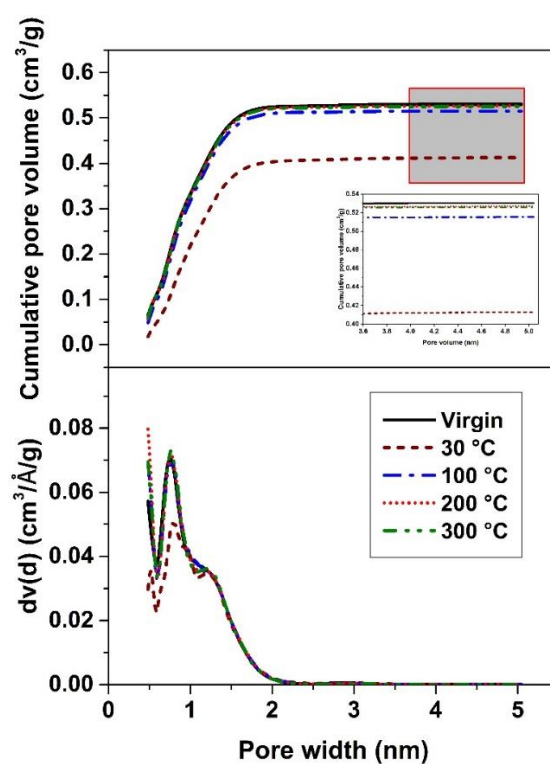


Figure 4. 8. Effect of purification temperature upon release of CP from microporosity of Gbac. (top) Pore volumes of the PACP measured by Ar adsorption at 87 K and obtained with a QSDFT model. (bottom) corresponding pore size distributions. Solid lines: virgin PACP. Dashed lines: same sample after CP adsorption/desorption with different purification temperatures.

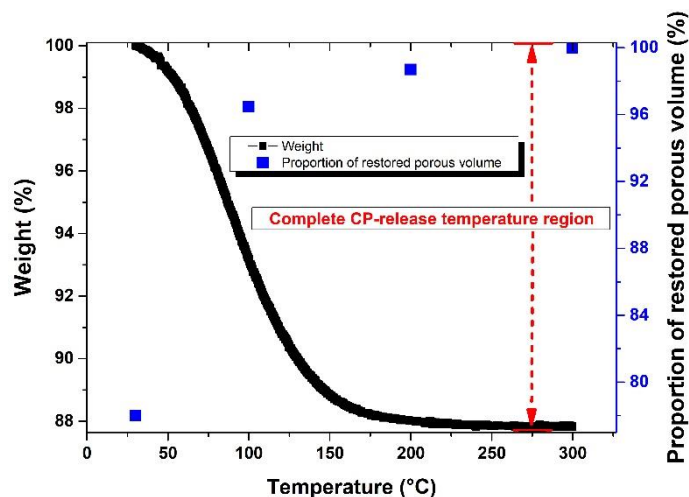


Figure 4. 9. Mass loss (measured by TGA) and proportion of pore volume recovered by secondary vacuum (measured by Ar porosimetry at 87 K) as a function of purification temperature.

4.4. Conclusion

This chapter has shown the evidence of hardly-reversible adsorption of cyclopentane in the four different PACP used in this work. The adsorption/desorption isotherm measurements revealed, on the one hand, that between 29 and 48 % of CP remains trapped in all the PACP even after prolonged evacuation under primary vacuum. On the other hand, calorimetric-manometric measurements have established that high-energy adsorption occurs at the lowest CP-loadings. Gas porosimetry before and after CP adsorption/desorption identified that the impact of particle size on CP-trapping is (as expected) negligible, whereas the impact of pore size distribution is significant. Pore sizes smaller than 1.1 nm were identified as responsible for hardly-reversible CP adsorption. The impact of CP-loading process (vapor adsorption vs. liquid imbibition) was also analyzed. It was shown that vapor-CP adsorption performs better in terms of adsorption capacity but liquid-CP soaking leads to lower CP trapping inside the micropores and thereby higher CP recovery after evacuation. Finally, coupling of TGA with gas porosimetry has shown that temperatures higher than 277°C are necessary to remove the CP trapped in the ultramicropores. The obtained results indicate that the low water-to-hydrate conversion in the presence of CP-loaded PACP, demonstrated in Chapter 3, can be related to CP trapping. According to the results obtained in this chapter, for enhancing hydrate formation, PACP with pores at least larger than 1.1 nm should be used.

4.5. References

- [1] Lowell S, Shields JE, Thomas MA, Thommes M, Characterization of Porous Solids and Powders: Surface Area, Pore Size and Density. Springer Netherlands, **2004**; <https://doi.org/10.1007/978-1-4020-2303-3>.
- [2] Mouahid A, Mise au point point d'un dispositif couple manométrique calorimétrique pour l'étude de l'adsorption de fluides supercritiques dans des milieux microporeux et mesoporeux. Physique[physics]. Université de Pau et des Pays de l'Adour, **2010**; Français. NNT: 10PAUU3020. tel-00573997.
- [3] Kabanova ON, Yakubov TS, Serpinski VV, Low-pressure hysteresis in the cyclopentane-activated charcoal system. Bulletin of the Academy of Sciences of the USSR, Division of Chemical Science **1988**; 37:1311–4. <https://doi.org/10.1007/BF00962728>.
- [4] Lin SH, Lin RC, Adsorption and Mass Transfer Characteristics of Pentane and Cyclopentane by Various Adsorbents. Environmental Technology **1999**; 20:11–9. <https://doi.org/10.1080/09593332008616787>.
- [5] Lashaki MJ, Fayaz M, Wang H (Helena), Hashisho Z, Philips JH, Anderson JE, Effect of adsorption and regeneration temperature on irreversible adsorption of organic vapors on beaded activated carbon. Environmental Science & Technology **2012**; 46:4083–90. <https://doi.org/10.1021/es3000195>.
- [6] Wang H, Jahandar Lashaki M, Fayaz M, Hashisho Z, Philips JH, Anderson JE, Adsorption and desorption of mixtures of organic vapors on beaded activated Carbon. Environmental Science & Technology **2012**; 46:8341–50. <https://doi.org/10.1021/es3013062>.
- [7] Yang X, Yi H, Tang X, Zhao S, Yang Z, Ma Y, Behaviors and kinetics of toluene adsorption-desorption on activated carbons with varying pore structure. Journal of Environmental Sciences **2018**; 67:104–14.
- [8] Do DD. Adsorption Analysis: Equilibria and Kinetics. vol. 2. Imperial College Press; **1998**. <https://doi.org/10.1142/9781860943829>.
- [9] Pino D, Plantier F, Bessières D, Adsorption of Alkanes in the Dense Vapor Phase on a Microporous Activated Carbon. Journal of Chemical & Engineering Data **2017**; 62:1716–24. <https://doi.org/10.1021/acs.jced.7b00175>.
- [10] <http://webbook.nist.gov/chemistry/fluid/>
- [11] Lashaki MJ, Hashisho Z, Phillips JH, Crompton D, Anderson JE, Nichols M, Mechanisms of heel buildup during cyclic adsorption-desorption of volatile organic compounds in a full-scale adsorber-desorber. Chemical Engineering Journal **2020**; 400:124937. <https://doi.org/10.1016/j.cej.2020.124937>.

- [12] Lashaki MJ, Atkinson JD, Hashisho Z, Phillips JH, Anderson JE, Nichols M, The role of beaded activated carbon's pore size distribution on heel formation during cyclic adsorption/desorption of organic vapors. *Journal of Hazardous Materials* **2016**; 315:42–51. <https://doi.org/10.1016/j.jhazmat.2016.04.071>.

Chapter 5. Investigation on hydrate formation from cyclopentane-loaded porous activated carbon particles

5.1. Introduction

It was shown previously that the PSD of the PACP is the main parameter that controls the CP-trapping and that PACP with large pore sizes are recommended for enhancing hydrate formation. The present chapter exploits these results in order to elucidate the mechanisms governing hydrate formation from CP-loaded PACP immersed in pure water at a subcooling of 6°C. Hydrate formation was investigated here through micro-DSC experiments. In a first part, the PACP were saturated with CP and subjected to several hydrate formation/dissociation cycles. CP conversion rates were quantified, throughout the cycles, by integrating the hydrate dissociation thermal peaks. In a second part, PACP were oversaturated with CP and only one cycle of hydrate formation/dissociation was imposed to the system in order to mimic the conditions of the batch reactor experiments (see Chapter 3). Microscopic observation of hydrate formation was also performed. The conducted investigations aim at proposing a formation mechanism for CP hydrates from CP-loaded PACP.

The results presented in this chapter are reported in a publication under revision cited as follows:

Rafik Mallek, Christelle Miqueu, Matthieu Jacob, Christophe Dicharry, Investigation on hydrate formation from cyclopentane-loaded porous activated carbon particles, submitted to Chemical Engineering Sciences in October 2021.

5.2. Experimental methods

5.2.1. Characterization of PACP and determination of adsorption capacities

To perform the gas porosimetry measurements, the PACP were purified at 200 °C under secondary vacuum for 12 hrs. Argon adsorption-desorption isotherms were generated at 87 K and interpreted with the help of the Quenched Solid Density Functional Theory (QSDFT) in order to determine the cumulative PV and the corresponding PSD. This technique provides a reliable evaluation of pore sizes from 0.5 to 30 nm. Mercury intrusion porosimetry (MIP), whose practical range is 10 nm to 300 μm, was used to complete the pore volumes information in the macroporous region. After being purified at 200 °C under primary vacuum for 12 hrs, 0.2 to 0.9 g of each type of PACP (depending on the PACP density and the penetrometer capacity) were loaded into a suitable powder penetrometer. The interpretation of the mercury intrusion volume curve using the Washburn model and considering the compressibility of the PACP and mercury at the highest pressures, served to determine the cumulative PV. The Mayer-Stowe method was used in the low-pressure range to determine the particle size distribution and compare it to granulometry measurements for one sample.

To perform CP-adsorption capacity measurements, the PACP were purified at 200 °C for 12 hrs under primary vacuum. Using a glass funnel, the hot purified sample was directly transferred to a small closable flask (5-mL capacity), which was then weighed and introduced into the CP-adsorption chamber. The PACP were not in contact with liquid CP but with vapor CP (see Appendix C-1). The CP-adsorption chamber was placed in the incubator at (1 ± 0.5) °C. After 48 hrs of adsorption, the flask was weighed again and the CP-adsorption capacity of the PACP was determined. The experiment was repeated 3 times to check the results' reproducibility and define the associated uncertainties. The validity of this method was checked by determining the adsorption capacity of BGX at 30°C and comparing the result obtained with the one deduced from the CP-adsorption isotherm (see Appendix C-2 and C-3) generated using the gravimetric technique.

5.2.2. CP-Hydrate formation from CP-saturated PACP

In order to investigate the effect of the PSD of the PACP on hydrate formation, experiments were performed using the three types of PACP saturated with CP. Figure 5.1 shows a CP-saturated PACP immersed in water before hydrate formation. In this case, PACP were first purified at 200 °C for 12 hrs under primary vacuum. 25 mg of the hot PACP were then transferred to the measurement cell of the μ DSC7 evo using a glass funnel. The cell was introduced into the CP-adsorption chamber at 1 °C for 48 hrs in order to saturate the PACP with CP. Afterwards, 200 mg of deionized water were added into the cell, which was then closed and placed in the μ DSC. A temperature profile, consisting of two main stages, was imposed on the system in order to form and dissociate hydrates (Figure 5.2). In the first stage, hydrate crystallization was initiated through ice formation. The system was cooled to – 20 °C (to form ice) and then heated to 1 °C (to melt ice and form the hydrates) and maintained at this temperature for 24 hrs. Afterwards, the hydrates formed were dissociated at a heating rate of 0.05 °C/min. The second stage consisted of 10 cycles of fast hydrate formation and decomposition followed by a slow decomposition cycle (heating rate of 0.05 °C/min). This second stage was repeated 5 times. The dissociation temperature(s) and amounts of energy released were determined after each slow hydrate dissociation cycle.

Dissociation temperatures were obtained by applying the tangent method (standard ISO 11357-3) and the amount of energy released by integrating the hydrate dissociation peaks. The latter were converted through CP-hydrate dissociation enthalpy (115.4 kJ/mole of CP [1]) to a CP-to-hydrate mass and subsequently to a CP-conversion rate, defined as follows:

$$CP_conversion\ rate\ (\%) = \frac{CP_to_hydrate\ mass * 100}{Initial\ CP_mass} \quad (Eq. 5.1)$$

The uncertainties as regards energies were calculated as the sum of the deviations determined based on the two experiments performed (deviation from the average value) and calibration control (through the dissociation of ice formed from deionized water (see Appendix C-4)).

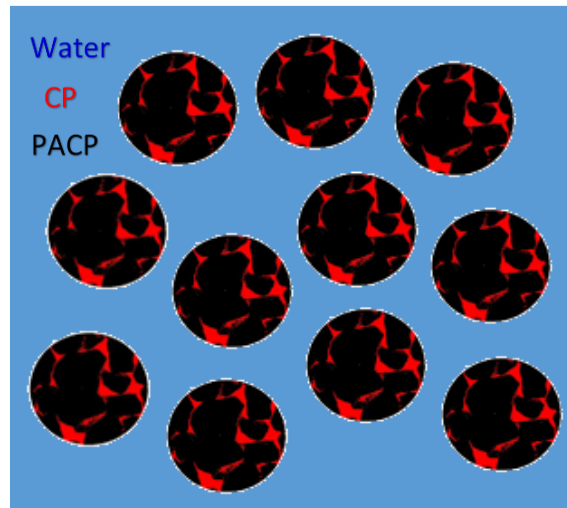


Figure 5. 1. CP-saturated PACP immersed in water.

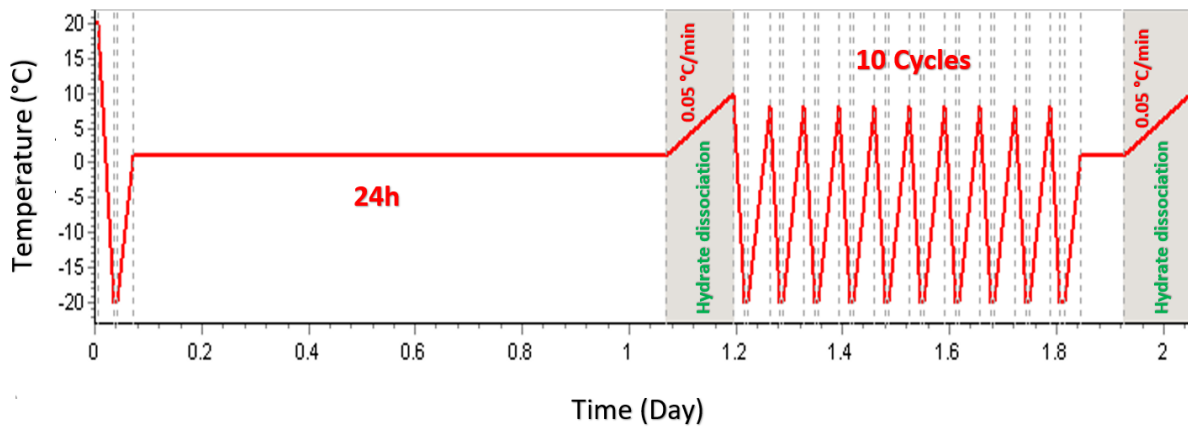


Figure 5. 2. Temperature profile imposed for hydrate formation and dissociation from CP-saturated PACP.

5.2.3. CP-Hydrate formation from CP-oversaturated PACP

The objective of this section is to investigate the amounts of CP-to-hydrates obtained in CP-oversaturated PACP water systems (Figure 5.3). To this end, two types of PACP (Gbac and BGX) were overloaded with the same excess amount of CP (excess mass compared to CP mass at saturation). The latter, below referred to as surface CP, entirely covered the external surface of the PACP. In other words, no free liquid CP appeared while the PACP were being loaded. The initial surface-CP mass was calculated as the difference between the total loaded CP mass and the CP mass at saturation (equation 5.2).

$$\text{Initial surface_CP mass} = \text{Loaded_CP mass} - \text{CP mass at saturation} \quad (\text{Eq. 5.2})$$

For this purpose, 25 mg of the hot purified PACP (under primary vacuum at 200°C for 12 hrs) were transferred to the μ DSC measurement cell. The PACP were directly soaked with liquid CP so as to be oversaturated at a rate of 0.4 g excess CP (CP above saturation) / g PACP. Afterwards, 200 mg of deionized water were added to the cell, which was then closed and introduced into the μ DSC. Hydrates were formed following the first stage of the temperature profile (Figure 5.2).

The hydrate dissociation peaks were integrated in order to obtain the CP-to-hydrate mass and consequently the CP- conversion rate (see Equation 5.1). The surface-CP-to-hydrate mass was determined by assuming that the surface CP is converted before the pore CP. From there, the surface-CP conversion rate was calculated using equation 5.3:

$$\text{Surface_CP conversion rate (\%)} = \frac{\text{Surface_CP to hydrate mass} * 100}{\text{Initial surface_CP mass}} \quad (\text{Eq. 5.3})$$

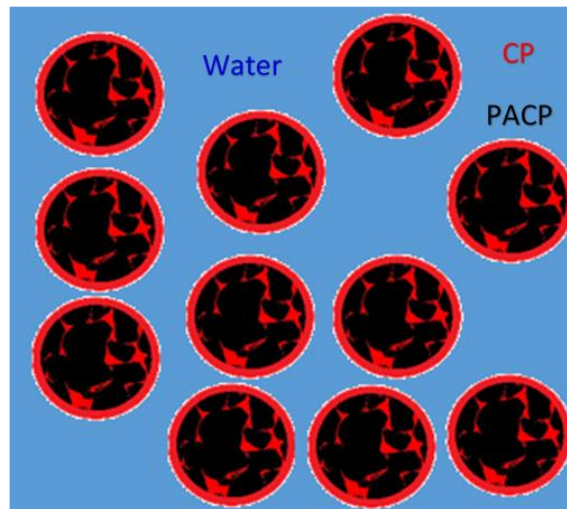


Figure 5. 3. CP-oversaturated PACP immersed in water.

Note that these experiments mimic the hydrate formation experiments conducted in batch reactors where CP hydrates were formed from CP-oversaturated Gbac (0.8 g CP/g PACP) in quiescent conditions (without stirring) for 24 hrs (see section 3.2.2.1 in Chapter 3).

5.2.4. Visualization of CP-hydrate crystallization from CP-loaded PACP

CP-loaded PACP (Gbac and BGX) and CP-hydrate crystallization were observed using the binocular magnifier. To do so, the glass cell was filled with 25 ml of deionized water. Alongside this, 200 mg of each type of PACP were saturated or oversaturated with CP at the same rates as previously (0.8 g CP/g Gbac and 1.36 g CP/g BGX) and then introduced into the glass cell. The system was cooled down to 1°C so as to achieve a subcooling of 6 °C. CP-hydrate crystallization was triggered by seeding the system with a few CP-hydrate crystals, prepared beforehand. The cell was tightly sealed in order to prevent CP evaporation. The binocular magnifier was focused on CP-loaded PACP and snapshots were acquired at a regular timestep. During the experiment, the seal top was exposed to an air flow in order to prevent water condensation and subsequently, blurry images.

5.3. Results and Discussion

5.3.1. Characterization of PACP and determination of adsorption capacities

The microporosity of the three types of PACP was analyzed using the adsorption isotherm of argon at 87 K. The cumulative PV and PSD of the three samples, obtained with the QSDFT (slit pore geometry), are shown in Figure 5.4. As can be observed, BGX (green curve) has a much more developed PSD in the largest micropore and small mesopore ranges than the other two PACP. Indeed, this criterion served as a basis for the selection of BGX in this study, considering the conclusions of Chapter 4 indicating that CP remains trapped in the ultramicroporosity and small supermicroporosity regions after adsorption.

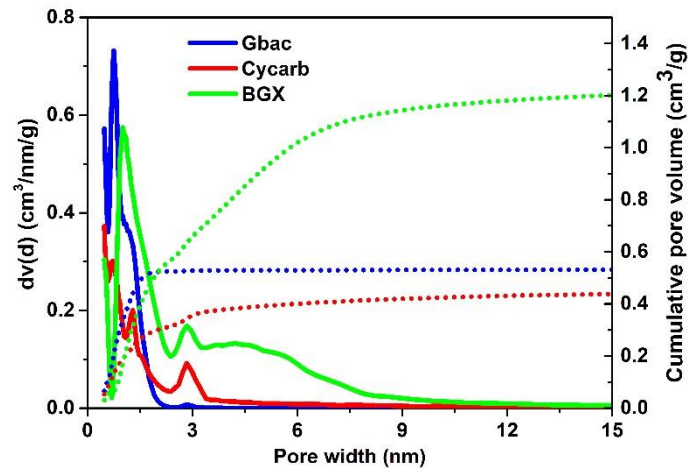


Figure 5. 4. PSD and cumulative pore volumes of PACP obtained with QSDFT Ar at 87 K

To go beyond the micropore volumes and PSD obtained using Argon porosimetry, the meso- and macropore volumes were quantified using MIP. A typical mercury intrusion curve is shown as a function of pressure in Figure 5.5 for a sample of Gbac. Three stages can be distinguished in the intrusion process: first, mercury invades the voids between the particles which causes a steep increase in the volume of intruded mercury at the lowest pressures ($P < 0.02$ MPa approx.). It is followed by a region in which the volume of intruded mercury continues to increase but to a lesser extent ($0.02 < P < 3$ MPa approx.); this corresponds essentially to the surrounding of the particles by the mercury and possibly its intrusion inside the microcracks. Finally, mercury penetrates the intraparticle porosity. It is the latter part of the intrusion curve that allowed us to deduce the macro and mesoporous volume of the samples.

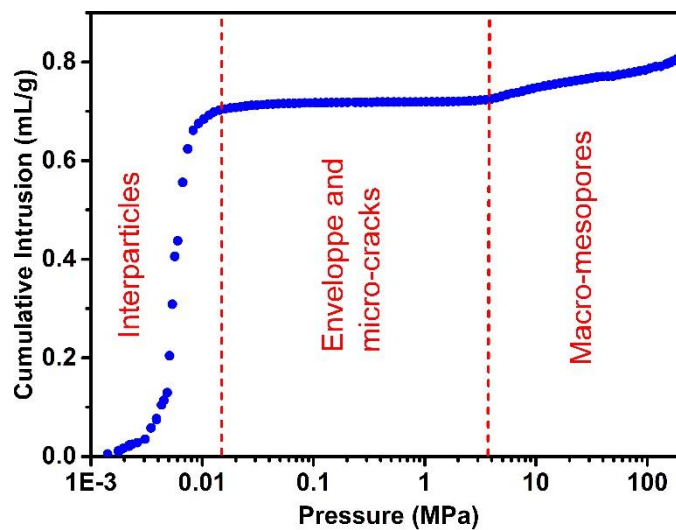


Figure 5. 5. Mercury intrusion curve (cumulative intrusion volume as a function of intrusion pressure) for Gbac.

The intruded mercury volume (or cumulative PV) obtained by considering compressibility at the highest pressures is plotted in Figure 5.6 as a function of pore size. The Washburn equation was used to link pressure and pore size. A contact angle of 145° - a typical value for activated carbons [2] - was used for both Cycarb and BGX samples. For Gbac, a highly spherical activated carbon made from petroleum pitch, a mercury contact-angle value of 130° was obtained by fitting the particle diameter distribution obtained using the Mayer-Stowe method with the SD measured in Chapter 4 (section 4.3.1). The corresponding macro- and mesoporous volumes are given in Table 5.1 together with the CP-adsorption capacities of the PACP at 1°C . The adsorption capacities measured are in line with the PSD obtained. Indeed, BGX, which has the highest adsorption capacity, presents both a greater micropore fraction, where most of the CP adsorption takes place, and larger pores (meso- and macropores) than Cycarb. On the other hand, it has almost the same micropore fraction as Gbac, but a greater fraction of large pores. In addition, the adsorption capacity of BGX is greater than what was determined at 30°C (see Table 5.1 and Appendix C-3), which makes sense since adsorption capacity decreases with temperature.

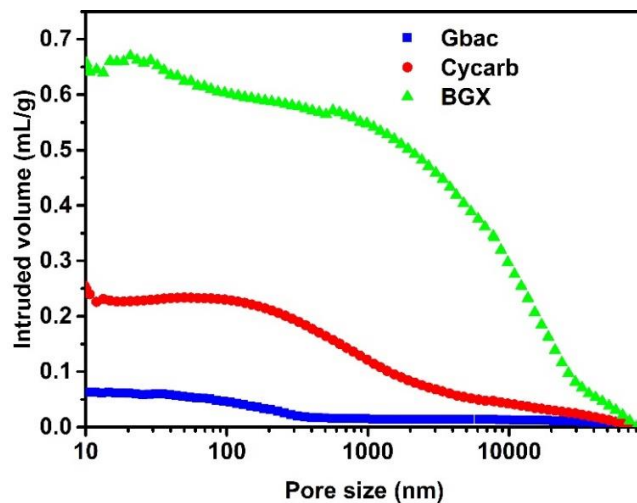


Figure 5. 6. Mercury intruded volume as a function of pore size for the three PACP.

Table 5. 1. Characteristics of the PACP used.

	Gbac	Cycarb	BGX
Adsorption capacity (g of CP/g of PACP)	0.40 ± 0.01	0.40 ± 0.03	0.96 ± 0.02
V_{macro} (cm ³ /g)	0.05	0.25	0.65
V_{meso} (cm ³ /g)	0.01	0.01	0.05
V_{micro} (cm ³ /g)	0.54	0.47	0.72

5.3.2. CP-Hydrate formation from of CP-saturated PACP

CP-hydrate formation/dissociation cycles in the presence of CP-saturated PACP resulted in several endothermic peaks. By analyzing them, it was possible to determine both the hydrate dissociation temperatures and dissociation energies (Figure 5.7). The latter were then used to calculate the CP-to-hydrate masses (Figure 5.8). In the hydrate dissociation stages, both a main peak around the CP-hydrate equilibrium temperature ($T \approx 7.1^\circ\text{C}$) and few small peaks at lower temperatures (between 4.8°C and 7.1°C) can be observed. Since gas hydrates confined in small pores are known to dissociate at lower temperatures than bulk hydrates [3], the shifts observed in the CP-hydrate equilibrium temperature prove that a fraction of the CP hydrates was formed inside the PACP pores, which indicates that water molecules were able to enter the PACP pores to form hydrates with the CP. For the three types of PACP, the CP-to-hydrate mass increased until reaching a maximum value after a given number of cycles depending on the PACP used (40, 30 and 10, for Gbac, Cycarb and BGX respectively).

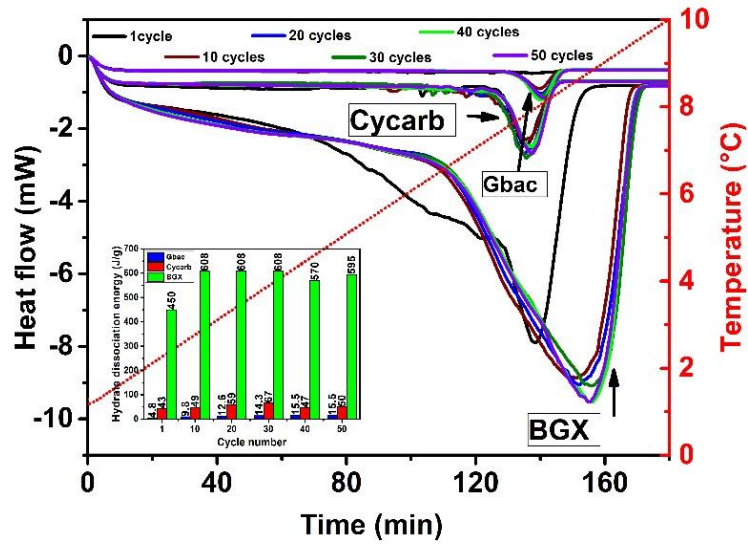


Figure 5. 7. Hydrate dissociation peaks of CP hydrates formed from CP-saturated PACP.

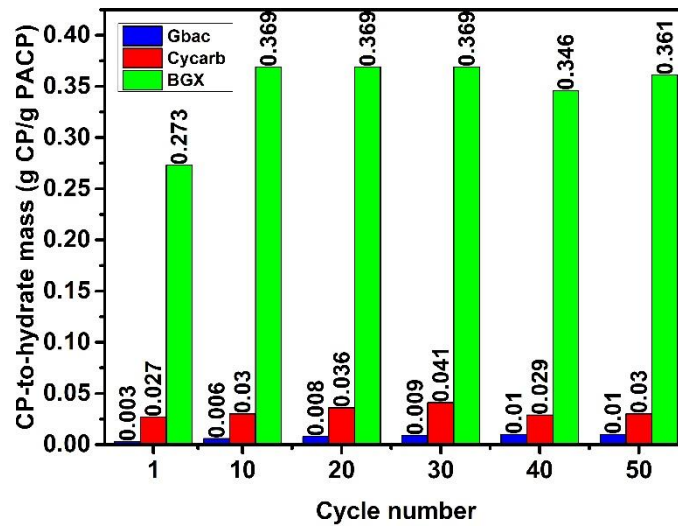


Figure 5. 8. CP-to-hydrate masses throughout the cycles.

Figure 5.8 shows that CP in pores is converted progressively and suggests that the conversion occurred at different kinetics. The maximum CP-conversion rates shown in Table 5.2 imply that the PACP trapped a high percentage of the CP initially loaded (up to 97% in the case of Gbac), meaning that only a few percent of CP (3% in the case of Gbac) was available for hydrate formation. The large fraction of trapped CP can be explained by a combination of: i) the fluid-solid and fluid-fluid interactions within the pores, and ii) the low CP-desorption driving force (applied by hydrate crystallization). This result is consistent with the results presented in Chapter 4 where a smaller fraction of trapped CP was obtained

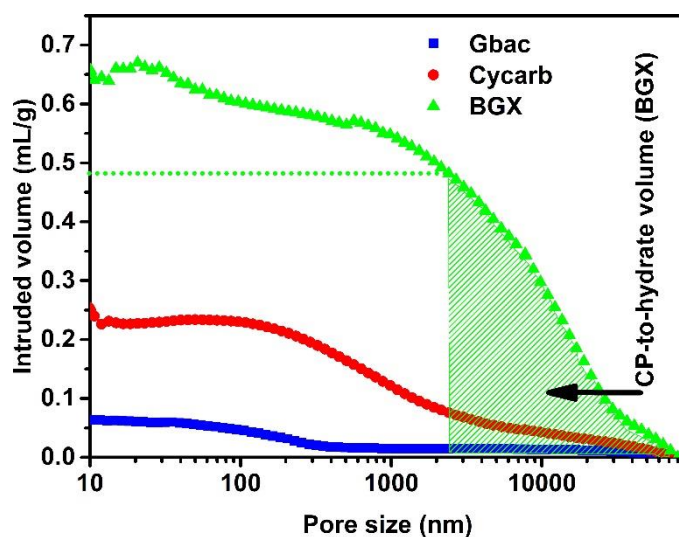
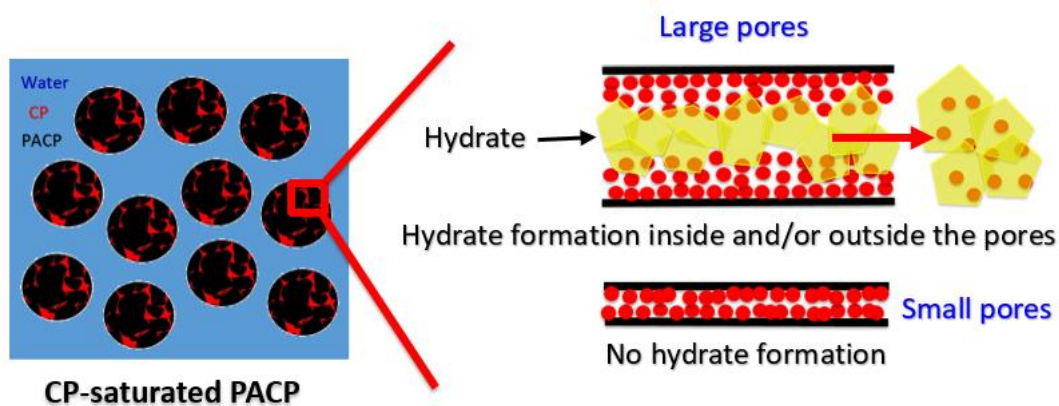
for Gbac (45%) using primary vacuum as the CP-desorption driving force. It also explains the relatively small quantity of hydrates formed obtained in Chapter 3. The maximum CP-conversion rate depends on the type of PACP used (Table 5.2) and seems to be related to their PSD. Indeed, BGX, which has the largest pores and meso- and macropore volumes among the PACP used (Table 5.1) produced the highest CP-conversion rate, whereas Gbac which has the smallest pores and hardly any meso- and macropores gave the lowest CP-conversion rate. One can see that the variation in the maximum CP conversion rate of two different types of PACP is roughly proportional to the ratio of their macroporous volumes. As an example, the latter for BGX and Gbac is 13 (= 0.65:0.05) and the CP conversion rate of BGX is 12.7 (= 38:3) times greater than that of Gbac.

Greater pore sizes mean reduced confinement, and CP is therefore released more easily. Both the trapping of CP and the effect of pore size (or PSD) on the CP-conversion rate suggest the existence of a threshold pore size above which CP is available for conversion to hydrates. Assuming that CP is converted/released more easily from larger pores and that all the CP contained in the pores larger than the threshold size is converted, the conversion rate could be roughly determined by projecting the maximum CP-to-hydrate volumes on the mercury intruded volume curve (Figure 5.9). As an example, the threshold size was found to be of the order of a micrometer for BGX. Note that for the two other types of PACP, it was impossible to estimate the threshold size due to both the small pore volumes and the corresponding uncertainties in the macro- and mesoporous ranges.

In light of the obtained results, a mechanism of hydrate formation in such CP-saturated PACP is proposed in Figure 5.10. CP remains trapped in small pores where high confinement is exerted (high interactions), whereas CP in large pores is available for hydrate formation. In this case, hydrate can form outside and/or inside the pores.

Table 5. 2. Maximum CP-conversion rates.

	Gbac	Cycarb	BGX
CP-to-hydrate mass after 1 cycle (g CP/g PACP)	0.003 ± 0.001	0.027 ± 0.006	0.27 ± 0.03
CP-to-hydrate conversion rate after 1 cycle (%)	1.0 ± 0.3	7 ± 2	28 ± 4
Maximum CP-to-hydrate mass (g CP/g PACP)	0.010 ± 0.002	0.04 ± 0.01	0.37 ± 0.05
Maximum CP-to-hydrate volume (cm ³ CP/g PACP)	0.012 ± 0.002	0.06 ± 0.01	0.49 ± 0.06
Maximum CP conversion rate (%)	3.0 ± 0.6	11 ± 4	38 ± 5

**Figure 5. 9.** Determination of the threshold pore size of pores releasing CP.**Figure 5. 10.** Proposed mechanism governing hydrate formation from CP-saturated PACP.

5.3.3. CP-Hydrate formation from CP-oversaturated PACP

Even though the CP-conversion rate, and therefore the quantity of hydrates, was enhanced using PACP with PSD more developed in the meso- and microporous regions, it still remained relatively low ($< 28 \pm 4$ % after 1 cycle and $< 38 \pm 5$ % after 50 cycles (Table 5.2)). Consequently, the PACP were oversaturated with CP in an attempt to enhance the CP-conversion rate. Figure 5.11 represents the dissociation peaks of CP-hydrates formed in the presence of oversaturated Gbac and BGX. Analysis reveals an enhancement in CP-conversion rates compared to those achieved with the CP-saturated PACP system after the same number of hydrate formation/dissociation cycles, namely after one cycle (from 1.0 ± 0.3 % to 44 ± 6 % for Gbac and from 28 ± 4 % to 45 ± 6 % for BGX (see the second line in Table 5.2 and the third line in Table 5.3). This is due to the high conversion rate of surface CP (88 ± 12 % for Gbac and 100 ± 23 % for BGX) (Table 5.3). A reasonable explanation is that the surface CP is in direct contact with water and thus readily available for hydrate formation.

As mentioned in section 5.2.3, the experiment involving CP-oversaturated Gbac mimics the hydrate formation experiments in the batch-chemical reactors used in Chapter 3 (see sections 3.2.2.1 and 3.3.2.1 for the case of Gbac loaded with 0.8 g CP/g PACP without stirring) where we found a CP-conversion rate of 47.4%. Interestingly enough, this rate is close to the one found here, *i.e.* 44% (see Table 5.3) even though the system volume differs by more than three orders of magnitude (250 μ L and 900 mL in the present and previous experiment respectively). This suggests that the system volume has no significant effect on hydrate formation. One can infer that the results obtained at laboratory scale might be reproducible at an industrial scale.

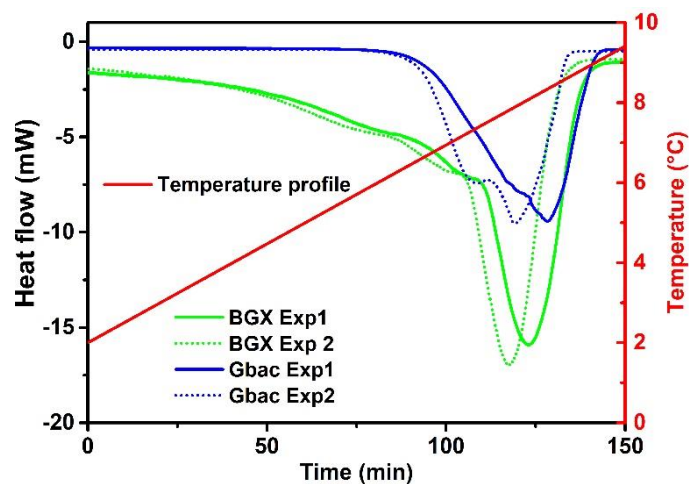


Figure 5. 11. Hydrate dissociation peaks of CP hydrates formed from CP-oversaturated PACP.

Table 5. 3. CP-conversion rates in the presence of PACP (Gbac or BGX).

	Gbac	BGX
Dissociation energy (J/g of PACP)	570 ± 30	1000 ± 45
CP-to-hydrate amount (g of CP/g of PACP)	0.35 ± 0.04	0.61 ± 0.07
CP-conversion rate (%)	44 ± 6	45 ± 6
Surface-CP-to-hydrate amount (g of CP/g of PACP)	0.35 ± 0.04	0.40 ± 0.07
Surface-CP conversion rate (%)	88 ± 12	100 ± 23

5.3.4. Visualizing of CP-hydrate crystallization from CP-loaded PACP

In order to understand why greater quantities of CP-to-hydrates are obtained in CP-oversaturated PACP systems, hydrate crystallization in CP-saturated and oversaturated Gbac and BGX systems was observed under the microscope (see Figure 5.12 for Gbac and Appendix C-5 for BGX). Figure 5.12a shows that very few hydrate crystals formed from CP-saturated Gbac particles. This result is in line with the conclusion of section 5.3.2 where the CP contained in the pores of the CP-saturated Gbac system was found to remain almost-entirely trapped (97%).

As can be seen in Figure 5.12b, upon contact with water, small CP droplets were released from the CP film present at the surface of the CP-oversaturated PACP allowing the proposal of a mechanism governing the conversion of surface-CP into hydrate (Figure 5.13). Moreover, fibrous hydrate crystals emerged from the surface of the particles toward the aqueous phase. A similar morphology was observed by Venet *et al.* (2021) [4] in experiments where the authors introduced Abac particles (smaller particles but with the same PSD as Gbac) at the interface of both excess water and CP. Concomitantly to the formation of the fibrous hydrate crystals, the CP droplets released by the PACP were converted to hydrates. The greater amounts of hydrates obtained with CP-oversaturated PACP can therefore be attributed to the high water/CP contact provided by both the external surface of the particles and the CP droplets.

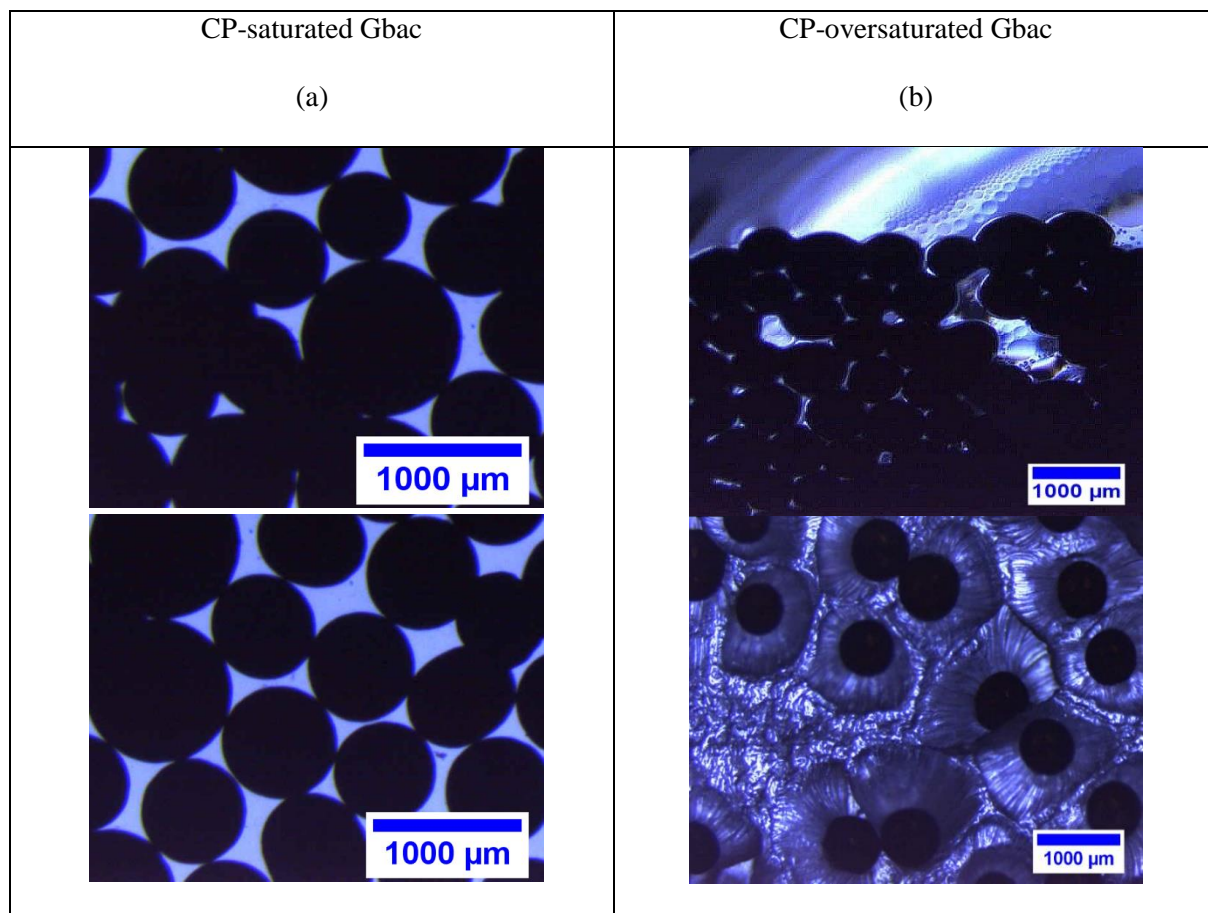


Figure 5. 12. Microscopic observation of hydrate formation from CP-saturated or oversaturated Gbac particles.

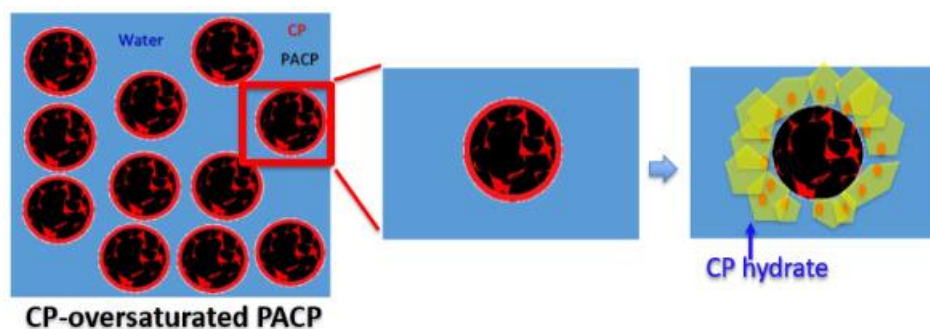


Figure 5. 13. A proposal of the mechanism governing the conversion of surface CP into hydrate.

5.4. Conclusion

This chapter investigated the prevailing mechanisms of CP-hydrate formation in (excess) pure water in the presence of PACP (Gbac, Cycarb, BGX) with different pore volumes and PSD, initially saturated or oversaturated with CP. In the case of Gbac, mainly microporous, 97% of the CP contained in pores was found to remain trapped. This result explains the small quantity of hydrates obtained in Chapter 3. The use of a PACP (BGX) with a PSD more developed in the meso- and macroporous regions and a macroporous volume about 13 times greater than that of Gbac enhanced the conversion rate of pore-CP in the same proportion. Moreover, calorimetric measurements showed that a fraction of hydrates was formed within the pores. The obtained results suggest that the CP available for hydrate formation is contained in pores of a size greater than a threshold size. Using rough hypotheses (the density of CP in the given pores is equal to the density of bulk CP, and the CP contained in the given pores is completely converted to hydrates), it could be estimated to the order of a micrometer for BGX. In the case of CP-oversaturated PACP, the CP-conversion rate increased (from about 1 to 44% for Gbac, and from about 28 to 45% for BGX) due to the high conversion rate of surface-CP ($> 88 \pm 12$ %). The microscopic observation of hydrate formation using CP-oversaturated PACP revealed that a fraction of surface CP is released as small droplets in the aqueous phase, which enhance the CP/water contact area, and thus the amount of hydrates formed. Moreover, hydrate crystals with a peculiar fibrous morphology were observed and described. To conclude, in order to optimize the quantity of hydrates formed from systems where a hydrophobic liquid hydrate former is loaded on PACP, large-pores and guest-oversaturated PACP should be used.

5.5. References

- [1] Delroisse H, Plantier F, Marlin L, Dicharry C, Frouté L, André R, Determination of thermophysical properties of cyclopentane hydrate using a stirred calorimetric cell, *J. Chem. Thermodyn.* **2018**; 125:136–41. <https://doi.org/10.1016/j.jct.2018.05.023>.
- [2] Lowell S, Shields JE, Thomas MA, Thommes M, Characterization of porous solids and powders: surface area, pore size and density, Springer Netherlands; **2004**. <https://doi.org/10.1007/978-1-4020-2303-3>.
- [3] Uchida T, Ebinuma T, Takeya S, Nagao J, Narita H. Effects of pore sizes on dissociation temperatures and pressures of methane, carbon dioxide, and propane hydrates in porous media. *J. Phys. Chem. B*, **2002**; 106:820–6. <https://doi.org/10.1021/jp012823w>.
- [4] Venet S, Broseta D, Brown R. A novel gas hydrate morphology: massive hollow fiber growth on a Porous Substrate, *Cryst. Growth Des.* **2021**; <https://doi.org/10.1021/acs.cgd.1c00161>.

Chapter 6. Experimental evaluation of the partial thermal energy compensation of hydrate crystallization from cyclopentane-loaded porous activated carbon particles immersed in brine

6.1. Introduction

In literature, few studies have been conducted with the aim to optimize hydrate formation energy [1–4]. Researchers generally tried to benefit from the endothermic energy produced by a reaction which is exogenous to the system. For instance, He *et al.* (2018) and Babu *et al.* (2020) tried to exploit LNG regasification for cooling the water to be desalinated [1,4]. He *et al.* (2018) obtained a decrease of specific energy consumption of 27.42% and 24.61% for 3.5 wt% NaCl and 7 wt% NaCl brines, respectively. In the same context, this chapter aims at showing experimental evidence of a partial thermal energy compensation as a consequence of using the CP-loaded PACP in hydrate formation. Indeed, the heat released by the exothermic hydrate crystallization (-115.4 kJ/mol of CP [5]) should be partially balanced by the endothermic CP desorption from the PACP (+28 to +57 kJ/mole of CP (see section 4.3.2.1 in Chapter 4)).

For that purpose, PACP with large pores (recommended in Chapter 5 for enhanced hydrate formation) were saturated with CP and immersed in brines (3.5 wt% and 8 wt% NaCl) to form hydrates, at a subcooling of 6 °C. Direct and indirect measurements of the thermal energies taking place during hydrate formation were performed. The former, obtained from a calorimetric study (heat flow measurements)

and accounting for both hydrate crystallization and CP desorption, was compared with the latter, deduced from an optical study (refractive index measurement) and accounting only for hydrate crystallization. The comparison of the balanced energy determined experimentally with the differential enthalpy of CP adsorption on PACP confirmed that the CP available for hydrate formation is contained in large pores. The results presented in this chapter have been reported in a publication cited as follows:

Rafik Mallek, *Christelle Miqueu, Matthieu Jacob, Christophe Dicharry, Experimental evaluation of the partial thermal energy compensation of hydrate crystallization from cyclopentane-loaded porous activated carbon particles immersed in brine, Desalination, Volume 530, 2022, 115662, <https://doi.org/10.1016/j.desal.2022.115662>.*

6.2. Experimental methods

6.2.1. Preparation of the CP-saturated PACP

The saturation of PACP with CP was performed as follows: 0.54 g of BGX were purified at 200°C under primary vacuum for 12 hrs. Using a glass funnel, 0.500 ± 0.005 g of this hot sample was immediately transferred to a resealable glass flask, which was then introduced into the closed vessel partially filled with CP (Figure 6.1). This in turn was placed in the incubator at $(1.0 \pm 0.5)^\circ\text{C}$. The PACP were left in contact with the vapor CP for 48 hrs.

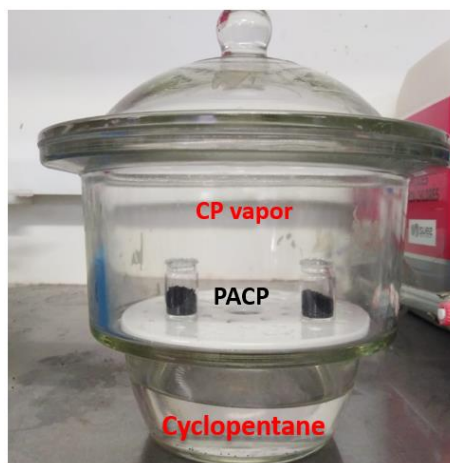


Figure 6. 1. Preparation of CP-saturated PACP.

6.2.2. Investigation into the CP desorption-CP hydrate crystallization thermal energy compensation

CP hydrates were formed in systems composed of CP-saturated BGX immersed in brine (3.5 and 8 wt% NaCl). In order to evaluate whether or not the thermal energy consumed by CP desorption from the PACP partially compensates the thermal energy released by hydrate crystallization, the thermal energy compensation was assessed by comparing the thermal energy measured in the calorimetry hydrate formation experiments (referred to as direct measurement) with the value deduced from the refractive index measurements of the unconverted water sampled at the end of the hydrate formation experiments (referred to as indirect measurement). The former corresponds to the energy $E_{des+crys}$ generated by CP desorption and hydrate crystallization, whereas the latter corresponds to the energy E_{crys} generated by hydrate crystallization only.

For this experiment, a few CP-hydrate crystals prepared beforehand were introduced into the measurement cell of the BT2.15 calorimeter along with 0.500 ± 0.005 g of CP-saturated BGX and 4.15 g (or 4.35 g) of 3.5 wt% NaCl (or 8 wt% NaCl) solution (Figure 6.2). The PACP, NaCl solution and cell were all precooled to the equilibrium temperature T_{eq} (5.5°C and 2.8°C for the 3.5 wt% NaCl and 8 wt% NaCl solutions respectively (see section 3.3.1.1 in Chapter 3)). The cell was then introduced into the calorimeter, which was set at 0.2°C above T_{eq} . A temperature profile (Figure 6.3) was imposed so that the heat flow caused when the cell was introduced was “canceled” (*i.e.* the signal could reach the baseline) and the seed hydrate crystals were melted (stage (a)). Hydrate crystallization was then initiated thanks to the memory effect (stage (b)). After 24 hrs of hydrate formation, the cell was removed from the calorimeter, a sample of the residual unconverted NaCl solution was collected and filtered, and its refractive index was measured using an Abbemat 550 refractometer (stage (c)).

$E_{des+crys}$, deduced from the direct measurements, was obtained by integrating the thermal peak generated by subtracting the “blank” thermogram (obtained in a similar fashion but without CP) from the “experiment” one (Figure 6.4). This excludes any heat flow deviation related to the heating-cooling

rates and any possible difference in mass between the reference and measurement cells. Thus, the resulting thermogram “Experiment minus Blank” shows only $E_{des+crys}$.

E_{crys} , deduced from the indirect measurements, was obtained by first determining the salinity $[NaCl]_{24h}$ of the unconverted solution - concentrated with salt as hydrates formed - from the measured refractive index and a previously generated “nD-[NaCl]” calibration curve (see Appendix D-1). Based on this, the water-to-hydrate conversion (WHC) and the water-to-hydrate amount (WHA) were determined using equations 6.1 and 6.2 respectively. The stoichiometric ratio of CP to water in the CP hydrates (1 mole of CP:17 moles of water) served to determine the amount of CP-to-hydrates obtained (CPHA) (equation 6.3). The hydrate formation energy was deduced from the CP-hydrate dissociation enthalpy (115.4 ± 7.6 kJ/mol of CP [5]) using equation 6.4.

$$WHC(\%) = 100 - \frac{100*[NaCl]_i * (100 - [NaCl]_{24h})}{(100 - [NaCl]_i) * [NaCl]_{24h}} \quad (\text{Eq. 6.1})$$

$$WHA (g) = m_{iw} * WHC (\%) \quad (\text{Eq. 6.2})$$

where $[NaCl]_i$, $[NaCl]_{24hrs}$ and m_{iw} are the initial water salinity (3.5 or 8 wt% NaCl), the final water salinity (after 24 hrs) and the initial pure-water mass respectively.

$$CPHA (g) = \frac{WHA * (17 * 18)}{70.13} \quad (\text{Eq. 6.3})$$

$$E_{crys} (J) = \frac{CPHA * 115400}{70.13} \quad (\text{Eq. 6.4})$$

The uncertainties as regards $E_{des+crys}$ were determined as the sum of experiment repetition and calibration-control deviations (see Appendix D-2 for determination of calibration-control deviation), whereas the uncertainties as regards E_{crys} were calculated from the experiment-repetition deviation, the calibration curve deviation, the refractometer accuracy, and the uncertainty regarding the dissociation enthalpy.

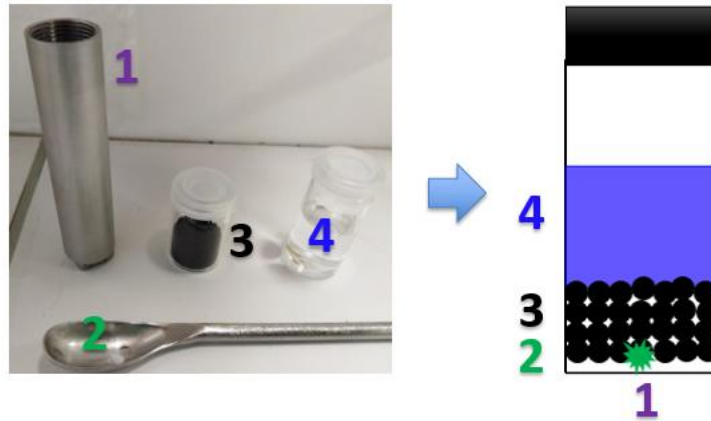


Figure 6. 2. Preparing the system for the hydrate formation experiment in the calorimetric cell of the BT2.15 apparatus. 1) measurement cell, 2) hydrate seed, 3) CP-saturated PACP, and 4) brine

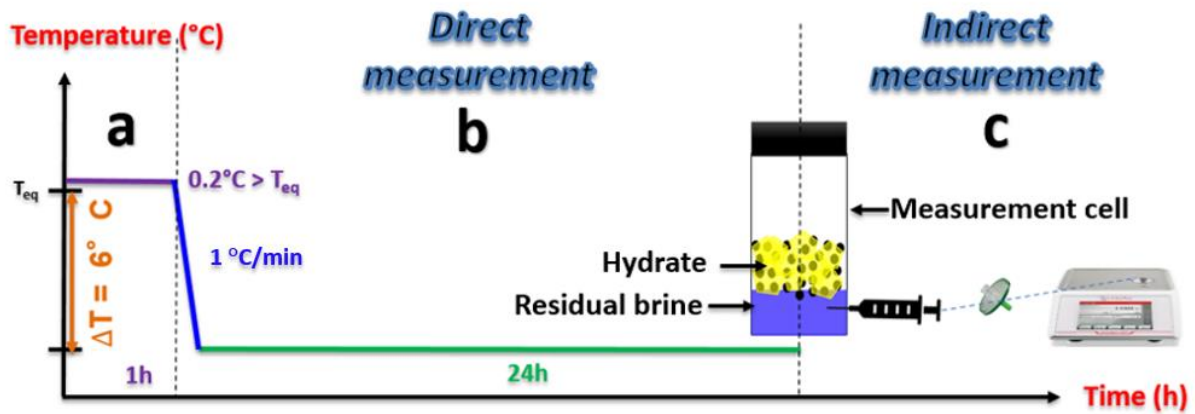


Figure 6. 3. Experimental procedure to determine thermal energy compensation.

6.3. Results and discussion

Figure 6.4 shows the resulting thermal peak (green curve) obtained after subtracting the “blank” thermogram (brown curve) from the “experiment” one (blue curve) for both NaCl solutions. The superposition of the thermal peaks obtained in experiments 1 and 2 shows a good reproducibility for each salinity (Figure 6.5). The average values of $E_{des+crys}$ obtained by integrating the thermal peaks are also given in Figure 6.5.

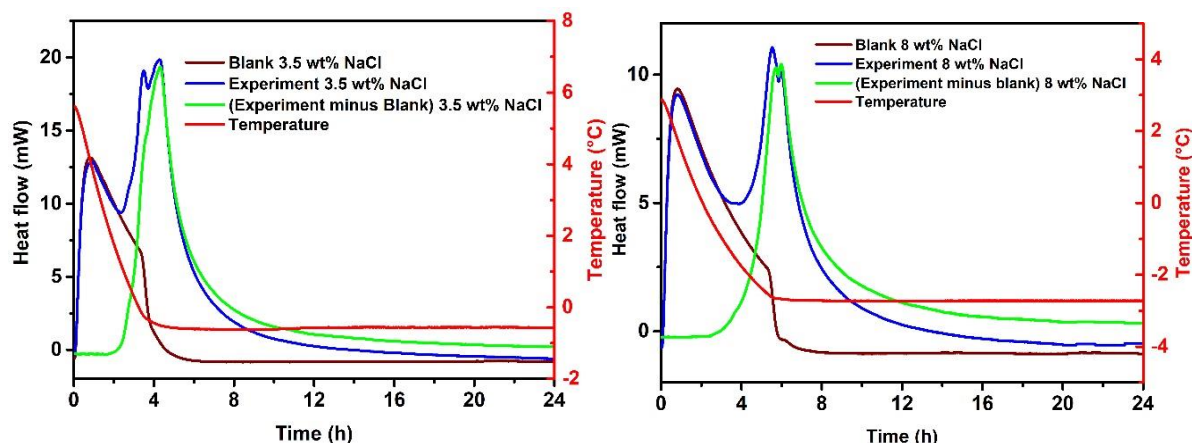


Figure 6. 4. Thermal energy peak (green curve) generated by subtracting the “blank” thermogram (brown curve) from the “experiment” thermogram (blue curve) for the 3.5 wt% NaCl solution (left) and 8 wt% NaCl solution (right).

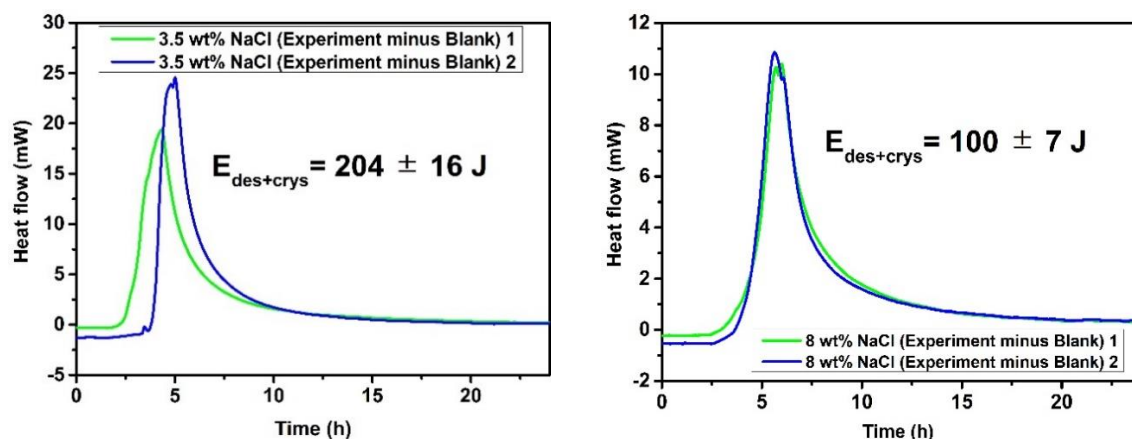


Figure 6. 5. Comparison of the thermal energy peak obtained in two repeated experiments with the 3.5 wt% NaCl solution (left) and the 8 wt% NaCl solution (right).

The thermal energy values E_{crys} deduced from the indirect measurements for the same systems are given in Table 6.1. The refractive indexes (nD) measured after 24 hrs of hydrate formation in experiments 1 and 2 are in good agreement which indicates a good reproducibility (difference of less than 0.002%).

Table 6. 1. Indirect measurement of hydrate formation energy.

		3.5 wt% NaCl	8 wt% NaCl
nD	Exp. 1	1.340402	1.348213
at t = 24 hrs	Exp. 2	1.340376	1.348220
	Average	1.340390 ± 0.00001	1.34822 ± 0.00001
[NaCl] _{24 hrs} (wt%)		4.23 ± 0.01	8.71 ± 0.01
WHC (%)		18.0 ± 0.4	8.70 ± 0.25
WHA (g)		0.72 ± 0.02	0.35 ± 0.01
CPHA (g)		0.160 ± 0.004	0.080 ± 0.002
E_{crys} (J)		271 ± 24	131 ± 12

As can be seen in Table 6.2, $E_{des+crys}$ is lower than E_{crys} . The difference in energy ($E_{crys} - E_{des+crys}$) is in fact the balanced energy. Since the PACP are initially saturated with CP, meaning the CP is found only within the pores, the balanced energy can be fully attributed to CP desorption. It can be estimated between 9 (=28-19) and 47 (=28+19) kJ/mol of CP (Table 6.2) and therefore be compared to the differential enthalpy of CP desorption. The latter, which is the opposite of the differential enthalpy of CP adsorption on PACP, ranges from 28 to 57 kJ/mol of CP. It was measured in Chapter 4 for two activated carbons with different characteristics. However, the similarity of the curves indicates a general range of values for CP adsorbed on activated carbons. For the sake of comparison, the balanced energy range and the differential enthalpy of CP desorption from PACP are plotted in the same figure (Figure 6.6).

Table 6. 2. Determination of the balanced energy per mole of CP.

	3.5 wt% NaCl	8 wt% NaCl
$E_{des+crys}$ (J)	204 ± 16	100 ± 7
E_{crys} (J)	271 ± 24	131 ± 12
Desorbed-CP amount (g)	0.16	0.08
Balanced energy (J)	67 ± 40	31 ± 19
Balanced energy (kJ/mol CP)	29 ± 17	28 ± 19

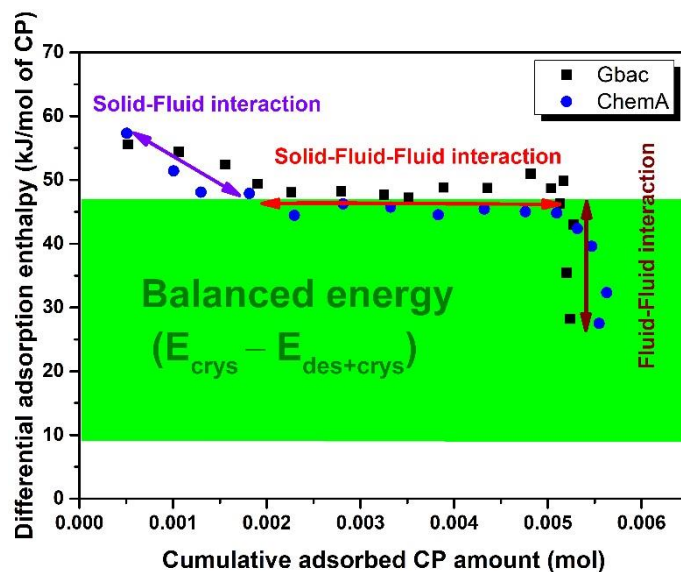


Figure 6. 6. Comparison of the balanced energy obtained in the case of hydrate formation from CP-saturated PACP (green area), and differential enthalpy of CP adsorption from PACP (blue and black dots).

While assuming that all the desorbed CP is converted to hydrates, one can infer that the former (green area) does not cover the entire range of the latter (dots), which confirms that part of the CP does not desorb from the PACP (and therefore does not participate to the formation of hydrates). The high enthalpy values (48 to 57 kJ/mol of CP) of the uncovered dots correspond to the filling of pores at low pressure. The non-desorbed CP was therefore trapped in the small pores (where the prevailing interactions are fluid-solid). The enthalpy values of the covered dots (28 to 48 kJ/mol of CP) correspond to medium-to-high-pressure pore filling of the meso- and macropores. So, the CP that desorbed from the PACP to form hydrates was contained in the large pores (where the prevailing interactions are solid-fluid-fluid and fluid-fluid interactions). This result is in line with the one obtained in Chapter 5 where the CP converted to hydrates was found to be contained in pores larger than a given threshold pore size. One can see that the balanced energy range is almost the same for both salinities (3.5 and 8 wt% NaCl), suggesting no significant effect of salt on this phenomenon. This result makes sense since the balanced energy was found to be related to the CP-desorption energy. The balanced energy (+9 to +47 kJ/mol of CP) implied a thermal energy compensation of between 8 and 40% of the energy supplied by the hydrate crystallization (115.4 kJ/mol of CP).

6.4. Conclusion

In this Chapter, the partial thermal energy compensation that may occur during hydrate formation from CP adsorbed in PACP was investigated in brines with salt concentrations typical of seawater (3.5 wt% NaCl) and produced water (8 wt% NaCl). A combination of calorimetry and refractive index measurements were used to determine the thermal energies released by both the hydrate crystallization and CP desorption from the PACP ($E_{des+crys}$), and by the hydrate crystallization alone (E_{crys}). The balanced energy ($E_{crys} - E_{des+crys}$) was found to range between 9 and 47 kJ/mol of CP for both salinities, which means that it might be possible to save 8 to 40% of the energy required by hydrate crystallization in such hydrate-based desalination process. This energy can be attributed to the desorption of CP from the large pores of the PACP. This result is in line with results of Chapter 5 in which it was demonstrated that the CP converted to hydrates was contained in the large pores of the PACP, and that the share of CP adsorbed in the smallest ones remained trapped.

6.5. References

- [1] He T, Nair SK, Babu P, Linga P, Karimi IA, A novel conceptual design of hydrate based desalination (HyDesal) process by utilizing LNG cold energy, *Applied Energy* **2018**; 222:13–24. <https://doi.org/10.1016/j.apenergy.2018.04.006>.
- [2] Lee SH, Park K. Conceptual design and economic analysis of a novel cogeneration desalination process using LNG based on clathrate hydrate, *Desalination* **2021**; 498. <https://doi.org/10.1016/j.desal.2020.114703>.
- [3] Chong ZR, He T, Babu P, Zheng J, Linga P, Economic evaluation of energy efficient hydrate based desalination utilizing cold energy from liquefied natural gas (LNG), *Desalination* **2019**; 463:69–80. <https://doi.org/10.1016/j.desal.2019.04.015>.
- [4] Babu P, Nambiar A, Chong ZR, Daraboina N, Albeirutty M, Bamaga OA, Hydrate-based desalination (HyDesal) process employing a novel prototype design. *Chem. Eng. Sci.* **2020**; 218:115563. <https://doi.org/10.1016/j.ces.2020.115563>.
- [5] Delroisse H, Plantier F, Marlin L, Dicharry C, Frouté L, André R, Determination of thermophysical properties of cyclopentane hydrate using a stirred calorimetric cell, *J. Chem. Thermodyn.* **2018**; 125:136–41. <https://doi.org/10.1016/j.jct.2018.05.023>.

General conclusion

The oil and gas industry must handle large volumes of high salinity water (known as produced water (PW)) produced as a byproduct during oil and gas extraction. Desalination of these waters may be required before any discharge or reuse operation. Hydrate-based desalination (HBD) is a potential unconventional process (compared for instance to reverse osmosis) that has been developed in the last decades. The objective of the present work was to elucidate the main mechanisms governing the hydrate formation stage in a recently patented HBD process using CP-loaded porous activated carbon particles. Hydrate formation experiments with model PW were first conducted in batch-chemical reactors. Refractive index measurements were used to evaluate both hydrate formation kinetics and hydrate-formed amounts. A preliminary diagnosis was performed while using or not PACP (here the PACP “Gbac” used in the patented process) and varying several parameters: stirring rate, CP-loading rate, PACP size and feed water salinity. At low stirring rates (up to 180 rpm), the presence of CP-loaded PACP both: i) enhanced hydrate formation kinetics by reducing induction time to few minutes; ii) increased water-to-hydrate conversion rate, for instance up to 8.2% after the first hour, iii) increased hydrate-formed amounts (high final relative water-to-hydrate conversion up to 47%). This was related to the high number of nucleation sites provided by the PACP and to their specific surface area which increased the CP/water contact area. At higher stirring rates (from 180 to 360 rpm), unexpectedly both the water-to-hydrate conversion rate and the final water-to-hydrate conversion decreased in presence of PACP, whereas they increased as expected without the PACP. Hydrate formation kinetics hardly depended on CP-loading rate whereas the hydrate-formed amount increased with the CP-loading rate of the PACP. It was found that the smaller particles induced higher hydrate formation kinetics but a lower final conversion. A possible explanation is the fact that the smallest particles provided higher CP/water contact area which might result in a fast formation of an impermeable hydrate crust around the PACP, thus limiting the CP transfer. The effect of water salinity on both hydrate formation kinetics and hydrate-formed amount was found to be negligible up to a salinity of 10 wt% NaCl. This was explained by the

high CP/water contact area provided by the specific surface area of the PACP, which overcame the inhibition effect of NaCl.

The main conclusion of these investigations is that **the PACP act as both CP source and kinetic promoter of hydrate formation. The relatively low hydrate-formed amount (relative water-to-hydrate conversion < 50%) aroused the following hypothesis: formation of an impermeable hydrate crust around the PACP or trapping of CP in the PACP pores.**

In order to investigate the low hydrate-formed amount, CP-loading/unloading of three different PACP (Gbac, ChemA and Cycarb) presenting different pore size distributions (PSD) was investigated using gravimetry, gas porosimetry, calorimetry-manometry and thermogravimetry. Adsorption and desorption of CP isotherms at 30°C were generated. CP was found to remain trapped in the PACP after desorption and a prolonged evacuation during 24 hrs under primary vacuum. The PACP with trapped CP were characterized and compared with the virgin PACP. **Results showed that CP remained trapped mainly within the pores of size lower than 1.1 nm corresponding to the ultra and super-microporosity.** CP trapping in such pores was linked to the high interactions between the fluid molecules and the solid surface. This result was corroborated with the measurement of the adsorption enthalpy of adsorption which informed on the prevailing interactions. The trapped CP was found to be completely evacuated only at a temperature higher than 277 °C under secondary vacuum. Moreover, the effect of the CP-loading method (vapor-CP adsorption and liquid-CP imbibition) on CP-trapping was concluded to be negligible. **The CP-trapping explained the low hydrate-formed amount. The use of PACP with large pores for easy CP release was thus recommended.**

To carry on the investigation, hydrate formation experiments were conducted with CP-saturated and oversaturated PACPs (Gbac, Cycarb and BGX) immersed into excess pure water within a measurement cell of a micro-differential scanning calorimetry apparatus (μ DSC7 evo). Meso-macroporous PACP (BGX) were used, based on the previous recommendation, to conduct the investigation together with two mainly micro-mesoporous previous PACP (Gbac and Cycarb). For the CP-saturated PACP, hydrate formation was cycled 50 times so that to determine the maximum CP-conversion rate that could be achieved. Higher maximum CP-conversion rate after less cycles was obtained for the meso-macroporous

PACP (*i.e.* PACP with large pore sizes) compared to the other used PACPs. **Therefore, the PSD of PACP was found to be a determinant parameter in hydrate formation.** The shift in hydrate dissociation temperature observed in these hydrate formation experiments proved that water could enter some pores and form hydrates inside them. These results and the fact that the used PACP were saturated with CP suggests that **CP contained in the large pores desorbed to form hydrates within and/or outside the pores.** PACP (Gbac and BGX) were also oversaturated so that 0.4 g of CP/g of PACP were held on their external surface. Results showed that surface CP was released as droplets in the aqueous phase before being converted to hydrate. Accordingly, it increased the CP conversion from 1 to 44% for Gbac, and from 28 to 45% for BGX.

As mentioned previously, CP must desorb from the PACP to form hydrates with water. The former reaction is endothermic, whereas the latter is exothermic. Therefore, the concomitance of both reactions (CP desorption and hydrate crystallization) should cause a partial thermal energy compensation. This phenomenon was evaluated experimentally by forming hydrate from CP-saturated meso-macroporous PACP (BGX) immersed in excess brine (3.5 wt% NaCl and 8 wt% NaCl) within the measurement cell of a Calvet calorimeter (BT2.15). After 24 hrs of hydrate formation, the thermal energy $E_{des+crys}$ due to both CP-desorption and hydrate crystallization was obtained by integrating the resulting thermal peaks, while the thermal energy due to only hydrate crystallization E_{crys} was deduced from the refractive index of the residual brine. The comparison of $E_{des+crys}$ and E_{crys} showed an energy difference between 9 and 47 kJ/mol of CP, **thus, a thermal energy compensation between 8 and 40% of the hydrate crystallization enthalpy.** The compensated energy was compared to the desorption differential enthalpy of CP from PACP and **it was concluded that CP converted to hydrate was desorbed from large pores** which is in line with our previous results.

Perspectives

As further work, hydrate formation from porous media other than PACP could be investigated. The idea would be to identify a porous media (native or functionalized) for which the desorption enthalpy of CP is higher than in the present work, and having a large meso- macroporous volume. From there, hydrate formation and energetic aspects could be better controlled, that is, both the hydrate-formed amount and thermal energy compensation might be optimized.-Furthermore, the porous media particle size could also be optimized so that a higher surface-CP amount could be held on the external surface of the particles, thus a possibility of enhancing the hydrate-formed amount. In addition, the effect of porous media shaping (woven, compact, etc.) could be investigated. Eutectic conditions, where a mixture crystallize/melt as if it was a pure substance, could serve in increasing both hydrate formation kinetics and hydrate-formed amount. Indeed, formation of hydrate in brine at eutectic conditions should take place at a constant water salinity (eutectic concentration), thus a constant imposed subcooling, and should end with an entirely solid system (salt and hydrate). To carry out this work, eutectic points of hydrate-salt mixtures should be first determined and then hydrate formation (with or without porous media) could be evaluated.

General overview of the thesis (In French)

Introduction générale

Au cours des dernières décennies, le monde a connu une croissance démographique notable (1 à 2% [1]) et un développement technologique rapide qui ont entraîné à la fois une augmentation de la consommation d'énergie et une dégradation de l'environnement. Par conséquent, l'approvisionnement en énergie et la protection de l'environnement sont devenus une priorité mondiale. Cela se reflète à la fois dans la croissance de la demande d'énergie (+27% prévus de 2017 à 2040 [2]) et dans les différentes conventions et réglementations environnementales (protocole de Kyoto, COPs, etc.).

L'industrie pétro-gazière est l'un des principaux fournisseurs d'énergie, représentant 54,4 % de l'approvisionnement énergétique mondial [3]. Pendant la production d'hydrocarbures, de grandes quantités d'eau (environ 75 % des effluents [4]) de salinité élevée (environ 8 %m de TDS[†] [5]), appelée eau de production, sont coproduites. Une bonne gestion de ce sous-produit est l'un des défis de l'industrie pétro-gazière. L'eau de production peut être stockée, rejetée ou réutilisée. Le stockage n'est pas envisageable en raison des énormes quantités d'eau produite, tandis que le rejet (souvent dans l'eau de mer) et/ou la réutilisation (principalement la réinjection dans le réservoir de production pour maintenir la pression du réservoir) sont les options les plus courantes. En raison de la forte salinité de l'eau produite, les restrictions environnementales (lois et réglementations) et les limitations techniques (problèmes éventuels de compatibilité avec l'eau de formation, corrosion des tubes, etc.) font du dessalement de l'eau un processus recommandé avant toute opération de décharge ou de réinjection.

De nos jours, plusieurs procédés de dessalement de l'eau sont utilisés, notamment l'osmose inverse (RO), les procédés basés sur la distillation (Multi-stage flash (MSF), multi-effect distillation (MED)), la nanofiltration (NF), l'électrodialyse (ED), etc. L'osmose inverse et la distillation de l'eau sont les procédés les plus utilisés (65 et 30 %, respectivement de la capacité mondiale de dessalement) [6].

[†] Total dissolved solids (connu comme « la matière sèche ») : la concentration totale de matières organiques et inorganiques dissoutes dans l'eau

Cependant, ces procédés conventionnels présentent soit des limitations techniques (une faible salinité de l'eau d'alimentation est requise dans le cas du RO (< 4,3 % en poids de TDS [7])), soit un impact économique élevé (une forte consommation d'énergie pour la distillation induisant des coûts élevés (1,1-1,5 USD/m³ [8])). Dans le but de dépasser ces limitations, un procédé de dessalement non conventionnel basé sur la formation d'hydrates de gaz (procédé appelé HBD) a été proposé comme une alternative potentielle [9]. Ce dernier exploite la formation et la dissociation des hydrates de gaz pour produire une eau moins salée. En effet, les sels présents dans le système ne participent pas à la structure de ces solides cristallins formés à partir de molécules d'eau et de molécules « invitées » (souvent un hydrocarbure léger ajouté au système). Le choix des molécules invitées peut permettre de procéder à des températures supérieures à la température normale de solidification de l'eau [8]. Les cristaux d'hydrate formés sont séparés de la saumure restante, dans laquelle les sels se sont concentrés. Les cristaux séparés sont ensuite dissociés et l'eau dessalée (en théorie de l'eau pure) est produite. Même si le procédé HBD semble prometteur, il n'est toujours pas applicable à l'échelle industrielle, principalement en raison de la faible cinétique de formation des hydrates et de l'énergie fournie relativement élevée. En conséquence, plusieurs recherches ont été menées afin de se débarrasser de ces aspects restrictifs [8].

Pour tenter de surmonter ces limitations, une start-up française appelée BGH a récemment breveté un nouveau procédé de dessalement basé sur le concept HBD, appelé ici procédé BGH [10], dans lequel des particules poreuses de charbon actif (PPCA) sont chargées de cyclopentane (CP) et immergées dans l'eau à dessaler à une température appropriée. Le CP a l'avantage de former des hydrates à la pression atmosphérique et à des températures inférieures à environ 7°C. On peut distinguer quatre étapes principales dans le procédé BGH : i) le chargement des PPCA avec le CP, ii) la formation des hydrates de CP, iii) la séparation des cristaux d'hydrates de la saumure restante, et iv) la dissociation des cristaux d'hydrate séparés. Bien que les résultats préliminaires obtenus par la start-up sur les eaux de production semblent prometteurs, une compréhension détaillée du rôle des PPCA et des mécanismes impliqués dans la formation des hydrates est encore nécessaire notamment pour améliorer/optimiser ce procédé.

Le but de ce travail est d'étudier les deux premières étapes du procédé BGH en utilisant des eaux de production modèles (saumures de NaCl à différentes concentrations). Les mécanismes régissant la

formation d'hydrates à partir de PPCA chargées en CP sont étudiés, et les principales questions abordées sont la formation d'hydrates et les aspects énergétiques résultant de l'utilisation du PPCA chargées en CP. En résumé, l'objectif de cette thèse est de répondre à la question suivante : quelle est l'utilité des PPCA chargées en CP dans la formation d'hydrates (procédé BGH) par rapport à une formation conventionnelle d'hydrates de CP « en vrac » (procédé classique HBD) ?

Le plan de travail de la thèse est de :

- faire une étude bibliographique pour mettre en relation l'état de l'art sur les investigations déjà réalisées sur le procédé HBD, les clathrates hydrates, les phénomènes d'adsorption/désorption et la formation d'hydrates en présence de milieux poreux.

- déterminer la région de stabilité des CP-hydrates et leur vitesse de croissance sans PPCA en fonction de la concentration en NaCl.

- évaluer l'effet des principaux paramètres (taille du PACP, distribution de la taille des pores, vitesse d'agitation, taux de chargement en CP et salinité de l'eau d'alimentation) du procédé BGH sur la formation d'hydrates.

- comprendre les mécanismes régissant de la formation d'hydrates à partir de PPCA chargées en CP (principalement les aspects formation d'hydrates et phénomènes énergétiques).

Principaux résultats et conclusions

L'industrie pétro-gazière doit traiter de grands volumes d'eau à forte salinité, dénommée eau de production, qui est un sous-produit de l'extraction des hydrocarbures. Le dessalement de ces eaux peut être nécessaire avant toute opération de rejet ou de réutilisation. Le dessalement à base d'hydrates (HBD) est un procédé potentiel non conventionnel (comparé par exemple à l'osmose inverse) qui a été développé au cours des dernières décennies. L'objectif de ce travail était d'élucider les principaux mécanismes régissant l'étape de formation des hydrates dans un procédé de dessalement à base d'hydrates récemment breveté, utilisant des particules de charbon actif poreuses (PPCA) chargées en cyclopentane (CP).

Des expériences de formation d'hydrates avec des eaux de production modèles ont d'abord été menées dans des réacteurs chimiques « batch ». Des mesures d'indice de réfraction ont été utilisées pour évaluer à la fois la cinétique de formation des hydrates et la quantité d'hydrates formés. Un diagnostic préliminaire a été réalisé en utilisant ou non les PPCA (ici les PPCA "Gbac" utilisées dans le procédé breveté) et en faisant varier plusieurs paramètres : vitesse d'agitation, taux de chargement en CP, taille des PACP et salinité de l'eau d'alimentation. À des taux d'agitation faibles (jusqu'à 180 tours/min), la présence des PPCA chargées en CP a à la fois : i) amélioré la cinétique de formation des hydrates en réduisant le temps d'induction à quelques minutes ; ii) augmenté le taux de conversion de l'eau en hydrates, par exemple jusqu'à 8,2 % après la première heure, iii) augmenté la quantité d'hydrates formés (conversion relative finale élevée de l'eau en hydrates jusqu'à 47 %). Ceci était lié au nombre élevé de sites de nucléation fournis par les PPCA et à leur surface spécifique qui augmentait la surface de contact CP/eau. A des taux d'agitation plus élevés (de 180 à 360 tours/min), le taux de conversion de l'eau en hydrates et la conversion finale de l'eau en hydrates ont diminué en présence des PPCA, ce qui n'était pas attendu, alors qu'ils ont augmenté comme prévu sans les PPCA. La cinétique de formation d'hydrates dépendait à peine du taux de chargement en CP alors que la quantité d'hydrates formés augmentait avec ce dernier. Il a été constaté que les petites PPCA induisaient une cinétique de formation d'hydrates plus élevée mais une conversion finale plus faible. Une explication possible est le fait que les petites particules fournissent une plus grande surface de contact CP/eau qui pourrait résulter en une formation

rapide d'une croûte d'hydrates imperméable autour des PPCA, limitant ainsi le transfert de CP. L'effet de la salinité de l'eau sur la cinétique de formation des hydrates et la quantité d'hydrates formés s'est avéré négligeable jusqu'à une salinité de 10 %m de NaCl. Ceci s'explique par la surface de contact CP/eau élevée fournie par la surface spécifique des PPCA, qui a surmonté l'effet d'inhibition du NaCl.

La principale conclusion tirée de cette partie d'étude est que **les PPCA agissent à la fois comme source de CP et comme promoteur cinétique de la formation d'hydrates. La faible quantité d'hydrates formés (conversion relative eau en hydrates < 50%) a suscité les hypothèses suivantes : formation d'une croûte d'hydrates imperméable autour des PPCA ou piégeage du CP dans les pores des PPCA.**

Afin d'étudier la faible quantité d'hydrates formés, le chargement/déchargement du CP de trois PPCA différents (Gbac, ChemA et Cycarb) présentant différentes distributions en taille de pores (PSD) a été étudié en utilisant des techniques de gravimétrie, de porosimétrie gazeuse, de calorimétrie-manométrie et de thermogravimétrie. Des isothermes d'adsorption et de désorption du CP à 30°C ont été générées. On a constaté que le CP restait piégé dans les PPCA après désorption et une évacuation prolongée pendant 24 heures sous vide primaire. Les PPCA avec du CP piégé ont été caractérisées et comparées aux PPCA vierges. **Les résultats ont montré que le CP restait piégé principalement dans les pores de taille inférieure à 1.1 nm correspondant à l'ultra et super-microporosité.** Le piégeage du CP dans ces pores est lié aux interactions élevées entre les molécules du fluide et la surface solide des PPCA. Ce résultat a été corroboré par la mesure de l'enthalpie différentielle d'adsorption qui renseigne sur les interactions dominantes. On a constaté que le CP piégé n'était complètement évacué qu'à une température supérieure à 277 °C sous vide secondaire. De plus, l'effet de la méthode de chargement de CP (adsorption de vapeur de CP ou imbibition de CP liquide) sur son piégeage a été conclu comme étant négligeable. Le piégeage du CP explique la faible quantité d'hydrates formés. **L'utilisation des PPCA avec de grands pores pour une libération facile du CP a donc été recommandée.**

Pour mener cette étude, des expériences de formation d'hydrates ont été réalisées avec des PPCA saturées et sursaturées en CP (Gbac, Cycarb et BGX) immergées dans un excès d'eau pure dans une cellule de mesure d'un appareil de calorimétrie à balayage micro-différentiel (μ DSC7 evo). Des PPCA

méso-macroporeuses (BGX) ont été utilisées, sur la base de la recommandation précédente, ainsi que deux PPCA précédentes principalement micro-mésoporeuses (Gbac et Cycarb). Pour les PPCA saturées en CP, la formation d'hydrates a été cyclée 50 fois afin de déterminer le taux maximal de conversion du CP qui pouvait être atteint. Un taux maximal de conversion plus élevé après moins de cycles a été obtenu pour les PPCA méso-macroporeuses (c'est-à-dire les PPCA avec de grandes tailles de pores) comparé aux autres PACP utilisées. **Par conséquent, la PSD des PPCA s'est avérée être un paramètre déterminant dans la formation d'hydrates.** Le décalage de la température de dissociation des hydrates observé dans ces expériences de formation d'hydrates a prouvé que l'eau pouvait pénétrer dans certains pores et former des hydrates à l'intérieur de ceux-ci. Ces résultats et le fait que les PPCA utilisées étaient saturées en CP suggèrent que **le CP contenu dans les grands pores s'est désorbé pour former de l'hydrate à l'intérieur et/ou à l'extérieur des pores.** Les PPCA (Gbac et BGX) ont également été sursaturées de sorte que 0,4 g de CP/g de PACP était retenu sur leur surface externe. Les résultats ont montré que le CP sur la surface externe était libéré sous forme de gouttelettes dans la phase aqueuse avant d'être converti en hydrates. En conséquence, cela a augmenté la conversion du CP de 1 à 44% pour le Gbac, et de 28 à 45% pour le BGX.

Comme mentionné précédemment, le CP doit se désorber des PPCA pour former l'hydrate avec l'eau. La première réaction est endothermique, alors que la seconde est exothermique. Par conséquent, la concomitance des deux réactions (désorption du CP et cristallisation de l'hydrate) devrait provoquer une compensation partielle de l'énergie thermique. Ce phénomène a été évalué expérimentalement en formant de l'hydrate à partir de PPCA méso-macroporeuses saturées en CP (BGX) immergées dans un excès de saumure (3,5 % m de NaCl et 8 % m de NaCl) dans la cellule de mesure d'un calorimètre Calvet (BT2.15). Après 24 heures de formation d'hydrates, l'énergie thermique $E_{des+crys}$ due à la fois à la désorption du CP et à la cristallisation des hydrates a été obtenue en intégrant les pics thermiques résultants, tandis que l'énergie thermique due seulement à la cristallisation d'hydrates E_{crys} a été déduite de l'indice de réfraction de la saumure résiduelle. La comparaison de $E_{des+crys}$ et E_{crys} a montré une différence d'énergie entre 9 et 47 kJ/mol de CP, **donc une compensation d'énergie thermique entre 8 et 40% de l'enthalpie de cristallisation de l'hydrate.** L'énergie compensée a été comparée à l'enthalpie

différentielle de désorption du CP des PPCA et il a été conclu que **le CP converti en hydrates a été désorbé des grands pores** ce qui est en accord avec nos résultats précédents.

Perspectives

Comme travail ultérieur, la formation d'hydrates à partir de milieux poreux autres que le PPCA pourrait être envisagée. L'idée serait d'identifier un milieu poreux (natif ou fonctionnalisé) pour lequel l'enthalpie de désorption du CP est plus élevée que dans le présent travail, et ayant un grand volume mésoporeux. A partir de là, la formation d'hydrates et les aspects énergétiques pourraient être mieux contrôlés, c'est-à-dire que la quantité d'hydrates formés et la compensation de l'énergie thermique pourraient être optimisées. En outre, la taille des particules du milieu poreux pourrait également être optimisée de manière à ce qu'une plus grande quantité de CP puisse être maintenue sur la surface externe des particules, ce qui permettrait d'augmenter davantage la quantité d'hydrates formés. L'effet de la forme du milieu poreux (tissé, compact...etc.) pourrait également être étudié. Enfin, les conditions eutectiques, où un mélange cristallise/fond comme s'il s'agissait d'une substance pure, pourraient servir à augmenter à la fois la cinétique de formation des hydrates et la quantité d'hydrates formés. En effet, la formation d'hydrates dans une saumure aux conditions eutectiques devrait avoir lieu à une salinité de l'eau constante (concentration eutectique), donc à un sous-refroidissement imposé constant, et devrait aboutir à un système entièrement solide (sel et hydrate). Pour mener à bien ce travail, il faudrait d'abord déterminer les points eutectiques des mélanges hydrate-sel, puis évaluer la formation des hydrates (avec ou sans milieu poreux).

References

- [1] World Population Clock: 7.9 Billion People **2021** - Worldometer n.d. <https://www.worldometers.info/world-population/>
- [2] Babu P, Nambiar A, Chong ZR, Daraboina N, Albeirutty M, Bamaga OA, Hydrate-based desalination (HyDesal) process employing a novel prototype design, *Chem. Eng. Sci.* **2020**; 218:115563. <https://doi.org/10.1016/j.ces.2020.115563>.
- [3] Key World Energy Statistics 2020 – Analysis. IEA n.d. <https://www.iea.org/reports/key-world-energy-statistics-2020>
- [4] Abousnina R, An overview on oil contaminated sand and its engineering applications. *Int. J. geomate* **2015**; 10:1615–22. <https://doi.org/10.21660/2016.19.150602>.
- [5] Cha JH, Seol Y. increasing gas hydrate formation temperature for desalination of high salinity produced water with secondary guests. *ACS Sustain. Chem. Eng.* **2013**; 1:1218–24. <https://doi.org/10.1021/sc400160u>.
- [6] Islam MS, Sultana A, Saadat AHM, Islam MS, Shammi M, Uddin MK. desalination technologies for developing countries: a review, *J. Sci. Res.* **2018**; 10:77–97. <https://doi.org/10.3329/jsr.v10i1.33179>.
- [7] Younos T, Tulou KE, overview of desalination techniques: overview of techniques, *J. Contemp Water Res. Educ.* **2009**; 132:3–10. <https://doi.org/10.1111/j.1936-704X.2005.mp132001002.x>.
- [8] Babu P, Nambiar A, He T, Karimi IA, Lee JD, Englezos P, a review of clathrate hydrate based desalination to strengthen energy–water nexus. *ACS Sustain. Chem. Eng.* **2018**; 6:8093–107. <https://doi.org/10.1021/acssuschemeng.8b01616>.
- [9] Zheng J, Cheng F, Li Y, Lü X, Yang M. Progress and trends in hydrate based desalination (HBD) technology: A review. *Chin J Chem Eng* **2019**; 27:2037–43. <https://doi.org/10.1016/j.cjche.2019.02.017>.
- [10] Mottet B, Method for crystallising clathrate hydrates, and method for purifying an aqueous liquid using the clathrate hydrates thus crystallised, Applicant: BGH[FR]. EP3153606, <https://worldwide.espacenet.com/patent/search/family/054476876/publication/WO2017060456A1?q=PCT%2FEP2016%2F074044>.

Appendix

Appendix A

A-1) nD -[NaCl] calibration points

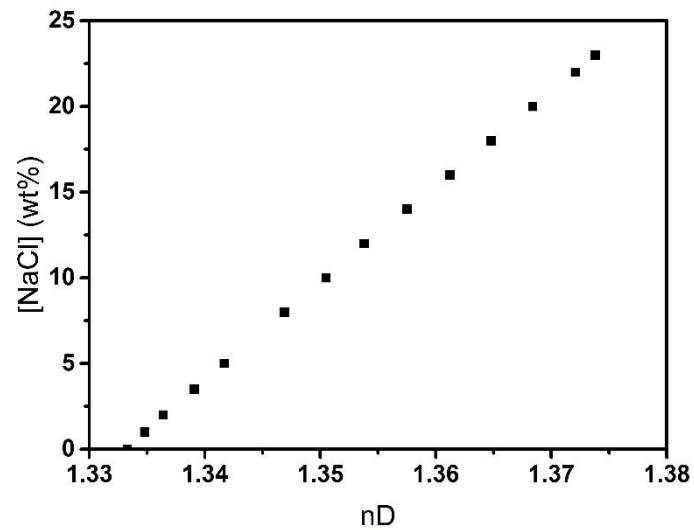


Figure A-1.1. nD -[NaCl] calibration points produced with Abbemat 3200 refractometer.

A-2) Hydrate crystals morphology

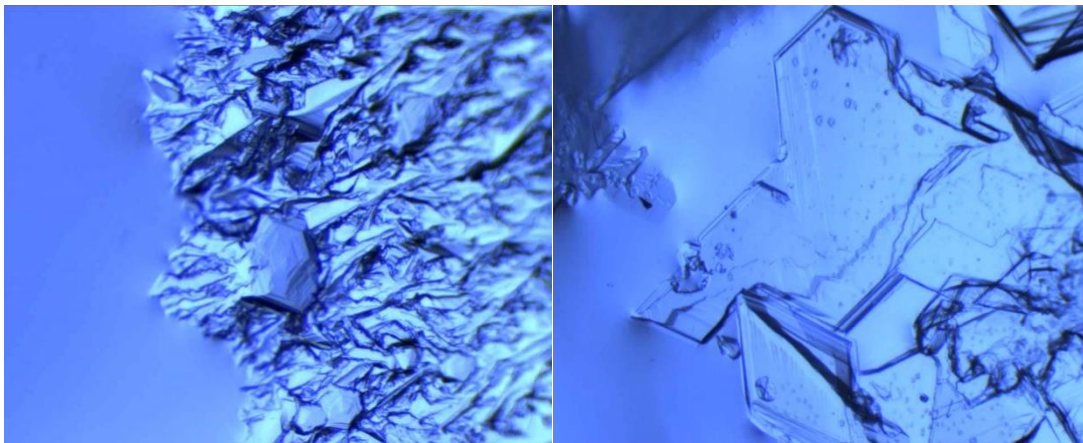


Figure A-2.1. Images showing the morphology of CP-hydrate crystals formed at the subcooling of 6°C (left) and 2°C (right).

Appendix B

B-1) Gravimetric technique: Calibration of the measurement system

The masses and volumes of the sample together with both the crucible and the cylinder ($m_{adsorbent}$, m_{Cr} , m_{Cy} , $V_{adsorbent}$, V_{Cr} , V_{Cy} respectively) are determined through He calibration prior any injection of the gas/vapor to be adsorbed. Indeed, He, which is considered as a non-adsorbed gas, is injected into the adsorption chamber where the sample is placed within the crucible. ZP and MP2 are measured at different pressures at a fixed temperature (temperature of the study). The quantity MP2- ZP (equation B-1.1) is plotted against the vapor/gas density ($\rho_{vapor/gas}(P, T)$) determined experimentally at the previous pressures and temperature (equation B-1.2). Thereby, the terms $m_{adsorbent}$, $V_{adsorbent}$, m_{Cr} , V_{Cr} are determined.

$$MP2 - ZP = m_{Cr} + m_{Cy} + m_{adsorbent} - \rho_{gas/vapor} (V_{Cr} + V_{Cr} + V_{adsorbent}) \quad (\text{Eq. B-1.1})$$

$$(\rho_{gas/vapor}(P, T) = \frac{m_{Cy} - (MP2 - MP1)}{V_{Cy}} \quad (\text{Eq. B-1.2})$$

Providing that the masses and the volumes of the crucible and the cylinder are already known, the sample mass and volume are determined (Tables B-1.1 and B-1.2 respectively).

Table B-1.1. *Mass and volume of the crucible and the cylinder.*

	Crucible	Cylinder
Mass (g)	8.15	20.05
Volume (cm ³)	1.03	4.44

Example of He calibration result:

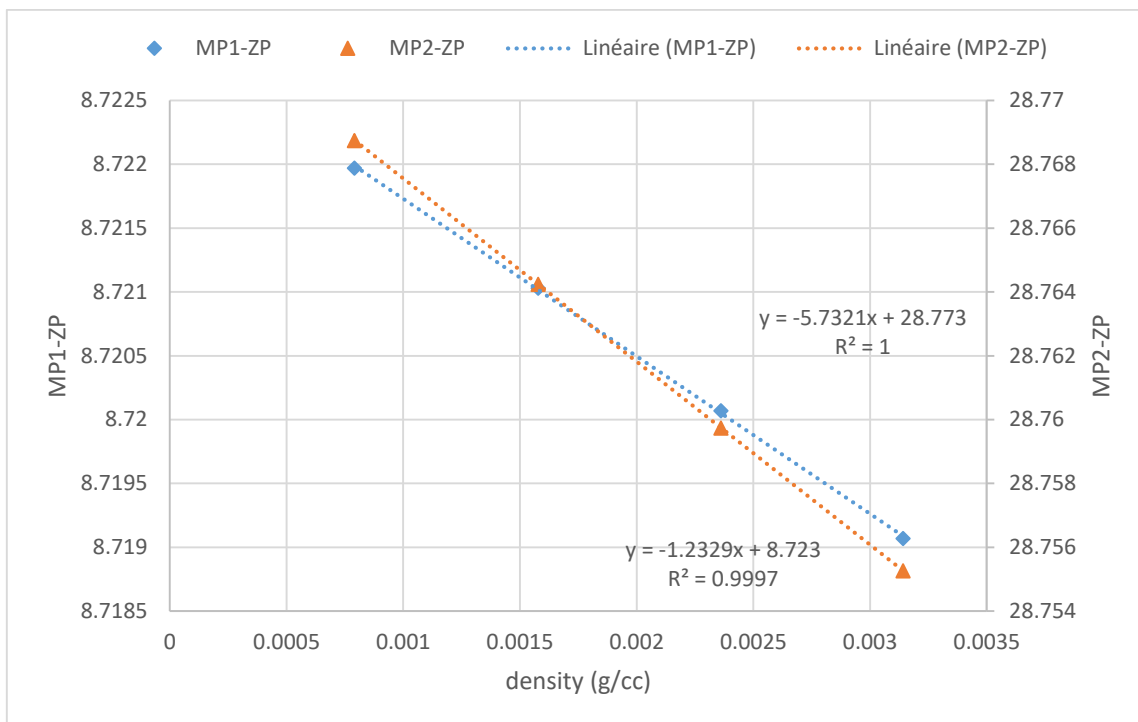


Figure B-1.1. Example of He calibration obtained for the system (PACP: ChemA).

The mass and volume of the sample can be determined as follows:

Table B-1.2. Determination of the mass and volume of PACP (ChemA).

	MP2-ZP
$m_{\text{adsorbent}} + m_{\text{Cr}} + m_{\text{Cy}}$ (g)	28.78
$V_{\text{adsorbent}} + V_{\text{Cr}} + V_{\text{Cy}}$ (cm ³)	5.73
$m_{\text{adsorbent}}$ (g)	0.57
$V_{\text{adsorbent}}$ (cm ³)	0.26

B-2) Skeleton density determination

The skeleton density is determined by the gravimetric technique thanks to the calibration of the system (sample (adsorbent) + crucible + cylinder) with He. Indeed, as already shown, He calibration allows the determination of both the system mass and volume including the sample.

The sample mass corresponds to the skeleton mass and the sample volume is the skeleton volume (since it is determined with He, which is supposed not being adsorbed). Accordingly, the skeleton density is deduced from the mass and the volume of the skeleton.

Example:

The skeleton density of ChemA can be determined as follows:

$$\text{Skeleton density}_{\text{ChemA}} = \frac{m_{\text{absorbent}}}{V_{\text{adsorbent}}} = \frac{0.57}{0.26} = 2.19 \text{ cm}^3/\text{g}$$

B-3) Calo-manometric technique: Calibration of the measurement system

The system was calibrated with He in order to determine the volumes V_M and V_E , appearing in equations 2.11 and 2.13 and depicted in Figure 2.10b (see Chapter 2), presenting the adsorption volume and the effective volume, respectively. Details of calibration method are given by Mouahid *et al.* (2010) [1].

Example of calibration results:

Determination of V_M

Providing that: $V_d = 16.66 \pm 0.06 \text{ cm}^3$

Table B-3.1. Amounts of Helium within the dosing volume.

V_d			
P (bar)	T (°C)	c (mol/cm ³)	n (mol)
4.51	30	0.0002	0.003
9.62	30	0.0004	0.006
12.64	30	0.0005	0.008
18.10	30	0.0007	0.012

Table B-3.2. Determination of the adsorption volume V_m .

$V_d + V_m$			
P (bar)	T (°C)	c (mol/cm ³)	V_m (cm ³)
3.38	30	0.0001	5.57
7.16	30	0.0003	5.70
9.44	30	0.0004	5.60
13.54	30	0.0005	5.56

$$V_M = 5.60 \text{ cm}^3$$

Determination of V_E

Table B-3.3. Determination of the effective volume V_E .

T °C	Calib. mW/ μ V	P1 bar	P2 bar	ΔP bar	Ahp 1/K	AHE-ASS 1/K
30	0.031	0	3.38	3.38	3.30E-03	3.25E-03
30	0.031	0	7.16	7.16	3.30E-03	3.25E-03
30	0.031	0	9.44	9.44	3.30E-03	3.25E-03
30	0.031	0	13.54	13.54	3.30E-03	3.25E-03

Peak integration μ V.s	Q_{comp} J	k/V_E bar/ $(\mu$ V.s)	V_E cm^3
-52165	-1.63	6.38 E-05	4.91E+00
-112623	-3.53	6.26 E-05	5.00 E+00
-152975	-4.79	6.08 E-05	5.15 E+00
-221139	-6.92	6.03 E-05	5.19 E+00

$$V_E = 5.06 \text{ cm}^3$$

B-4) Evaluation of CP-adsorption kinetics

The best experiment to measure the adsorption kinetics would be to perform the adsorption breakthrough curves through a bed of PACP. However, the magnetic suspension balance from Rubotherm allows to record the adsorbed mass as function of time and thus can give some insights into the adsorption kinetics. It should be noted that the pressure range (pressure step) must be the same and the microvalve opening controlled similarly in order to obtain reliable kinetics comparison.

As an example, the Figure B-4.1 is obtained when determining the first point of CP-adsorption isotherms on Gbac and Abac whose particle sizes are 689 μm and 326 μm , respectively. It shows that a larger particle size typically affects adsorption kinetics, showing a shallower adsorption breakthrough curve.

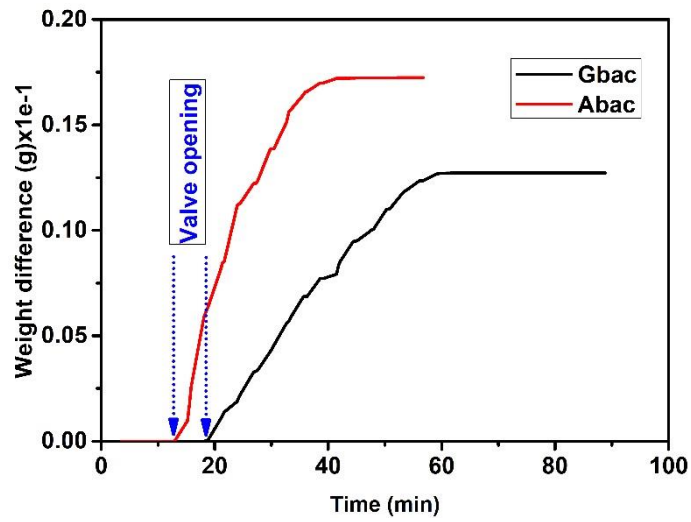


Figure B-4.1. Evaluation of the adsorption kinetics of CP on Gbac and Abac.

B-5) External morphology of Gbac and Abac observed with a light microscope

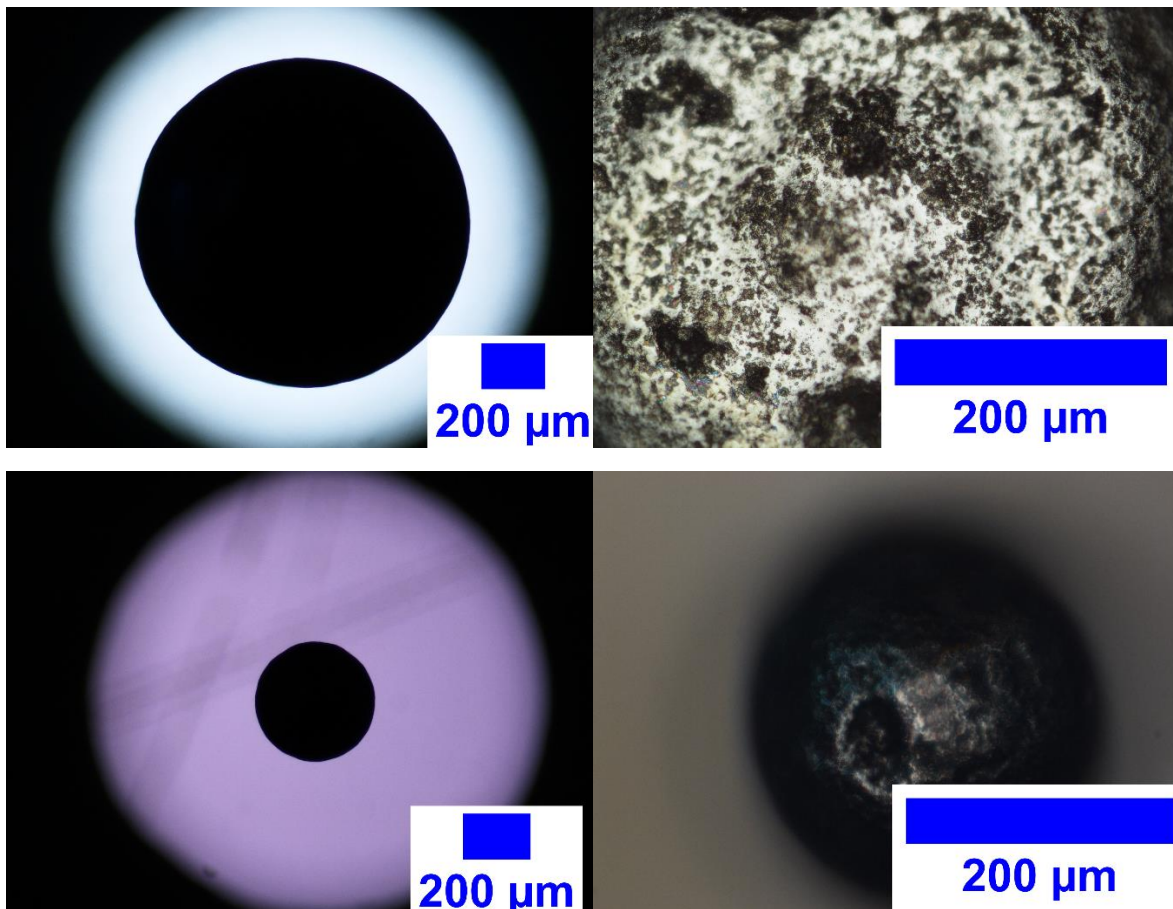


Figure B-5.1. Light transmission (left) and light reflection (right). a) G-BAC-G70R; b) A-BAC-SP

Appendix C

C-1) Preparation of CP-saturated PACP



Figure C-1.1. Closed-vessel, partially filled with CP (adsorption chamber), used for adsorption capacity determination of the PACP and preparation of CP-saturated PACP for the hydrate formation experiments.

C-2) Adsorption isotherm of CP on BGX

Adsorption isotherm of CP on BGX at 30 °C was generated using Rubotherm Magnetic Suspension Balance. The accuracy on the adsorbed mass and pressure is $\pm 10^{-5}$ g and ± 0.005 bar respectively.

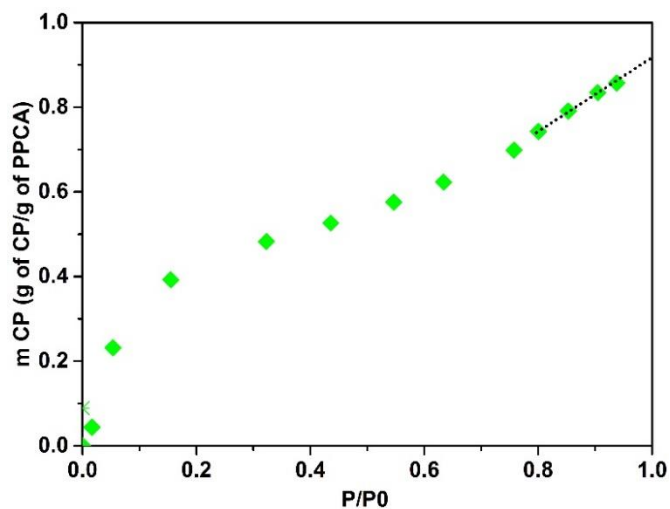


Figure C-2.1. CP-adsorption isotherm of CP on BGX at 30 °C.

C-3) CP-adsorption capacity of BGX at 30 °C

Table C-3.1. Validation of the closed-vessel method used in measuring adsorption capacities and sample preparation.

	CP-vapor closed-vessel	Magnetic suspension balance
CP adsorption capacity of BGX at 30 °C	0.93	0.91

C-4) Calibration control of micro-DSC7 evo apparatus.

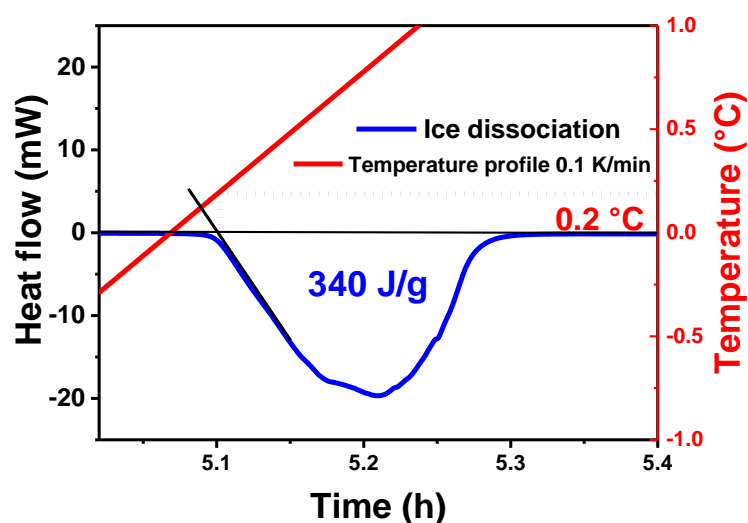


Figure C-4.1. Ice dissociation for micro-DSC7 evo calibration control.

C-5) Microscopic observation of hydrate formation from CP-loaded BGX

The Figure C-5.1 depicts hydrate crystallization in the CP-saturated and CP-oversaturated BGX system. Before hydrate crystallization, surface-CP film is not clearly observed. Nonetheless, CP droplets are released in the aqueous phase before hydrate crystallization. Identically to oversaturated Gbac particles, a high hydrate amount is formed within the aqueous phase thanks to the high water/CP contact area provided by both CP droplets and particle external surface. However, no fiber-like hydrate crystals were observed.

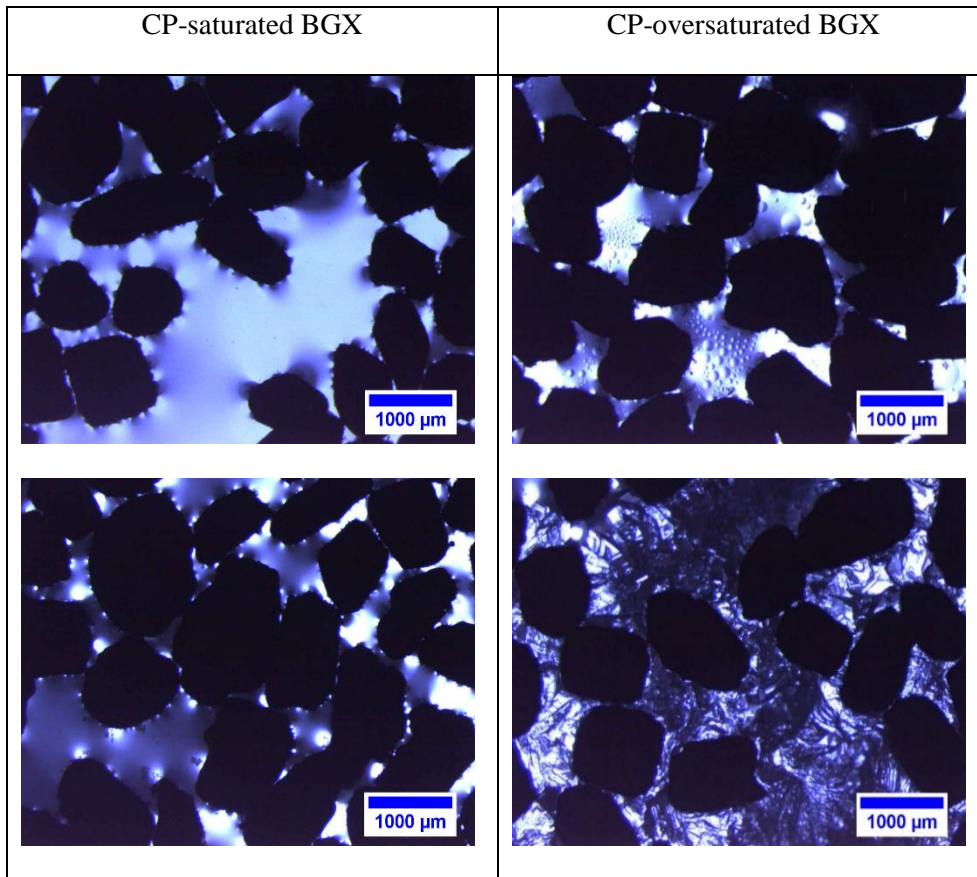


Figure C-5.1. Microscopic observation of hydrate formation from CP-saturated and oversaturated BGX particles.

Appendix D

D-1) nD-[NaCl] calibration points

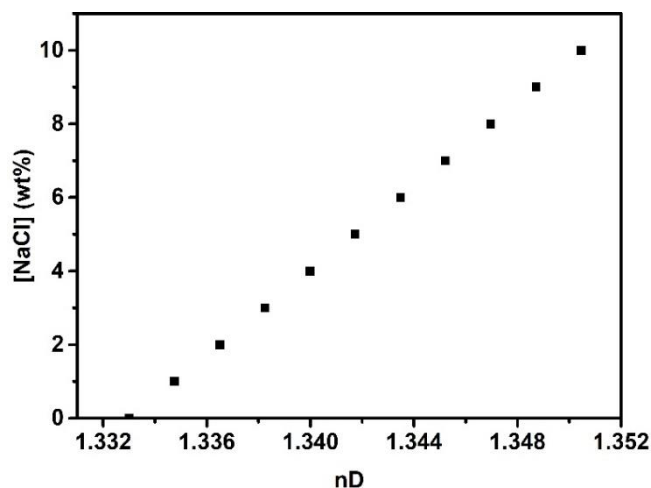


Figure D-1.1. [NaCl]-nD calibration points produced with Abbemat 550 refractometer

The calibration points [NaCl] vs. nD depicted in Figure D-1.1 was obtained by measuring the refractive index (nD) of beforehand prepared NaCl solutions of known concentrations. The linear regression of the [NaCl] vs. nD plot gave the following equation: $[\text{NaCl}] = 573.044 \times \text{nD} - 763.87$. The uncertainties on the slope and the intercept were determined using the DROITEREG function method ($\Delta a = 0.18704$; $\Delta b = 0.25096$). The uncertainties $\Delta[\text{NaCl}]$ and ΔWHC on the determined salinity and the water-to-hydrate conversion WHC, respectively, were obtained by differentiating the calibration equation ($[\text{NaCl}] = 573.044 \times \text{nD} - 763.87$) and equation 6.1. Finally, ΔE_{crys} was similarly obtained from equation 6.4 after determining ΔWHA , ΔCPHA from the differentiation of equations 6.2 and 6.3 (see Chapter 6).

D-2) Calibration control of Tian-Calvet BT2.15 apparatus

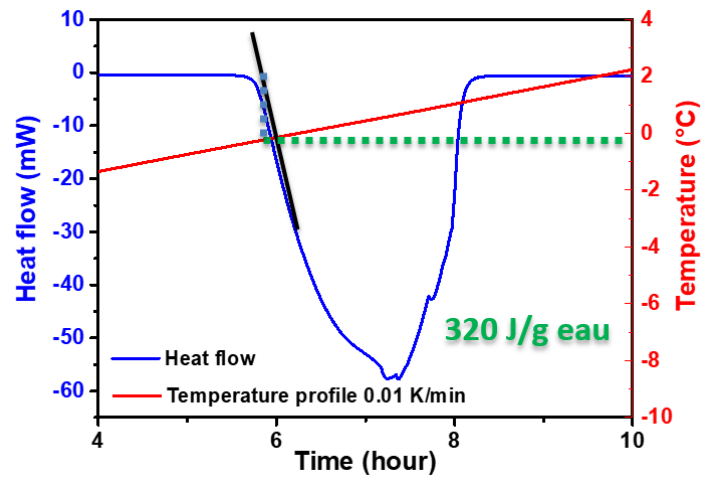


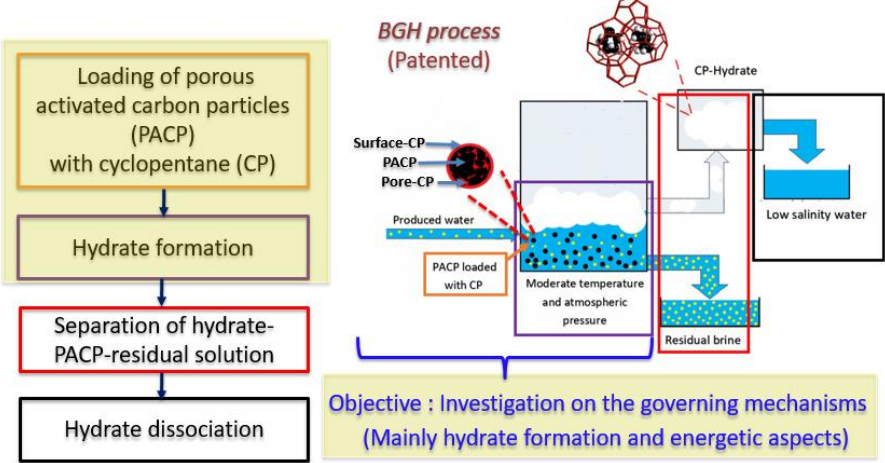
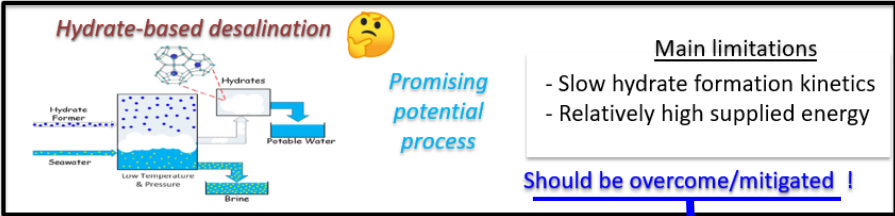
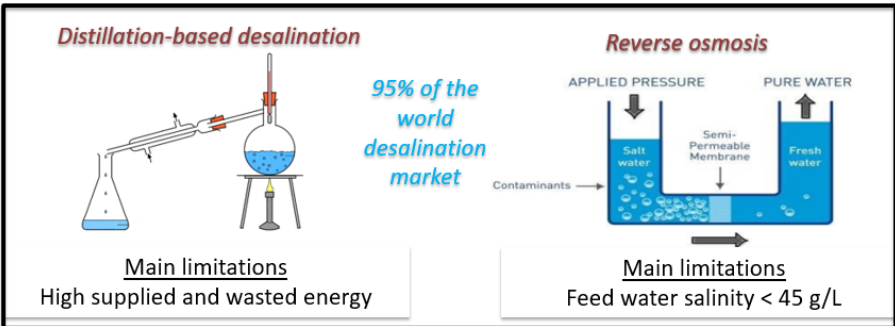
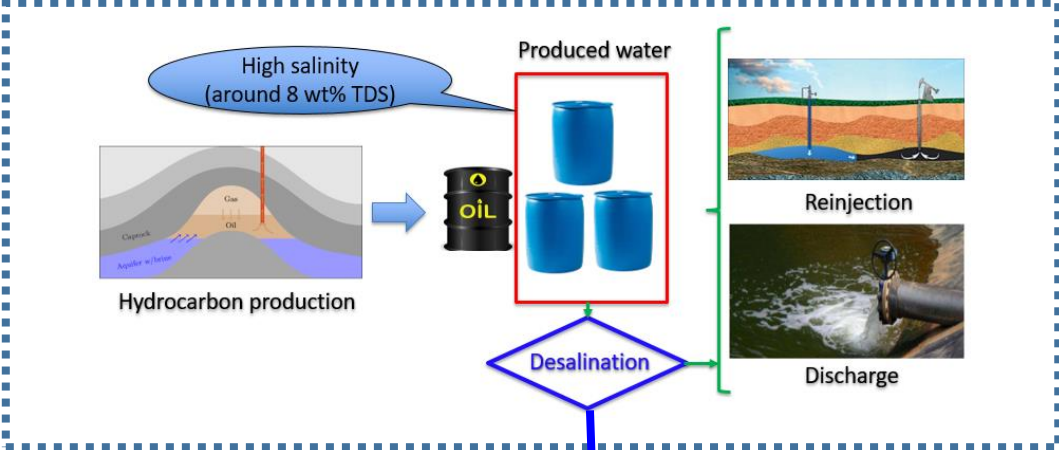
Figure D-2.1. Dissociation of ice used for determining uncertainties associated to the DSC measurements

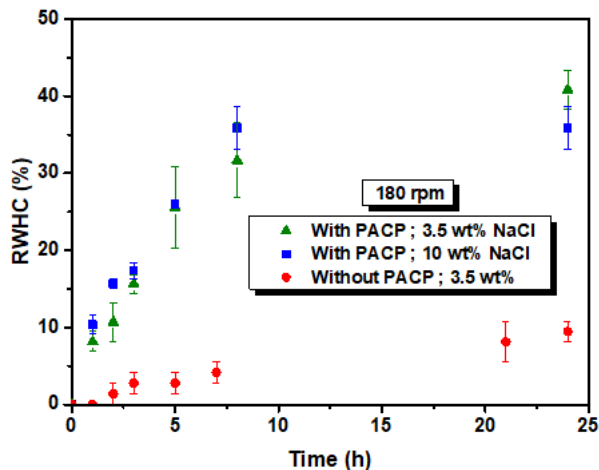
References

- [1] Mouahid A, Mise au point point d'un dispositif couple manométrique calorimétrique pour l'étude de l'adsorption de fluides supercritiques dans des milieux microporeux et mesoporeux. Physique[physics]. Université de Pau et des Pays de l'Adour., **2010**. Français. NNT : 10PAUU3020. tel-00573997.

Graphical abstract

CONTEXT AND OBJECTIVE

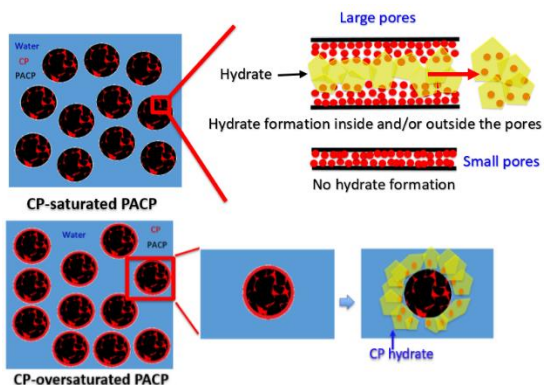




Chapter 4:

The CP contained in the low-size pores of the PACP cannot desorb.

CP trapping explains the low hydrate formed amount.



Chapter 6:

Hydrate crystallization from CP-saturated PACP induces partial thermal energy compensation.

The balanced energy ranges between 8 and 40% of the hydrate crystallization enthalpy

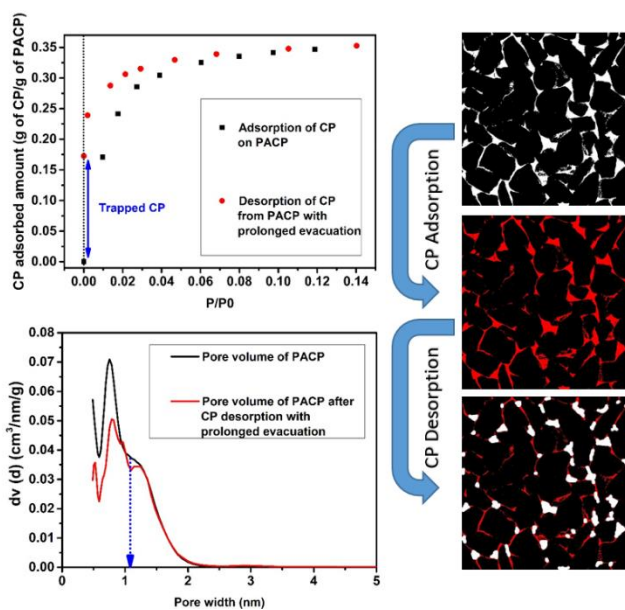
MAIN RESULTS

Chapter 3:

The CP-loaded PACP act as both:

- Source of CP
- Kinetic promoter of hydrate formation

Hydrate formed amount < 50% of the max possible.



Chapter 5:

CP contained in large pores can desorb to form hydrate within and/or outside the pores.

CP held by the external surface of PACP is released as droplets in water phase before being converted to hydrate.

